REPORT DOCUMENTATION PAGE

Form Approved
OMB No. 0704-0188

Public reporting burden for this collection of information is estimated to average 1 hour per response, including the time for reviewing instructions, searching existing data sources, gathering and maintaining the data needed, and completing and reviewing the collection of information. Send comments regarding this burden estimate or any other aspect of this collection of information, including suggestions for reducing this burden, to Washington Headquarters Services, Directorate for Information Operations and Reports, 1215 Jefferson Davis Highway, Suite 1204, Arlington, VA 22202-4302, and to the Office of Management and Budget, Paperwork Reduction Project (0704-0188), Washington, DC 20503.

1. AGENCY USE ONLY *(Leave blank)*

2. REPORT DATE
31 December 1995

3. REPORT TYPE AND DATES COVERED
Final 11/1/91 - 10/31/95

4. TITLE AND SUBTITLE
CONSTITUTIVE AND LOCALIZATION MODELS FOR ASSEMBLIES
OF CIRCULAR DISKS

5. FUNDING NUMBERS
F49620-92-J-0008-

6. AUTHOR(S)
Ronaldo I. Borja and Jon R. Wren

7. PERFORMING ORGANIZATION NAME(S) AND ADDRESS(ES)
STANFORD UNIVERSITY
125 Panama, Jordan Quad/Birch
Stanford, CA 94305-4020

8. PERFORMING ORGANIZATION REPORT NUMBER
SPO 8901

9. SPONSORING/MONITORING AGENCY NAME(S) AND ADDRESS(ES)
NA
AFOSR/NA
110 Duncan Ave., suite B115, Bolling AFB DC 20332-001
Capt. Sanders 2302 CS

10. SPONSORING/MONITORING AGENCY REPORT NUMBER
574 3600 294 4781 612302
CS 00000 61102F 503700
F03700

11. SUPPLEMENTARY NOTES

12a. DISTRIBUTION/AVAILABILITY STATEMENT
No limitations
Approved for public release, distribution unlimited

12b. DISTRIBUTION CODE

19960408 079

13. ABSTRACT *(Maximum 200 words)*

The complex response of a granular material to loading and unloading results directly from its particulate nature. The independent particle motions affect load transferal among neighboring grains and alters the microstructure of the material. Constituent particles typically transfer load through shear and normal forces at contacts with neighboring particles, causing the overall stress to be unevenly distributed in the material. This research focuses on the development of a mathematical model to derive the response of a macroscopic point in a granular material from the overall response of collection of particles. The formulation describes a methodology for deriving the macroscopic constitutive law from an implicit generation of the micromechanical response of the assembly using a quasi-static, and not a dynamic approach. The quasi-static approach is more appropriate for a broader class of engineering applications where inertia effects are negligible. The influence of pore fluid on the response of the assembly is also investigated in this research.

14. SUBJECT TERMS
constitutive model; fluid flow; micromechanics; particulate mechanics; quasi-static analysis; soil-structure interaction

15. NUMBER OF PAGES
214

16. PRICE CODE
N/A

17. SECURITY CLASSIFICATION OF REPORT

18. SECURITY CLASSIFICATION OF THIS PAGE

19. SECURITY CLASSIFICATION OF ABSTRACT

20. LIMITATION OF ABSTRACT
SAR

DTIC QUALITY INSPECTED 1

CONSTITUTIVE AND LOCALIZATION MODELS FOR ASSEMBLIES OF CIRCULAR DISKS

by

Ronaldo I. BORJA and Jon R. WREN
Department of Civil Engineering
Stanford University
Stanford, CA 94305-4020

Final Report
to
Department of the Air Force
Contract No. F49620-92-J-0008-P00003

December 31, 1995

Abstract

The complex response of a granular material to loading and unloading results directly from its particulate nature. The independent particle motions affect load transferal among neighboring grains and alters the microstructure of the material. Constituent particles typically transfer load through shear and normal forces at contacts with neighboring particles, causing the overall stress to be unevenly distributed in the material. This research focuses on the development of a mathematical model to derive the response of a macroscopic point in a granular material from the overall response of collection of particles.

The mathematical formulation describes a methodology for deriving the macroscopic constitutive law for a granular material directly from the discrete particle-to-particle interactions. The important feature of the model lies in the implicit generation of the micromechanical response of a particle assembly quasi-statically and not dynamically. The quasi-static approach to generating the micromechanical response is more appropriate for a broader class of engineering applications where inertia effects are negligible such as in creep deformation.

Table of Contents

Chapter 1. Introduction

1.1. Problem Statement 1
1.2. Structure of Presentation 6

Chapter 2. Micromechanical Relations

2.1. Introduction 8
2.2. Particle kinematics 9
2.3. Constitutive relation for particle contacts 13
2.4. Contact force integration 17

Chapter 3. Micromechanical-Macromechanical Connections

3.1. Introduction 21
3.2. Macroscopic stress field 22
3.3. Macroscopic deformation field 25
3.4. Macroscopic constitutive relation 27
3.5. Localization criterion 29

Chapter 4. Strain-driven Problem

4.1. Introduction 31
4.2. Algorithm for problems with an imposed deformation history 32
4.3. The notion of a repeating cell 35
4.4. Numerical simulations 38

Chapter 5. Stress-driven Problem

5.1. Introduction 60
5.2. Algorithm for problems with a imposed stress history 61
5.3. Particle displacement decomposition 63

5.4. Displacement decomposition and particle kinematics/contact forces .. 66
5.5. Displacement decomposition and the macroscopic stresses 69
5.6. Exact algorithmic tangent operator and concentration tensor 70
5.7. Discretized Newton method 73
5.8. Numerical simulations 75

Chapter 6. Elastic Contact Laws and Validation

6.1. Introduction 93
6.2. Cylindrical bodies in contact: normal interaction 94
6.3. Cylindrical bodies in contact: tangential interaction 97
6.4. Linearization of the contact laws 100
6.5. Numerical simulations 104

Chapter 7. Fluid Flow Model

7.1. Introduction 131
7.2. Balance Laws 132
7.3. Numerical Example 133

Chapter 8. Summary and Conclusions 138

Appendices

A. Virtual contact separation 140
B. Localization function 142
C. Strain-driven problem: tangent operator derivatives 143
D. Stress-driven problem: tangent operator derivatives 145

References 149

Computer Code for Micromechanical and Macromechanical Model

List of Tables

Chapter 2. Micromechanical Relations

Box 1 Contact force calculations. 20

Chapter 4. Strain-driven Problem

Box 2 Strain-driven algorithm. 34

Table 1 Model parameters. 39

Table 2 Convergence test for the 196-particle assembly: isotropic compression. 43

Table 3 Convergence test for the 196-particle assembly: simple shear. 44

Chapter 5. Stress-driven Problem

Box 3 Stress-driven algorithm. 64

Table 4 Model parameters. 76

Table 5 Convergence test for the 196-particle assembly: isotropic compression. 79

Table 6 Convergence test for the 196-particle assembly: shear. 81

Chapter 6. Elastic Contact Laws and Validation

Table 7 Model and material parameters. 106

Table 8 Convergence test for the 196-particle assembly: $E = 0.50$ GPa. 111

Table 9 Initial secant modulus. 112

List of Figures

Chapter 2. Micromechanical Relations

1 Slip between two contacting circular disks. 12

2 Constitutive models for indentation and slip at contact points. 14

Chapter 3. Micromechanical-Macromechanical Connections

3 Branch vector for two control volume particles. 23

Chapter 4. Strain-driven Problem

4 Particle degrees of freedom on the x_1, x_2 plane. 33

5 Periodic control volume subjected to a uniform deformation. 36

6 Enforcement of the periodicity condition. 37

7 Initial configuration for the 64-particle control volume. 46

8 Isolated clusters of particles form from an initially loose packing of circular disks. 47

9 Isotropic compression followed by lateral shearing for the 64-particle assembly. 48

10 Normalized overall shear stress versus overall shear strain showing the effects of the moduli ratio. 49

11 Periodicity test. 50

12 Initial configuration for the 58-particle control volume. 51

13 Deformed configuration for the 58-particle control volume showing zero-energy modes when the assembly is fully unconstrained. 52

14 Normalized overall normal stresses versus overall normal strains showing the effects of structural anisotropy. 53

15 Normalized overall shear stress versus overall shear strain. 54

16 Normalized overall shear stress versus overall shear strain. 55

17 Initial configuration for the 196-particle assembly. 56

18 Overall shear stress versus overall shear strain for the 196-particle assembly subjected to alternating isotropic compression and simple shear strain history. 57

19 Deformed configuration for the 196-particle assembly. 58

20 Overall shear stress versus overall shear strain. 59

Chapter 5. Stress-driven Problem

21 Initial configuration for the 64-particle closest packing control volume. 83

22 Normalized overall shear stress versus overall shear motion showing formation of a yield plateau. 84

23 Deformed configuration of the 64-particle closest packed control volume at the end of the shear loading. 85

24 Normalized overall shear stress versus overall shear motion showing the effects of the moduli ratio $\Omega = H'/k_T$. 86

25 Cyclic testing of the 58-particle control volume. 87

26 Localization function versus orientation of the plane of discontinuity. . 88

27 Normalized overall shear stress versus overall normal motion. 89

28 Overall shear stress versus overall shear motion for shear loading followed by isotropic loading. 90

29 Localization function minimum versus overall shear stress. 91

30 Deformed configuration for the 196-particle assembly. 92

Chapter 6. Elastic Contact Laws and Validation

31 Cylindrical bodies in contact under a normal load P. 95

32 Tangential displacements of two contacting cylinders. 98

33 Comparison between the Hertzian normal contact law and the linearized contact law for similar cylinders. 114

34 Initial configuration for the 49-particle control volume. 115

35 Deviator stress versus axial strain for the 49-particle control volume at different Young's moduli and Osterchelde sand. Confining stress = 29.43 N/cm^2. 116

36 Initial deviator stress versus axial strain for the 49-particle control volume at different Young's moduli and Osterchelde sand. Confining stress = 29.43 N/cm^2. 117

37 Deformed configuration for the 49-particle control volume. Confining stress = 29.43 N/cm^2. 118

38 Deviator stress versus axial strain for the 49-particle control volume at different Young's moduli and Karlsruhe sand. Confining stress = 19.62 N/cm^2. 119

39 Initial deviator stress versus axial strain for the 49-particle control volume at different Young's moduli and Karlsruhe sand. Confining stress = 19.62 N/cm^2. 120

40 Deformed configuration for the 49-particle control volume. Confining stress = 19.62 N/cm^2. 121

41 Initial configuration for the 196-particle control volume. 122

42 Sensitivity analysis: ramp function ε. 123

43 Sensitivity analysis: maximum normal contact force P_{max}. 124

44 Deviator stress versus axial strain for the 196-particle control volume at different Young's moduli and Osterchelde sand. Confining stress = 29.43 N/cm^2. 125

45 Initial deviator stress versus axial strain for the 196-particle control volume at different Young's moduli and Osterchelde sand. Confining stress = 29.43 N/cm^2. 126

46 Deformed configuration for the 196-particle control volume. Confining stress = 29.43 N/cm^2. 127

47 Deviator stress versus axial strain for the 196-particle control volume at different Young's moduli and Karlsruhe sand. Confining stress = 19.62 N/cm^2. 128

48 Initial deviator stress versus axial strain for the 196-particle control volume at different Young's moduli and Karlsruhe sand. Confining stress = 19.62 N/cm^2. 129

49 Deformed configuration for the 196-particle control volume. Confining stress = 19.62 N/cm^2. 130

Chapter 7. Fluid Flow Model

50 Two-dimensional plane-strain FE mesh. 136

51 Resulting average stress $\bar{\sigma}^*_{22}$ versus imposed average strain $\bar{\epsilon}_{22}$ demonstrating a lower stress plateau reached when two weak elements are incorporated at side of mesh. 137

52 Resulting average stress $\bar{\sigma}^*_{22}$ versus imposed average strain $\bar{\epsilon}_{22}$ demonstrating a "strengthening" effect due to negative pore pressures generated in a dilating material. 137

Chapter 1

Introduction

1.1. Problem Statement

Many problems of special interest to engineers and earth scientists involve characterization of the engineering behavior of granular materials such as soils. Granular materials respond quite differently from polycrystalline materials such as metals due to their particulate nature and more random microstructure. Since the particle-to-particle interaction is frictional in nature, contacts in granular media can easily form or break as the particles move toward their new equilibrium positions. From a modeling standpoint, the prediction of the new microstructure of the material represents a major source of numerical difficulty. Consequently, the effects of microstructure on the macromechanical response of granular media remain poorly understood.

The distinguishing features of a granular material's response to loading and unloading directly result from the material's particulate nature. Constituent particles typically interact with distinct neighboring granules at points of contact, and during loading/unloading, unbalanced shear and normal contact forces impel particles toward their new equilibrium positions. As a result, the overall stress field becomes unevenly distributed throughout the material. Many experimental, analytical and numerical models have been developed to study such particle behavior and its effects on the overall response of a granular material.

Several common experimental methods include microscopic evaluation of soil samples and the loading/unloading of metal, photoelastic disk assemblies. Oda [1–3] used a hardening resin to fix a sand sample's microstructure during deformation. They reported spatial distributions of the average number of contacts per particle, orientation of the long axes of the grains, and the orientation of the contact planes between particles. Drescher and De Josselin de Jong [4] and Oda et al. [5–6] photographed assemblies of photoelastic rods at various stages of loading to determine contact forces, displacements, and rotations of individual disks. However, such analyses are time consuming and lack flexibility to run multiple tests on precisely identical specimens for studying the effect of any parameters.

Analytical models provide expressions to predict the nonlinear behavior of uniformly packed and sized spheres. Deresiewiez [7] proposed a model for cubic arrays of uniform spheres that accommodated for the ultimate failure of the assembly and predicted a hysteretic stress-strain behavior. Thorton [8] developed a general solution for the strength of face-centered cubic array of uniform spheres and identified a variety of failure envelopes. This regular packing of uniform spheres and a few simple loading/unloading paths restrict the analytic approach to calculating stresses and displacements in a granular media.

In contrast to experimental and analytical models, numerical models allow the observation of minute changes in an idealized material's structure for any loading and unloading path. Numerical simulation provides access to detailed micromechanical statistics, particle motions, and interparticle forces. It also allows flexibility to alter loading paths, particle size distributions, and the physical properties of the particles.

Serrano and Rodriguez-Ortiz [9], Rodriguez-Ortiz [10], and Kishino [19] developed a numerical model for assemblies of circular disks by solving for an assembly of particle's deformation based on governing equations for each particle as it interacts with its surrounding particles. These models allow the specification of either a quasi-static stress or strain history for the assembly boundary. Serrano and Rodriguez-Ortiz calculate particle equilibrium forces and displacements by assuming that the incremental displacements of each particle center determines increments of contact force. They continually solve the linear system of equations relating the particle contact forces to the particle displacements and rotations. The contact theories of Mindlin [11] and Mindlin and Deresiewiez [12] form the basis of the matrix of contact compliances which must be updated for each iteration according to the loading path followed for each contact. Kishino's model, on the other hand, iteratively displaces and rotates each particle according to the contact stiffness matrix defined by the locations of neighboring particles. The contact stiffness matrix consists of simply rotating a constant diagonal matrix of normal and tangential contact compliances by a transformation matrix. The orientation of the vector connecting the centroids of contacting particles defines this matrix for each iteration. The model applies a strain history via the movement of four straight walls by prescribed incremental displacements and applies a stress history by moving the walls to attain the prescribed external stress according to the contact stiffnesses of the boundary.

Cundall and Strack [13] proposed a computationally less intensive algorithm for assemblies of particles called the distinct element method (DEM). The method considers the interaction of particles as a transient problem where states of equilibrium develop whenever internal forces balance. The crucial feature of the DEM lies in the choice of a small enough time step over which particle velocities and accelerations may be assumed constant and particle disturbances do not propagate further than a disk's contiguous neighbors. Many improvements on the original DEM algorithm have since been made [14–19]. The DEM, however, contains several shortcomings. The DEM simply employs a particle's acceleration to predict its direction of movement when in fact neighboring particles constrain this movement to be not co-axial with the particle's acceleration vector. Also, since the fundamental idea of the model rests on explicit integration of Newton's second law for each particle, the model treats all problems, even quasi-static ones, dynamically. Even with an extremely slow rate of loading, the DEM uses inertial effects to predict the future position of each particle. The particle displacements are calculated based on the "bounces" that particles make against contacting particles, and not on the rotational and "scraping" effects which dominate a granular material's response to shearing deformations. For a problem with a very slow loading rate or even a static problem, it becomes important to regulate the time effect in order for the inertial effects to be negligible. Furthermore, the explicit nature of the numerical integration algorithm makes the DEM conditionally stable and restricts the step size by the natural period of the smallest particle. Thus, for even the simplest quasi-static stress histories, inertial effects and numerical stability require many computational cycles (see, e.g., [20–22]).

In a different approach to numerical modeling of granular materials, micromechanical models describe the deformation behavior of an assembly of particles using the continuum concepts of stress and strain. This type of model derives the constitutive relationship for a granular assembly based on the microstructure and interaction between particles. Nemat-Nassar and Mehrabadi [23] describe the overall mechanical response of the granular mass with a simple micromechanical model that treats the translation and rotation of discrete particles as continuous fields. They transform a discrete system into an equivalent continuum where continuum concepts of stress and strain describe the material's overall behavior. The model decomposes the local (micro) deformation rate and spin into a 'plastic' or 'inelastic' part which leaves the soil fabric unchanged, and an accommodating part which changes the soil fabric and results in a change in the overall stress. At the macroscopic level, the notion of self-consistency as described by Hill [24,25] relates the overall nominal stress rate to the overall velocity gradient in terms of local variables.

Similarly, Chang et al. [26–28] adopt a self-consistent method to account for the effect of particle separation, particle sliding associated with large deformations, and a nonuniform strain field. Their model proposes a decomposition of the general nonlinear particle displacement field into a linear displacement field and a field describing the particle's movement to achieve equilibrium after the imposition of the linear field. In addition, the magnitude of the local (micro) strain depends largely on the local stiffness rather than on the location of a particle and its contacting neighbors. In effect, the macro-behavior of the granular assembly can be traced back to the micromechanical behavior of a contact. This model, however, only subjects the boundaries of the representative unit consisting of many randomly arranged particles to displacements compatible with a uniform strain and does not apply a stress field.

The modeling approach pursued in this study differs somewhat from those proposed in previous studies in that the nonuniform and locally discontinuous particle motions directly derive the macroscopic constitutive equations. In effect, the model treats the assembly of particles as a separate structure whose overall response reflects the character of a macroscopic point experiencing uniform deformation. Note that the macro-element is interpreted herein as a homogeneously deforming element and not as a soil sample experiencing non-uniform deformation. Viewing the macro-element in this fashion renders the resulting model perfectly amenable to finite element implementation since the overall response of the particle assembly may now be interpreted as the sampled macroscopic response at the Gauss integration points. It also allows the representation of the nonlinear elasto-plastic behavior of granular materials using laws derived from particle-to-particle contacts.

The central features of the model can be described as follows. The model's foundation rests on the conventional hypothesis in computational plasticity by assuming a deformation-driven problem, i.e., a given overall displacement gradient determines the overall stress response. The assembly of particles representing the macroscopic point experiences a prescribed overall uniform motion, after which the particles are allowed to move in the microscopic sense. During the particle motion, contacts are allowed to form or break, thus altering the microstructure of the material. The overall stresses are then evaluated from the contact forces that develop between the particles using the relationships derived from a virtual work formulation presented in [23,24,29].

When the particle assembly experiences a macroscopic stress history, the model iteratively seeks the assembly's overall uniform motion which creates contact forces exactly balancing the applied stress. The basis of the model lies on the analytical description of the change in each particle's displacement (a microscopic quantity) with respect to the overall motion of the particle assembly (a macroscopic quantity). In the terminology of self-consistent models, this matrix describes the so-called 'concentration tensor.' To formalize this complex microscopic-macroscopic relationship, a decomposition similar to Chang [26–28] is employed for the constituent particle motions. Each particle's movement consists of a uniform displacement resulting from the overall strain field and a nonuniform, locally discontinuous motion necessary to balance the contact forces among neighboring particles and the applied loads. The exact description of the concentration tensor, however, does not lend itself to elegant or efficient computer implementation. To circumvent this difficulty, this tensor is defined with a secant approximation that retains the essential properties of the exact description. The formulation allows finite motions of the individual particles, but the macroscopic material response is formulated based on infinitesimal theory. The model describes only the material overall response and leaves the finite rotation and/or large deformation of the assembly of particles for a future application.

Throughout the application of an overall stress history, the onset of localization in the particle assembly is investigated. The model's macroscopic constitutive relation falls neatly within previous localization analyses of Rice [30] and Rudnicki and Rice [31]. Localization is interpreted as an instability in the macroscopic constitutive description of the material's deformation. Thus, it is possible for a material to undergo localized deformation even before the constitutive relation ceases to become invertible, or even before some related indication of ideally plastic response is met. The macroscopic model's framework allows the natural incorporation of this localization analysis.

The next section describes the format of the presentation of the micromechanical-macromechanical model.

1.2. Structure of Presentation

Chapter 2 presents the kinematics of particle motion from a finite-displacement viewpoint that includes particle rotation. This chapter also details the contact model constitutive relation for describing the particle-to-particle interaction. These equations will then be specialized to a two-dimensional assembly consisting of rigid circular disks.

Chapter 3 describes the field equations essential for deriving the micromechanical-macromechanical connections between the overall response of the granular material and the constituent particle behavior. This chapter also presents the macroscopic constitutive relation used for modeling the overall response of the material and for predicting the onset of localization in the control volume.

Chapter 4 and Chapter 5 present the numerical algorithms for determining the displacement vector of each particle when the imposed boundary conditions are strain-controlled and stress-controlled, respectively. The notion of a repeating cell essential to the numerical implementation of the model will also be described as part of Chapter 4. Chapter 5 pays special attention to the stress driven problem and the exact steps necessary to solve this problem.

Chapter 4 and Chapter 5 end with two-dimensional plane-strain numerical simulations on regular and random initial packing of circular disks. The examples demonstrate the model's ability to capture the periodicity of the control volume, its invariance under rigid body motion, and its convergence characteristics for both boundary conditions. Experiments which include a localization analysis will also be presented.

Chapter 6 focuses on model validation. This chapter includes a secant approximation to the Hertzian contact theory to describe the contact law between two particles. The performance of the numerical model is then compared with experimental plane strain tests on dry sands.

Chapter 7 extends the dry model to the case of saturated granular assemblies. A continuum methodology is pursued to predict the pore pressure changes in fully saturated granular assemblies as a result of changes in the soil's microstructure.

Chapter 8 summarizes the work done. It also contains recommendations for further study and for extension of the model developed in this thesis.

Chapter 2

Micromechanical Relations

2.1. Introduction

The fundamental elements of the model framework rest on the interpretation that the overall response of an assembly of particles represents the behavior of a uniformly deforming macroscopic point in a granular material. During loading and unloading of the assembly, constituent particles experience locally discontinuous motions as unbalanced particle contact forces drive them towards new equilibrium positions. Within the assembly, each discrete particle can be visualized as a 'node' connected to contiguous nodes via 'elements' having normal and tangential degrees of freedom. When a contact forms between two particles, an element is created and its loading history tracked until the particles separate causing the element to disappear. Thus, throughout the loading history, the number of nodes in the assembly control volume remains constant but the number and orientation of elements may fluctuate.

Attention in this chapter focuses on only the interaction of two contacting particles (nodes) within the assembly control volume and their contact element. First, the kinematics of the particles motion are considered assuming a finite displacement of the two particles. Next, the constitutive equation describing the contact element's elasto-plastic behavior will be presented in the context of plasticity theory. Finally, the constitutive relation will be integrated assuming a finite incremental motion.

2.2. Particle kinematics

Consider a finite-sized, spherical particle A. Within particle A, let $d\boldsymbol{X}^A$ represent a material vector in the undeformed configuration, and $d\boldsymbol{x}^A$ denote the position occupied by $d\boldsymbol{X}^A$ in the deformed configuration. Assume $d\boldsymbol{X}^A$ and $d\boldsymbol{x}^A$ are measured with respect to the particle centroids $\hat{\boldsymbol{X}}^A$ and $\hat{\boldsymbol{x}}^A$ respectively. Thus, the position vectors in the undeformed and deformed configurations of any point in particle A are given by

$$\boldsymbol{X}^A = \hat{\boldsymbol{X}}^A + d\boldsymbol{X}^A\,, \tag{2.1}$$

$$\boldsymbol{x}^A = \hat{\boldsymbol{x}}^A + d\boldsymbol{x}^A\,. \tag{2.2}$$

With reference to the undeformed configuration, the deformation gradient $\boldsymbol{F}$ relates the material vector $d\boldsymbol{X}^A$ to the vector $d\boldsymbol{x}^A$ via

$$d\boldsymbol{x}^A = \boldsymbol{F}^A \cdot d\boldsymbol{X}^A\,, \tag{2.3}$$

where

$$\boldsymbol{F}^A = \boldsymbol{R}^A \cdot \boldsymbol{U} = \boldsymbol{V} \cdot \boldsymbol{R}^A\,, \tag{2.4}$$

and $\boldsymbol{U}$ and $\boldsymbol{V}$ are the right and left stretch tensors, respectively, and $\boldsymbol{R}^A$ is the orthogonal rotation tensor. For a rigid particle, $\boldsymbol{U} = \boldsymbol{V} = \boldsymbol{I}$, the identity tensor. The material vector $d\boldsymbol{X}^A$ only experience a rigid body rotation and displacement but no stretch as seen by reducing (2.3) to

$$d\boldsymbol{x}^A = \boldsymbol{R}^A \cdot d\boldsymbol{X}^A\,. \tag{2.5}$$

Thus, particle A only undergoes rigid body rotation and translation.

To quantify this result, let the centroidal particle displacement $\boldsymbol{d}^A$ be defined by $\boldsymbol{d}^A = \boldsymbol{x}^A - \boldsymbol{X}^A$. In the deformed configuration, the position vector of any point in particle A then becomes

$$\boldsymbol{x}^A = \hat{\boldsymbol{X}}^A + \boldsymbol{d}^A + \boldsymbol{R}^A \cdot d\boldsymbol{X}^A\,. \tag{2.6}$$

The position vector $\boldsymbol{x}^A$ can be found by successive application of the translation $\boldsymbol{d}^A$ and a rigid body rotation $\boldsymbol{R}^A$ of the material vector $d\boldsymbol{X}^A$.

Now, consider a contact point between two spherical particles A and B. With respect to the undeformed configuration, the contact point at C has a position vector given by

$$\boldsymbol{X}^C = \hat{\boldsymbol{X}}^A + r^A \boldsymbol{N}^A = \hat{\boldsymbol{X}}^B + r^B \boldsymbol{N}^B \,, \tag{2.7}$$

where r^A and r^B denote the particle radii, and $\boldsymbol{N}^A$ and $\boldsymbol{N}^B$ represent the unit outward vectors through C. Since $\boldsymbol{N}^A = -\boldsymbol{N}^B$, these vectors can be written as

$$\boldsymbol{N}^A = -\boldsymbol{N}^B = (\hat{\boldsymbol{X}}^B - \hat{\boldsymbol{X}}^A)/(r^A + r^B) \,. \tag{2.8}$$

With respect to the deformed configuration, the contact point at C has a position vector given by (2.6) as

$$\boldsymbol{x}^C = \hat{\boldsymbol{x}}^A + r^A \boldsymbol{R}^A \cdot \boldsymbol{N}^A \,. \tag{2.9}$$

Likewise, a new contact point c in the deformed configuration has a position vector given by

$$\boldsymbol{x}^c = \hat{\boldsymbol{x}}^A + r^A \boldsymbol{n}^A = \hat{\boldsymbol{x}}^B + r^B \boldsymbol{n}^B \,, \tag{2.10}$$

where the unit outward vectors $\boldsymbol{n}^A$ and $\boldsymbol{n}^A$ are found to be

$$\boldsymbol{n}^A = -\boldsymbol{n}^B = (\hat{\boldsymbol{x}}^B - \hat{\boldsymbol{x}}^A)/(r^A + r^B) \,. \tag{2.11}$$

In general, the new contact point c does not coincide with the old contact point C.

Taking the magnitudes of equations (2.7) and (2.11) yields

$$r^A + r^B = \|\hat{\boldsymbol{X}}^B - \hat{\boldsymbol{X}}^A\| = \|\hat{\boldsymbol{x}}^B - \hat{\boldsymbol{x}}^A\| \,. \tag{2.12}$$

If (2.12) is not satisfied, the particles will either separate or overlap. The initial and final indentation becomes, respectively,

$$\Delta = r^A + r^B - \|\hat{\boldsymbol{X}}^B - \hat{\boldsymbol{X}}^A\| \tag{2.13}$$

$$\delta = r^A + r^B - \|\hat{\boldsymbol{x}}^B - \hat{\boldsymbol{x}}^A\| \tag{2.14}$$

where $\Delta, \delta > 0$.

Now, consider the relative rotation of the contact point on particle A from C

to c. This rotation is given by the vector

$$\boldsymbol{\theta}^{AC} = \theta^{AC}\,\tilde{\boldsymbol{\theta}}^{AC}, \tag{2.15}$$

where

$$\tilde{\boldsymbol{\theta}}^{AC} = (\boldsymbol{R}^A \cdot \boldsymbol{N}^A) \times \boldsymbol{n}^A / \sin|\theta^{AC}|, \tag{2.16}$$

and θ^{AC} represents the magnitude of the relative rotation, and $\tilde{\boldsymbol{\theta}}^{AC}$ denotes the unit normal to the plane on which the rotation occurs. Similar results are obtained if the contact point is interpreted as belonging to particle B.

If particle B is fixed against rotation and displacement, the magnitude of the contact slip is given by

$$\gamma = \theta^{AC} r^A \tag{2.17}$$

which represents the length of an arc on the surface of a sphere of radius r^A, subtended by the angle θ^{AC}, and lying on a plane with unit normal $\tilde{\boldsymbol{\theta}}^{AC}$. If particle B also rotates, the slip becomes

$$\boldsymbol{\gamma} = \boldsymbol{\theta}^{AC} r^A + \boldsymbol{\theta}^{BC} r^B; \quad \gamma = \|\boldsymbol{\gamma}\|. \tag{2.18}$$

If $\boldsymbol{\theta}^{AC} r^A = -\boldsymbol{\theta}^{BC} r^B$, then $\gamma = 0$ and particles A and B simply undergo pure rolling.

The rotation vector relationships collapse neatly for 2D-plane strain analysis. Consider the same particles A and B, now represented by circular disks with radii r^A and r^B on the x_1, x_2-plane, respectively. In this case, the rotation of particle A defined in (2.5) becomes

$$\boldsymbol{R}^A = \begin{bmatrix} \cos\theta^A & -\sin\theta^A \\ \sin\theta^A & \cos\theta^A \end{bmatrix}, \tag{2.19}$$

where θ^A denotes the rigid body rotation of particle A.

The relative motion of the contact points is now given by the scalar angular rotations θ^{AC} and θ^{BC} which from (2.15) and (2.16) can be written as

$$\sin\theta^{AC} = \boldsymbol{e}_3 \cdot (\boldsymbol{R}^A \cdot \boldsymbol{N}^A) \times \boldsymbol{n}^A, \tag{2.20}$$

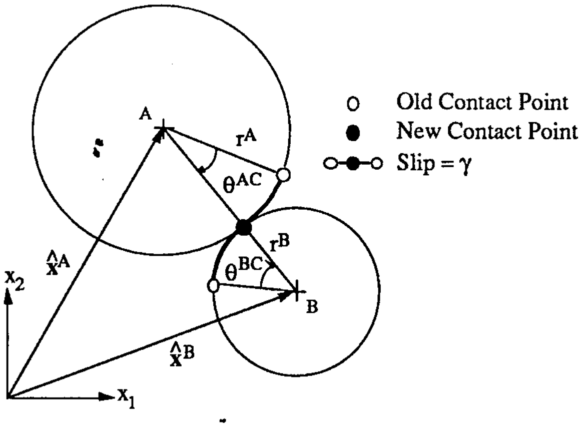

Figure 1. Slip between two contacting circular disks.

where $\boldsymbol{e}_3$ is the unit basis vector in the x_3 direction. Expanding the right-hand side of (2.20) gives

$$\begin{aligned} \sin\theta^{AC} &= \cos\theta^A \; \boldsymbol{e}_3 \cdot \boldsymbol{N}^A \times \boldsymbol{n}^A - \sin\theta^A \; \boldsymbol{N}^A \cdot \boldsymbol{n}^A \\ &= \cos\theta^A \; \sin\theta^C - \sin\theta^A \; \cos\theta^C \\ &= \sin(\theta^C - \theta^A)\,, \end{aligned} \tag{2.21}$$

where θ^C denotes the rotation of the unit normal vector (assumed positive counterclockwise). A similar result can be obtained for particle B.

Thus, equation (2.21) implies that the relative rotation of the contact points equals the change in direction of the unit normal minus the total rotation of the particle

$$\theta^{AC} = \theta^C - \theta^A\,, \tag{2.22}$$

$$\theta^{BC} = \theta^C - \theta^B\,. \tag{2.23}$$

The particle slip can be defined analogously to (2.18) as

$$\gamma = \theta^{AC} r^A + \theta^{BC} r^B \tag{2.24}$$

assuming that Δ, $\delta > 0$. Physically, the slip γ represents the tangential stretching of the contact spring which, for large rotations, wraps around the particle sides as shown in Figure 1.

2.3. Constitutive relation for particle contacts

In the following, Mohr-Coulomb frictional resistance to slip governs the microstructural rearrangement mechanism between two particles. Slip between two particles cannot occur until the contact shear force reaches a critical value. This particle contact model is analogous to crystallographic slip where slip only occurs on well defined slip systems when a critical resolved shear stress is achieved. The slip plane and slip direction uniquely define the slip system.

In crystal slip, an a priori known set of slip systems constrain the direction and location of slip. The central task lies in choosing a set of independent active slip systems from a pool of known linearly dependent potentially active slip systems. However, particulate slip occurs in a direction randomly constrained by neighboring particles but on a known contact plane with a normal vector parallel to the branch vector connecting contiguous particle centroids. Therefore, in contrast to crystallographic slip, as many potential slip systems exist as there are admissible slip directions — an infinite set. Since these systems all lie in the same plane with only different slip directions, the problem of dependent slip systems does not exist. For more information on the exact selection of the active crystal slip systems one may see Borja and Wren [32].

In the following, only two dimensional circular disk particles are considered. The formalism of plasticity theory has been adopted for describing the constitutive model for an ideally plastic and work-hardening particle contact. At the contact points, the particles will exert a normal force f_N and a tangential force f_T through their contact element. Each contact element is represented as a pair of springs with stiffnesses k_N and k_T. The associated deformations are given by a normal indentation δ of the normal spring and a slip γ in the tangential direction. Figure 2 shows the sign conventions for the forces and the deformations. In condensed form, the contact element forces, deformations, and stiffness are

$$\mathcal{F} = \begin{Bmatrix} f_N \\ f_T \end{Bmatrix} ; \quad \mathcal{D} = \begin{Bmatrix} -\delta \\ \gamma \end{Bmatrix} ; \quad \mathcal{K}^e = \begin{bmatrix} k_N & 0 \\ 0 & k_T \end{bmatrix} . \tag{2.25}$$

If the spring stiffnesses are constant and $k_N \gg 0$, then the indentation becomes very small, and the particles may be considered rigid. A more elaborate constitutive

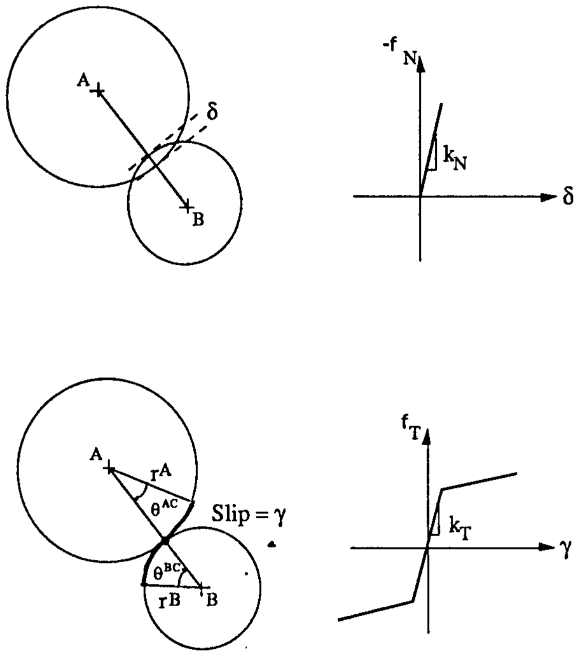

Figure 2. Constitutive models for indentation and slip at contact points.

model for the contact forces is provided by a class of nonlinear elastic contact theories where the spring stiffnesses are not constant (see e.g., [11, 12]), but this could engender additional numerical complexity.

On a particle level the rate-constitutive equation for the contact element is given by

$$\dot{\mathcal{F}} = H(\delta)\mathcal{K}^e \cdot \dot{\mathcal{D}}^e = H(\delta)\mathcal{K}^e \cdot (\dot{\mathcal{D}} - \dot{\mathcal{D}}^p) , \tag{2.26}$$

where $\dot{\mathcal{D}}^e$ and $\dot{\mathcal{D}}^p$ are the elastic and plastic components of $\dot{\mathcal{D}}$, respectively, and $H(\delta)$ is the Heaviside function which takes on the value of unity when $\delta > 0$ and zero otherwise. Note that setting large spring stiffnesses results in a rigid-plastic contact model.

Plastic tangential slip takes place when the tangential contact force reaches a critical maximum value of the Mohr-Coulomb frictional resistance given by the expression

$$F = |f_T| - \alpha + f_N \tan\phi = 0\,, \tag{2.27}$$

where ϕ is the particle-to-particle angle of internal friction, and α is the cohesive force (for a purely frictional contact $\alpha = 0$). In the terminology of crystallographic slip, the particle contact becomes potentially active when $F = 0$. Equation (2.27) represents the yield condition corresponding a straight line separating the elastic and plastic responses. The elastic region is given by the set

$$E = \left\{ f_T \in \Re^1 \mid F := |f_T| - \alpha + f_N \tan\phi < 0 \right\} . \tag{2.28}$$

Following plasticity theory, the flow rule defines the direction of the plastic slip vector $\dot{\mathcal{D}}^p$ by assuming a plastic potential function of the form

$$G = |f_T| - \alpha + f_N \tan\psi\,, \tag{2.29}$$

where the friction angle in (2.28) has been replaced by the dilation angle ψ. Hence, the flow rule G in which $\psi = 0$ gives

$$\dot{\mathcal{D}}^p = \left\{ \begin{matrix} 0 \\ \dot{\gamma}^p \end{matrix} \right\} = \lambda \frac{\partial G}{\partial \mathcal{F}} = \lambda \left\{ \begin{matrix} 0 \\ 1 \end{matrix} \right\} . \tag{2.30}$$

Note that the consistency parameter λ has the physical meaning of being the particle contact slip itself.

The constitutive equation (2.26) can now be expanded to give

$$\dot{\mathcal{F}} = H(\delta) \left\{ \begin{matrix} -k_N \dot{\delta} \\ k_T(\dot{\gamma} - \dot{\gamma}^p) \end{matrix} \right\} . \tag{2.31}$$

In terms of the centroidal particle displacements and rotations, the indentation rate $\dot{\delta}$ for small δ can be found from (2.14) as

$$\dot{\delta} = \boldsymbol{n}^A \cdot (\dot{\boldsymbol{d}}^A - \dot{\boldsymbol{d}}^B) = \boldsymbol{n}^B \cdot (\dot{\boldsymbol{d}}^B - \dot{\boldsymbol{d}}^A)\,. \tag{2.32}$$

Similarly, the slip rate $\dot{\gamma}$ for small δ is found from (2.22)–(2.24) to be

$$\dot{\gamma} = \dot{\theta}^{AC} r^A + \dot{\theta}^{BC} r^B\,, \tag{2.33}$$

$$\dot{\theta}^{AC} = \dot{\theta}^C - \dot{\theta}^A\,, \tag{2.34}$$

$$\dot{\theta}^{BC} = \dot{\theta}^C - \dot{\theta}^B\,, \tag{2.35}$$

in which

$$\dot{\theta}^C = \left(\boldsymbol{e}_3 \cdot \boldsymbol{N}^A \times \frac{\dot{\boldsymbol{d}}^B - \dot{\boldsymbol{d}}^A}{r_A + r_B} \right) \sec \theta^C = \left(\boldsymbol{e}_3 \cdot \boldsymbol{N}^B \times \frac{\dot{\boldsymbol{d}}^A - \dot{\boldsymbol{d}}^B}{r_A + r_B} \right) \sec \theta^C \,. \tag{2.36}$$

The hardening law represents an important element of any constitutive relation. For simplicity, a linear hardening law has been assumed of the form

$$\dot{\alpha} = H' |\dot{\gamma}^p| \,. \tag{2.37}$$

Note that when $H' = 0$, the particle contact becomes ideally plastic. Thus, the consistency condition which requires that the yield condition be satisfied as long as the contact is in the plastic state gives

$$\lambda \equiv \dot{\gamma}^p = \left(1 + \frac{H'}{k_T} \right)^{-1} \left(\dot{\gamma} + \frac{k_N}{k_T} \tan \phi \, \dot{\delta} \right) . \tag{2.38}$$

The loading/unloading conditions for a particle contact slip system can now be written as follows:

i. the contact unloads or is *inactive* ('stick' mode) if

$$F < 0, \text{ or } F = 0 \text{ and } \lambda < 0; \tag{2.39}$$

ii. the contact loads or is *active* ('slip' mode) if

$$F = 0 \text{ and } \lambda > 0. \tag{2.40}$$

The constitutive relations (2.26) can be summarized by relating the particle forces $\mathcal{F}$ to the contact movement $\dot{\mathcal{D}}$ as follows:

$$\dot{\mathcal{F}} = H(\delta) \mathcal{K}^{ep} \dot{\mathcal{D}} \,, \tag{2.41}$$

where

$$\mathcal{K}^{ep} = \mathcal{K}^e \cdot (\mathbf{1} - \mathcal{K}) \,, \tag{2.42}$$

and

$$\mathcal{K} = \begin{bmatrix} 0 & 0 \\ \frac{k_N}{k_t + H'} \tan \phi & \frac{H'}{k_T (k_T + H')} \end{bmatrix} , \tag{2.43}$$

and **1** is the second-rank identity tensor and $\mathcal{K}^{ep}$ are the elastic-plastic moduli. The constitutive relation (2.41) for a general particle contact has two branches which corresponds to continued loading ('slip') and to unloading ('stick') (see Figure 2). Clearly, if the slip system is inactive or unloads ('stick'), the response is purely elastic and (2.42) reduces to $\mathcal{K}^{ep} = \mathcal{K}^{e}$.

2.4. Contact force integration

Let the superimposed ∇ denote the time rate of change co-rotational with the contact normal. Consider a rate constitutive equation of the form

$$\overset{\nabla}{\mathcal{F}} = \boldsymbol{R} \cdot \dot{\mathcal{F}} + \dot{\boldsymbol{R}} \cdot \mathcal{F} \,, \tag{2.44}$$

where $\boldsymbol{R}$ represents a transformation operator which rotates the local contact element axes to the global (Cartesian) coordinate system. The first term on the right-hand side of (2.44) is given by (2.41) and represents the material response due to deformation of the contact element. The second term accounts for rotational effects. For two-dimensional problems on the plane x_1, x_2, the rotation and rotational rate take the form

$$\boldsymbol{R} = \begin{bmatrix} \cos\theta & -\sin\theta \\ \sin\theta & \cos\theta \end{bmatrix} , \tag{2.45}$$

$$\dot{\boldsymbol{R}} = -\begin{bmatrix} \sin\theta & \cos\theta \\ -\cos\theta & \sin\theta \end{bmatrix} \dot{\theta} \,, \tag{2.46}$$

where θ is the orientation of the contact normal with respect to the positive Cartesian x_1-axis. Since $\boldsymbol{N}$ is fixed and θ^C represents the rotation of $\boldsymbol{n}$ relative to $\boldsymbol{N}$, $\dot{\theta} = \dot{\theta}^C$, see (2.36).

The form of (2.44) facilitates an exact analytical integral of forces which leads to an incremental constitutive equation of the form

$$\Delta \boldsymbol{f} = \int_{t_n}^{t_{n+1}} \overset{\nabla}{\mathcal{F}} \, \mathrm{d}t = \boldsymbol{R}_{n+1}\mathcal{F}_{n+1} - \boldsymbol{R}_n \mathcal{F}_n = \boldsymbol{f}_{n+1} - \boldsymbol{f}_n \,, \tag{2.47}$$

where $\boldsymbol{f}_{n+1} = \boldsymbol{R}_{n+1}\mathcal{F}_{n+1}$, $\boldsymbol{f}_n = \boldsymbol{R}_n\mathcal{F}_n$, and $\mathcal{F}_{n+1} = \{f_N, f_T\}^t$. The forces $\boldsymbol{f}_n$ and $\boldsymbol{f}_{n+1}$ will be used in Chapter 4 to construct internal force vectors for each contact element.

Expressions for the contact forces $\mathcal{F}_{n+1}$ will be obtained by considering contacting particles A and B. Assume that at time t_n the positions of the particle centroids, $\boldsymbol{x}^A$ and $\boldsymbol{x}^B$, are well defined. Then integrating (2.41) yields the component f_N:

$$(f_N)_{n+1} = -H_\varepsilon(\delta_{n+1}) k_N \delta_{n+1}\,; \quad \delta_{n+1} = r^A + r^B - \|\boldsymbol{l}_{n+1}\|\,, \tag{2.48}$$

where

$$\boldsymbol{l}_{n+1} = \hat{\boldsymbol{X}}^B + \boldsymbol{d}^B_{n+1} - (\hat{\boldsymbol{X}}^A + \boldsymbol{d}^A_{n+1})\,, \tag{2.49}$$

and H_ε is a ramp function of the form

$$H_\varepsilon(\delta_{n+1}) = \begin{cases} 1, & \text{if } \delta_{n+1} > \varepsilon; \\ \delta_{n+1}/\varepsilon, & \text{if } 0 < \delta_{n+1} \leq \varepsilon; \\ 0, & \text{if } \delta_{n+1} \leq 0. \end{cases} \tag{2.50}$$

in which ε is a 'sufficiently small' number. This ramp function approximates the Heaviside function such that as $\varepsilon \to 0$, $H_\varepsilon(\delta) \to H(\delta)$. It makes the integrated constitutive equation continuous in the sense of Lipschitz [33] and regularizes an otherwise non-regular contact problem. The ramp function renders the discrete contact forces amenable to linearization.

The tangential force f_T reflects the previous slip mode between two contacting particles and contains the material memory. Thus, assuming that at time t_n the magnitude, and the sense of the force $(f_T)_n$ are known, the slip increment can then be simply evaluated as

$$\Delta\gamma = \Delta\theta^{AC} r^A + \Delta\theta^{BC} r^B\,, \tag{2.51}$$

where

$$\Delta\theta^{AC} = \Delta\theta^C - (\theta^A_{n+1} - \theta^A_n)\,, \tag{2.52}$$

$$\Delta\theta^{BC} = \Delta\theta^C - (\theta^B_{n+1} - \theta^B_n)\,, \tag{2.53}$$

and

$$\Delta\theta^C = \sin^{-1}(\boldsymbol{e}_3 \cdot \boldsymbol{n}^A_n \times \boldsymbol{n}^A_{n+1}) = \sin^{-1}(\boldsymbol{e}_3 \cdot \boldsymbol{n}^B_n \times \boldsymbol{n}^B_{n+1})\,. \tag{2.54}$$

Now, the contact modes (2.39) and (2.40) can be defined for a finite incremental motion assuming the particles remain in contact during the time step as follows:

i. the contact is in 'stick' mode if

$$|\,(f_T)_n + H_\varepsilon k_T \Delta\gamma\,| \;<\; \alpha_n + k_N \delta_{n+1} \tan\phi\,, \tag{2.55}$$

and

$$f_T = (f_T)_n + H_\varepsilon k_T \Delta\gamma\,, \tag{2.56}$$

$$\Delta\gamma^p = 0\,, \tag{2.57}$$

otherwise;

ii. the contact is in 'slip' mode:

$$f_T = \mathrm{sign}(f_T^{\mathrm{tr}})\alpha_{n+1} - (f_N)_{n+1} \tan\phi\,, \tag{2.58}$$

where

$$f_T^{\mathrm{tr}} = (f_T)_n + H_\varepsilon k_T \Delta\gamma\,, \tag{2.59}$$

$$\alpha_{n+1} = \alpha_n + H'|\Delta\gamma^p|\,, \tag{2.60}$$

$$|\Delta\gamma^p| = \frac{|f_T^{\mathrm{tr}}| - \alpha_n + f_N \tan\phi}{H_\varepsilon k_T + H'}\,, \tag{2.61}$$

and f_T^{tr} represents the trial tangential force, α_{n+1} denotes the updated cohesive force, and $\Delta\gamma^p$ is the plastic slip.

The steps necessary to calculate f_N and f_T are summarized in Box 1. Note that because the load increment is finite and the particle assembly may be locally discontinuous, it may happen that during the iteration a new contact is formed between two previously disconnected particles. Unless a very small load increment is employed, it may never be known when the initial contact is actually formed between these two particles. Box 1 thus presents two options to bracket the expected response. For IOPT = 1, initial contact is assumed to take place at time t_{n+1}, in which case, $(f_T)_{n+1}$ becomes identically equal to zero (see Step 3); for IOPT = 0, initial contact is assumed to take place instantaneously at time t_n.

Box 1. Contact force calculations.

```
Step 1. Compute $\delta_{n+1}$, $(f_N)_{n+1} = -H_\varepsilon(\delta_{n+1}) k_N \delta_{n+1}$.
Step 2. If $(f_N)_{n+1} \geq 0$, $(f_N)_{n+1} = (f_T)_{n+1} = 0$ and return.
Step 3. If $\delta_n = 0$ and IOPT $= 1$, $(f_T)_{n+1} = 0$ and return.
Step 4. Compute $\Delta\gamma$.
Step 5. Compute $(f_T)_{n+1} = (f_T)_n + H_\varepsilon k_T \Delta\gamma$.
Step 6. Compute $f_{\max} = \alpha_n - (f_N)_{n+1} \tan\phi$.
Step 7. If $|(f_T)_{n+1}| > f_{\max}$, $(f_T)_{n+1} = (\alpha_{n+1} - (f_N)_{n+1} \tan\phi)\,\mathrm{sign}(f_T)_{n+1}$.
Step 8. Return. □
```

Chapter 3

Micromechanical-Macromechanical Connections

3.1. Introduction

The particulate nature of granular materials causes the macroscopic applied loads to be carried at contact points between grains. Thus, employing continuum concepts to describe the overall response of a material with microstructure and particulate mechanics to describe of constituent particle motions presents a modeling challenge. For example, since stress represents a macroscopic continuum concept, its use for a particulate medium requires careful micromechanical considerations of particle contact force transmission. Likewise, the notion of macroscopic kinematic quantities demands special interpretation of the role micromechanics plays in describing the motion of individual particles. Hence, the overall stress and kinematic relationships establish crucial connections between the macromechanical description and the fundamental underlying particulate mechanics.

This chapter describes the connection between the particle contact forces and the overall stress. The kinematical description of the overall velocity gradient will also be considered in terms of an average of appropriate microscopic quantities. These two essential connections then form the basis for the macroscopic constitutive relation. The development of the criterion for predicting the onset of localized deformation follows naturally from this relation.

3.2. Macroscopic stress field

The overall stress acting on a particle assembly produces contact forces at contacting points of the constituent particles. Independent of the nature of these contacts, the basic objective in this section is to describe the overall stress in terms of the contact forces and some geometric characteristics of the granules.

Consider a representative sample of a granular mass of volume V and surface area S. Let two control volume particles A and B, with centroids at $\boldsymbol{x}^A$ and $\boldsymbol{x}^B$ respectively, have a contact point at $\boldsymbol{x}^{AB}$ as shown in Figure 3. The branch vector $\boldsymbol{l}^{AB}$ connects the centroid of particle A to the centroid of particle B and is given by

$$\boldsymbol{l}^{AB} = \boldsymbol{x}^B - \boldsymbol{x}^A . \tag{3.1}$$

Let $\boldsymbol{f}^{AB}$ and $\boldsymbol{f}^{BA}$ denote, respectively, the contact forces exerted on grain A by grain B and vice versa, and therefore $\boldsymbol{f}^{AB} = -\boldsymbol{f}^{BA}$.

Neglecting inertia and gravity terms the balance of linear momentum for particle A requires

$$\sum_{\beta=1}^{\kappa} \boldsymbol{f}^{A\beta} = \boldsymbol{0} , \tag{3.2}$$

where $\boldsymbol{f}^{A\beta}$ represents the contact forces exerted on particle A by particle β, and κ denotes the so-called coordination number for particle A (i.e., the number of particles contacting A).

The balance of angular momentum for particle A yields

$$\sum_{\beta=1}^{\kappa} \boldsymbol{f}^{A\beta} \times (\boldsymbol{x}^{A\beta} - \boldsymbol{x}^A) = \boldsymbol{0} , \tag{3.3}$$

where $\boldsymbol{x}^{A\beta}$ is the position vector of the contact point between particles A and β. Summing the contributions from all particles contained in the control volume gives

$$\sum_{\beta=1}^{N} \boldsymbol{f}^{\alpha} \times \boldsymbol{l}^{\alpha} = \boldsymbol{0} , \tag{3.4}$$

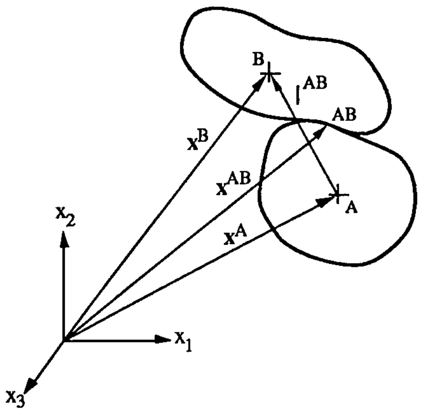

Figure 3. Two control volume particles with centroids at $\boldsymbol{x}^A$ and $\boldsymbol{x}^B$, contact point at $\boldsymbol{x}^{AB}$, and branch vector $\boldsymbol{l}^{AB}$.

where α represents a particle contact such as AB, and N denotes the total number of contacts in the control volume. An important implication of equation (3.4) is that it renders the following tensor symmetric

$$\sum_{\alpha=1}^{N} \boldsymbol{f}^\alpha \otimes \boldsymbol{l}^\alpha = \sum_{\alpha=1}^{N} \boldsymbol{l}^\alpha \otimes \boldsymbol{f}^\alpha . \tag{3.5}$$

To relate the contact forces to the macroscopic stress, the principle of virtual work is employed in the manner of Christoffersen et al. [29]. First, the overall stress, $\bar{\boldsymbol{\sigma}}$ is given by its natural definition [24, 25]

$$\bar{\boldsymbol{\sigma}} = \frac{1}{V} \int_V \boldsymbol{\sigma}(\boldsymbol{x}) \, \mathrm{d}V , \tag{3.6}$$

where $\boldsymbol{\sigma}(\boldsymbol{x})$ represents the variable stress field in equilibrium with the overall applied boundary traction $\boldsymbol{T}$, i.e.

$$\boldsymbol{\sigma} \cdot \bar{\boldsymbol{n}} = \boldsymbol{T} \qquad \text{on } S , \tag{3.7}$$

where $\bar{\boldsymbol{n}}$ denotes the exterior unit normal to S.

Now, consider a sufficiently smooth overall virtual displacement $\boldsymbol{u}$ that results in a virtual separation $\boldsymbol{\Delta}^\alpha$ of the αth contact force. Assuming that the traction $\boldsymbol{T}$

is in equilibrium with the contact forces $\boldsymbol{f}^{\alpha}$, the virtual work principle requires

$$\frac{1}{V}\int_S \boldsymbol{T}\cdot\boldsymbol{u}\,\mathrm{d}S = \sum_{\alpha=1}^{N} \boldsymbol{f}^{\alpha}\cdot\boldsymbol{\Delta}^{\alpha}\,. \tag{3.8}$$

Since the virtual displacement field can be chosen arbitrarily, consider the linear field

$$\boldsymbol{u} = \boldsymbol{\phi}\cdot\boldsymbol{x} + \boldsymbol{c}\,, \tag{3.9}$$

where $\boldsymbol{\phi}$ and $\boldsymbol{c}$ denote, respectively, an arbitrary second order tensor and an arbitrary vector. The virtual contact separation compatible with this field is given by

$$\boldsymbol{\Delta}^{\alpha} = \boldsymbol{\phi}\cdot\boldsymbol{l}^{\alpha}\,. \tag{3.10}$$

Appendix A shows that this representation of $\boldsymbol{\phi}\cdot\boldsymbol{l}^{\alpha}$ is reasonable to a first order approximation to $\boldsymbol{\Delta}^{\alpha}$.

Substituting (3.9) and (3.10) into (3.8) and employing the divergence theorem gives

$$\boldsymbol{\phi} : \left[\frac{1}{V}\int_V \boldsymbol{\sigma}(\boldsymbol{x})\,\mathrm{d}V - \sum_{\alpha=1}^{N} \boldsymbol{f}^{\alpha}\otimes\boldsymbol{l}^{\alpha}\right] = \boldsymbol{0}\,. \tag{3.11}$$

With the symmetry property (3.5) and the definition of the overall stress, equation (3.11) reduces to

$$\bar{\boldsymbol{\sigma}} = \frac{1}{2}\sum_{\alpha=1}^{N}(\boldsymbol{f}^{\alpha}\otimes\boldsymbol{l}^{\alpha} + \boldsymbol{l}^{\alpha}\otimes\boldsymbol{f}^{\alpha})\,. \tag{3.12}$$

Note that this expression is dimensionally consistent if N is interpreted as the number of contacts per unit volume. The derivation of the macroscopic stress $\bar{\boldsymbol{\sigma}}$ requires the assumption that the virtual displacements are small. Thus, the overall stress inherits a spatial definition, and $\bar{\boldsymbol{\sigma}}$ may be termed the overall Cauchy stress arising from the contact forces.

It is important to recognize that from each pair of contact forces at a given contact (i.e., $\boldsymbol{f}^{AB}$ or $\boldsymbol{f}^{BA}$ for contact AB) only one enters the summation in (3.12). The choice of the vector $\boldsymbol{l}^{\alpha}$ determines the choice of $\boldsymbol{f}^{\alpha}$ (i.e., when $\boldsymbol{l}^{\alpha} = \boldsymbol{l}^{AB}$, $\boldsymbol{f}^{\alpha} = \boldsymbol{f}^{AB}$). In this manner, at each contact, a pair of vectors $\boldsymbol{l}^{\alpha}$ and $\boldsymbol{f}^{\alpha}$ has a unique tensor product and contribution to the overall stress.

3.3. Macroscopic deformation field

In this section, the relationships between the macromechanical and micromechanical kinematic quantities will be described. Consider the same representative control volume composed of discrete particles, and again let V denote the volume and S the surface area. Recall that this volume represents a point in the macroscopic sense and that the overall quantities (stresses, deformations, etc.) are the macroscopic responses themselves. Now, assume a velocity field $\bar{\boldsymbol{v}} \in \Re^{n_{sd}}$ that is sufficiently smooth over the problem domain, i.e.,

$$\bar{\boldsymbol{L}} = \frac{\partial \bar{\boldsymbol{v}}}{\partial \boldsymbol{x}} = \text{constant in } \bar{V}\,, \tag{3.13}$$

where $\bar{V} = V \cup S$ is the closure of V, and $\bar{\boldsymbol{L}}$ is the uniform overall velocity gradient. Note from the overall velocity gradient $\bar{\boldsymbol{L}}$, the overall rate of deformation $\bar{\boldsymbol{D}}$ and spin $\bar{\boldsymbol{W}}$ can be evaluated via

$$\bar{\boldsymbol{D}} = \operatorname{symm}(\bar{\boldsymbol{L}})\,; \quad \bar{\boldsymbol{W}} = \operatorname{skew}(\bar{\boldsymbol{L}})\,; \quad \bar{\boldsymbol{L}} = \bar{\boldsymbol{D}} + \bar{\boldsymbol{W}}\,. \tag{3.14}$$

A micromechanical connection with (3.13) and (3.14) can be described in the manner of Nemat-Nasser and Mehrabadi [23].

Consider a unit cell centered at a point with position vector $\boldsymbol{x}$ experiencing a uniform velocity gradient $\bar{\boldsymbol{L}}$. As this unit cell shrinks to a point, one recovers the macroscopic definition (3.13). However, the cell must be large enough to contain a sufficient number of particles to capture the overall behavior of the material. Within the control volume the local velocity field $\boldsymbol{v} = \boldsymbol{v}(\boldsymbol{x})$ will not generally be a linear function of $\boldsymbol{x}$ but will vary according to the typically irregular particle motions. As a result, the associated velocity gradient $\boldsymbol{L}$ will also be irregular and is given by the expression

$$\boldsymbol{L} = \frac{\partial \boldsymbol{v}}{\partial \tilde{\boldsymbol{x}}}\,, \tag{3.15}$$

where $\tilde{\boldsymbol{x}}$ represents the position vector of a point in the neighborhood of $\boldsymbol{x}$ within the unit cell.

Applying the divergence theorem to (3.13) and (3.15) yields

$$\frac{1}{V}\int_S \bar{\boldsymbol{v}}\bar{\boldsymbol{n}}\,\mathrm{d}S = \frac{1}{V}\int_V \frac{\partial \bar{\boldsymbol{v}}}{\partial \boldsymbol{x}}\,\mathrm{d}V \equiv \bar{\boldsymbol{L}}\,, \tag{3.16}$$

and

$$\frac{1}{V}\int_S \boldsymbol{v}\bar{\boldsymbol{n}}\,\mathrm{d}S = \frac{1}{V}\int_V \frac{\partial \boldsymbol{v}}{\partial \widetilde{\boldsymbol{x}}}\,\mathrm{d}V \equiv \langle \boldsymbol{L} \rangle\,, \tag{3.17}$$

where the symbol $\langle \cdot \rangle$ denotes an average over the control volume, and $\bar{\boldsymbol{n}}$ again represents the exterior unit normal vector to S.

If the boundary particles move uniformly such that $\bar{\boldsymbol{v}} = \boldsymbol{v}$ on S, then the left-hand sides of (3.16) and (3.17) are identical, which implies that

$$\bar{\boldsymbol{L}} = \langle \boldsymbol{L} \rangle\,. \tag{3.18}$$

The physical meaning of this equation is that the macroscopic velocity gradient equals the volume average of the local particle velocity gradients.

Now, let $\Delta\bar{\boldsymbol{u}}$ be a sufficiently smooth macroscopic displacement field associated with the overall velocity field $\bar{\boldsymbol{v}}$, measured with respect to the configuration at time station t_n. Then, the updated position vector at any time $t > t_n$ is

$$\boldsymbol{x} = \boldsymbol{X}_n + \Delta\bar{\boldsymbol{u}}\,, \tag{3.19}$$

where $\boldsymbol{X}_n$ is the configuration at the beginning of the time step.

The associated overall deformation gradient for this motion is

$$\bar{\boldsymbol{F}} = \frac{\partial \boldsymbol{x}}{\partial \boldsymbol{X}} = \bar{\boldsymbol{F}}_n + \frac{\partial \Delta\bar{\boldsymbol{u}}}{\partial \boldsymbol{X}}\,, \tag{3.20}$$

where $\bar{\boldsymbol{F}}_n = \partial \boldsymbol{X}_n / \partial \boldsymbol{X}$. Now, if $\boldsymbol{X}_n$ is taken as the reference configuration, then (3.20) degenerates to

$$\bar{\boldsymbol{f}} = \frac{\partial \boldsymbol{x}}{\partial \boldsymbol{X}_n} = \boldsymbol{1} + \frac{\partial \Delta\bar{\boldsymbol{u}}}{\partial \boldsymbol{X}_n} \equiv \bar{\boldsymbol{F}} \cdot \bar{\boldsymbol{F}}_n^{-1}\,. \tag{3.21}$$

Since the overall velocity gradient $\bar{\boldsymbol{L}}$ is a spatial tensor, then

$$\begin{aligned}
\bar{\boldsymbol{L}} &= \dot{\bar{\boldsymbol{F}}} \cdot \bar{\boldsymbol{F}}^{-1} && (3.22)\\
&= \dot{\bar{\boldsymbol{f}}} \cdot \bar{\boldsymbol{F}}_n \cdot \bar{\boldsymbol{F}}_n^{-1} \cdot \bar{\boldsymbol{f}}^{-1} && (3.23)\\
&= \dot{\bar{\boldsymbol{f}}} \cdot \bar{\boldsymbol{f}}^{-1}\,, && (3.24)
\end{aligned}$$

i.e., $\bar{\boldsymbol{L}}$ does not depend on the choice of the reference configuration.

Equation (3.19) can be used to obtain the updated configuration at time t_{n+1} as

$$\boldsymbol{X}_{n+1} = \boldsymbol{X}_n + \Delta\bar{\boldsymbol{u}}_n \,. \tag{3.25}$$

Now, if $\Delta\bar{\boldsymbol{u}}_n$ is assumed to be a homogeneous function of degree one, then Euler's theorem for homogeneous functions gives

$$\Delta\bar{\boldsymbol{u}}_n = \frac{\partial\Delta\bar{\boldsymbol{u}}_n}{\partial\boldsymbol{X}_n} \cdot \boldsymbol{X}_n \equiv \boldsymbol{A} \cdot \boldsymbol{X}_n \,, \tag{3.26}$$

where $\boldsymbol{A} = \partial\Delta\bar{\boldsymbol{u}}_n/\partial\boldsymbol{X}_n$. The macroscopic velocity field associated with (3.26) is

$$\bar{\boldsymbol{v}} = \dot{\boldsymbol{A}} \cdot \boldsymbol{X}_n \,. \tag{3.27}$$

Substituting (3.26) and (3.21) into (3.24) gives the overall velocity gradient at time t_{n+1} as

$$\bar{\boldsymbol{L}} = \dot{\boldsymbol{A}} \cdot (\boldsymbol{1} + \boldsymbol{A})^{-1} \,. \tag{3.28}$$

Hence, for $\bar{\boldsymbol{L}}$ to have a uniform distribution over the control volume V, the tensor $\boldsymbol{A}$ should be spatially constant over V. Physically, the macroscopic tensor $\boldsymbol{A}$ provides a measure of the overall deformation experienced by the macroscopic point of interest.

Conceptually equation (3.26) indicates that if adjacent control volumes lie sufficiently close to each other, they may overlap. This observation is consistent in order for the macroscopic tensor $\boldsymbol{A}$ (and thus, the overall velocity gradient $\bar{\boldsymbol{L}}$) to have a sufficiently smooth distribution over the problem domain.

3.4. Macroscopic constitutive relation

A macroscopic constitutive relation will be useful for characterizing the overall behavior of the granular material in terms of its particulate nature. As will be seen in the next section, the macroscopic constitutive relation plays a central role in the development of the localization criterion for the material. Localization is interpreted herein as an instability in the macroscopic constitutive description of the inelastic deformation of a material. The constitutive equations will also be of particular importance in the development of the response of a macroscopic point to an applied overall stress history presented in Chapter 5.

The macroscopic constitutive relation depends heavily upon the micromechanical-macromechanical connections that bridge the continuum and particulate descriptions of the granular material. First, the dependency of the overall stress on these connections will be determined. The particle contact force integration presented in Section 2.4 provides the contact forces $\boldsymbol{f}^{\alpha}$ for evaluating the macroscopic stress $\bar{\boldsymbol{\sigma}}$ given in (3.12). The local constitutive relation describes these forces in terms of the particle's centroidal motion which in turn depends in part on the applied overall displacement gradient $\boldsymbol{A}$. In terms of overall quantities, an implicit macroscopic constitutive equation can be written to capture this relationship as follows:

$$\bar{\boldsymbol{\sigma}}_{n+1} = \bar{\boldsymbol{\sigma}}_{n+1}(\boldsymbol{A})\,, \tag{3.29}$$

i.e., the overall stress is a function of the components of the displacement gradient $\boldsymbol{A}$.

In principle, (3.29) can always be written in rate form. For example, differentiating (3.29) with respect to time and using (3.28) gives

$$\begin{aligned}
\dot{\bar{\boldsymbol{\sigma}}} &= \frac{\partial \bar{\boldsymbol{\sigma}}}{\partial \boldsymbol{A}} : \dot{\boldsymbol{A}} && (3.30)\\
&= \frac{\partial \bar{\boldsymbol{\sigma}}}{\partial \boldsymbol{A}} : \bar{\boldsymbol{L}} \cdot (\boldsymbol{1} + \boldsymbol{A}) && (3.31)\\
&= \boldsymbol{K} : \bar{\boldsymbol{L}}\,. && (3.32)
\end{aligned}$$

The fourth order tensor $\boldsymbol{K}$ represents an overall moduli tensor with components

$$K_{ijkl} = \frac{\partial \bar{\sigma}_{ij}}{\partial A_{km}}(\delta_{lm} + A_{lm})\,, \tag{3.33}$$

where δ_{lm} denotes the Kronecker delta. When the components of the displacement gradient $\boldsymbol{A}$ are small, then equation (3.33) reduces to

$$K_{ijkl} = \frac{\partial \bar{\sigma}_{ij}}{\partial A_{kl}}\,. \tag{3.34}$$

Since slip governs the microstructural rearrangement mechanism, a vertex will develop on the macroscopic yield surface [30,31]. In other words, the relation (3.32) will have an infinite number of branches corresponding to different directions of $\bar{\boldsymbol{L}}$. Thus, plastic 'normality' in conjugate deformation variables is lost [30], and the moduli tensor $\boldsymbol{K}$ is restricted to only minor symmetry

$$K_{ijkl} = K_{jilk}. \tag{3.35}$$

The minor symmetry of $\boldsymbol{K}$ with respect to the indices ij follows directly from the symmetry of $\bar{\boldsymbol{\sigma}}$. The minor symmetry with respect to the indices kl results from the fact that $\bar{\boldsymbol{L}}$ is rotation-free, i.e., from a macroscopic standpoint the strains are small. Thus, the tensor $\boldsymbol{K}$ can be used for small-strain stability analysis as demonstrated in the next section.

3.5. Localization criterion

Critical conditions are now sought at which the material's macroscopic constitutive relation may allow a bifurcation from a homogeneous or smoothly varying deformation into a highly concentrated non-uniform deformation in a planar band. Outside the localized band, the conditions of continuing equilibrium and continuing homogeneous deformation must be met. The onset of localization results from the loss of ellipticity of the continuing velocity equilibrium equation

$$\frac{\partial \dot{\bar{\boldsymbol{\sigma}}}}{\partial \boldsymbol{x}} = \boldsymbol{0}. \tag{3.36}$$

The problem is then to determine conditions at which (3.36) is satisfied across some planes of orientation $\boldsymbol{n}$.

Consider a macroscopically homogeneous, homogeneously deformed material subjected to quasi-static increments of deformation. For the velocity field to remain continuous at bifurcation, compatibility requires the velocity field to be expressed as

$$\bar{\boldsymbol{L}}^b = \bar{\boldsymbol{L}}^o + \boldsymbol{g}\boldsymbol{n}\,, \tag{3.37}$$

where superscripts b and o denote band and outside the band respectively, and $\boldsymbol{g}$ is a function only of the distance across the band, $\boldsymbol{n}\cdot\boldsymbol{x}$, and is zero outside the band.

The condition of continuing equilibrium (3.36) also demands that the traction be continuous across the discontinuity planes

$$\boldsymbol{n} \cdot \dot{\boldsymbol{\sigma}}^{o} = \boldsymbol{n} \cdot \dot{\boldsymbol{\sigma}}^{b}. \tag{3.38}$$

With (3.32), the constitutive equation inside the band is

$$\dot{\boldsymbol{\sigma}}^{b} = \boldsymbol{K}^{b} : \bar{\boldsymbol{L}}^{b}, \tag{3.39}$$

and substituting in (3.37) and (3.38) yields

$$\left(\boldsymbol{n} \cdot \boldsymbol{K}^{b} \cdot \boldsymbol{n}\right) \cdot \boldsymbol{g} = \boldsymbol{n} \cdot \left(\boldsymbol{K}^{o} - \boldsymbol{K}^{b}\right) : \bar{\boldsymbol{L}}^{o}. \tag{3.40}$$

A continuous constitutive response is assumed prior to localization, i.e., $\boldsymbol{K}^{o} = \boldsymbol{K}^{b}$. Thus, for a non-trivial solution for $\boldsymbol{g}$, the condition for localization becomes

$$\det\left[\mathcal{A}(\boldsymbol{n})\right] = \det\left[\boldsymbol{n} \cdot \boldsymbol{K} \cdot \boldsymbol{n}\right] = 0\,, \tag{3.41}$$

where $\mathcal{A} = \boldsymbol{n} \cdot \boldsymbol{K} \cdot \boldsymbol{n}$ is the so-called 'acoustic tensor.' Appendix B contains the details for calculating the orientation of the band $\boldsymbol{n}$ in two dimensions.

Chapter 4

Strain-driven Problem

4.1. Introduction

With the background of Chapter 2 and Chapter 3, a solution strategy may be constructed to derive the response of a macroscopic point in a granular material from the behavior of a particle assembly. The solution model adopts the conventional hypothesis in computational plasticity by assuming a deformation driven problem, i.e., the given overall displacement gradient determines the overall stress response. The mathematical formulation prescribes an overall uniform motion to an assembly of particles and then allows the particles to move in a microscopic sense. Throughout the particle motions, contacts may form or break altering the material's microstructure. The contact forces that develop between particles can then be used to evaluate the overall stresses.

This chapter considers the solution of the deformation driven problem in detail. The formulation is presented in the context of an analogy with the finite element method where the control volume particles represent nodes and their contacts denote elements. Special attention is given to the application of the uniform deformation to the assembly of particles. The notion of a repeating, or periodic, cell will be presented which allows the prediction of the overall response of the control volume without the imposition of boundary particle displacements.

4.2. Algorithm for problems with an imposed deformation history

Consider a two-dimensional assembly of rigid circular particles. Each particle contains two translation degrees of freedom in the x_1, x_2 plane and one rotational degree of freedom about the x_3 axis as shown in Figure 4. The constituent particles form a moving mesh where the particles have been replaced by nodes and the contacts are represented by the stick/slip elements of Chapter 2. The associated grid continually changes as particles move to new positions breaking contacts and forming new ones, i.e., severing contact elements and forming new ones.

The internal force vector at time t_{n+1} for a typical contact element number 'e' connecting particles A and B is given by

$$\boldsymbol{f}^e_{(6\times 1)} = \left\{ \boldsymbol{f}^A_{n+1}, r^A f_T, \boldsymbol{f}^B_{n+1}, r^B f_T \right\}^t , \tag{4.1}$$

where the balance of linear momentum (3.2) requires that $\boldsymbol{f}^A_{n+1} = -\boldsymbol{f}^B_{n+1}$. Recall that $\boldsymbol{f}^A_{n+1}$ and $\boldsymbol{f}^B_{n+1}$ represent that internal force vectors reckoned with respect to the Cartesian axes x_1, x_2 and the rotation matrix $\boldsymbol{R}$ relates them to the normal and tangential contact forces in $\mathcal{F}$ via

$$\boldsymbol{f}^A_{n+1} = \boldsymbol{R}^A_{n+1} \mathcal{F}^A_{n+1} , \tag{4.2}$$

where

$$\mathcal{F}_{n+1} = \{ f_N, f_T \}^t . \tag{4.3}$$

The corresponding particle degrees of freedom are

$$\boldsymbol{d}^e_{(6\times 1)} = \left\{ \boldsymbol{d}^A_{n+1}, \theta^A_{n+1}, \boldsymbol{d}^B_{n+1}, \theta^B_{n+1} \right\}^t , \tag{4.4}$$

where $\boldsymbol{d}^A_{n+1}$ represents the vector of unknown nodal displacements for particle A and θ^A_{n+1} denotes the unknown rotation of particle A (see Figure 4).

Imposing the momentum balance equation for every particle in the control volume and neglecting inertia and gravity terms results in an equilibrium equation of the form

$$\boldsymbol{F}_{INT}(\boldsymbol{d}_{n+1}) = \bigcup_{e=1}^{n_{el}} \boldsymbol{f}^e = \boldsymbol{0} , \tag{4.5}$$

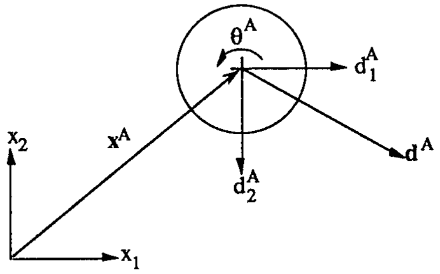

Figure 4. Particle degrees of freedom on the x_1, x_2 plane.

where the symbol $\bigcup$ denotes the assembly operator. To determine the vector of nodal displacements $\boldsymbol{d}_{n+1}$ that satisfies (4.5) at each time step, Newton's method with line search can be employed:

$$\boldsymbol{F}'_{INT}(\boldsymbol{d}^i_{n+1})\Delta\boldsymbol{d} = \boldsymbol{F}_{INT}(\boldsymbol{d}^i_{n+1})\,; \quad \boldsymbol{d}^{i+1}_{n+1} \leftarrow \boldsymbol{d}^i_{n+1} - \alpha\Delta\boldsymbol{d}; \quad \boldsymbol{d}^{i=0}_{n+1} \equiv \boldsymbol{d}_n\,, \tag{4.6}$$

where $0 < \alpha < 1$ is a line search parameter introduced to insure that the iteration (4.6) is norm-reducing [34,35]. In (4.6), $\boldsymbol{F}'_{INT}(\boldsymbol{d}^i_{n+1})$ denotes the algorithmic tangent operator derived from the element contribution

$$\boldsymbol{F}'_{INT}(\boldsymbol{d}^i_{n+1}) = \bigcup_{e=1}^{n_{el}} \boldsymbol{f}^{e\prime}(\boldsymbol{d}^e_{n+1})\,. \tag{4.7}$$

By definition, the solution has converged when

$$\|\boldsymbol{F}^i_{INT}\| / \|\boldsymbol{F}^0_{INT}\| < \mathrm{rtol}\,, \tag{4.8}$$

where rtol represents a prescribed error tolerance.

Taking the derivatives of (4.1) results in the following element contributions $\boldsymbol{f}^{e\prime}(\boldsymbol{d}^e_{n+1})$ to the tangent operator (omitting subscripts '$n+1$' for time step and superscripts 'i' for iteration counter, for simplicity):

$$\boldsymbol{f}^{e\prime}(\boldsymbol{d}^e) = \begin{bmatrix} \boldsymbol{f}'(\boldsymbol{d}^A) & \boldsymbol{f}'(\theta^A) & \boldsymbol{f}'(\boldsymbol{d}^B) & \boldsymbol{f}'(\theta^B) \\ r^A f'_T(\boldsymbol{d}^A) & r^A f'_T(\theta^A) & r^A f'_T(\boldsymbol{d}^B) & r^A f'_T(\theta^B) \\ -\boldsymbol{f}'(\boldsymbol{d}^A) & -\boldsymbol{f}'(\theta^A) & -\boldsymbol{f}'(\boldsymbol{d}^B) & -\boldsymbol{f}'(\theta^B) \\ r^B f'_T(\boldsymbol{d}^A) & r^B f'_T(\theta^A) & r^B f'_T(\boldsymbol{d}^B) & r^B f'_T(\theta^B) \end{bmatrix}_{(6\times 6)} \tag{4.9}$$

Box 2. Strain-driven algorithm.

```
i. Given $\boldsymbol{A}^{i+1}_{n+1}$, $\boldsymbol{A}_n$, and $i = 0$.
ii. Compute $\boldsymbol{F}'_{INT}(\boldsymbol{d}^i_{n+1})$.
iii. $\boldsymbol{d}^{i+1}_{n+1} = \boldsymbol{d}^i_{n+1} - \left[\boldsymbol{F}'_{INT}(\boldsymbol{d}^i_{n+1})\right]^{-1} \boldsymbol{r}^i$.
iv. $\boldsymbol{r}^{i+1} = \bigcup_{e=1}^{n_{el}} \boldsymbol{f}^e(\boldsymbol{d}^{i+1}_{n+1})$.
v. IF $\|\boldsymbol{r}^{i+1}\|/\|\boldsymbol{r}^0\| < \text{rtol}$, GO TO 5.
vi. $i \leftarrow i + 1$ and GO TO ii. $\square$
```

where

$$\boldsymbol{f}'(\boldsymbol{d}^A) = -\boldsymbol{f}'(\boldsymbol{d}^B); \quad r^B \boldsymbol{f}'(\theta^A) = r^A \boldsymbol{f}'(\theta^B); \tag{4.10}$$

$$f'_T(\boldsymbol{d}^A) = -f'_T(\boldsymbol{d}^B); \quad r^B f'_T(\theta^A) = r^A f'_T(\theta^B). \tag{4.11}$$

Appendix C contains a complete discussion of the derivatives contained in (4.9).

In general, the matrix $\boldsymbol{F}'_{INT}(\boldsymbol{d}^i_{n+1})$ will be neither symmetric nor positive definite. Furthermore, it may be singular with isolated particles or clusters of particles. The matrix $\boldsymbol{F}'_{INT}(\boldsymbol{d}^i_{n+1})$ may have a changing bandwidth from iteration to iteration as a consequence of new contacts being formed and old contacts being broken. Section 4.4 discusses these numerical issues in detail.

Box 2 contains the steps necessary for solving a deformation-driven problem. The algorithm depends heavily upon the calculation of the internal force vector $\boldsymbol{f}^e(\boldsymbol{d}_{n+1})$ which represents the particle contact force contribution to the internal force. Recall that Chapter 2 described the role that the spring stiffnesses k_N and k_T play in the contact constitutive equations used for calculating the contact forces. In the context of the deformation-driven problem of Box 2, these spring stiffnesses may be considered as penalty parameters rather than as physical measures of the true particle rigidities.

4.3. The notion of a repeating cell

The dependence of the vector $\boldsymbol{f}^e$ on the imposed displacement gradients $\boldsymbol{A}$ follows directly from the initial imposition of a uniform motion of the particle centroids according to (3.25) and (3.26). Assume that the particle centroids are given by $\boldsymbol{X}_n^A, A = 1, 2, \ldots, N$, then the new configuration of a typical particle A can be written as

$$\tilde{\boldsymbol{x}}^A = (\boldsymbol{1} + \boldsymbol{A}) \cdot \boldsymbol{X}_n^A \,. \tag{4.12}$$

This motion will generally perturb the momentum balance equations as contacting particles either separate, overlap, or slip during the uniform motion. The unbalanced forces create residuals in the force vector,

$$\boldsymbol{r} = \boldsymbol{F}_{INT}(\boldsymbol{A} \cdot \boldsymbol{X}_n^A) \neq \boldsymbol{0} \,, \tag{4.13}$$

where (4.12) has been used as an initial estimate for Newton's method (4.6). The continued dependence of $\boldsymbol{f}^e$ on $\boldsymbol{A}$ follows from the dissipation of the residual vector $\boldsymbol{r}$. Through the Newton iteration, the particles seek their equilibrium configuration while the sides of the control volume are held fixed according to the displacements produced by $\boldsymbol{A}$. Thus, the sides of the unit cell constrain the particles to move according to the deformed configuration imposed by $\boldsymbol{A}$.

As the iterations progress, the particles will translate and rotate to find their equilibrium positions, which could be drastically different from the imposed uniform motion. Hence, it may happen that $\boldsymbol{v} \neq \bar{\boldsymbol{v}}$ even on S, and so one cannot simply prescribe the motion of the boundary particles in order to constrain the problem. To determine the particle motion that is independent of the boundary displacements, the notion of a repeating, or periodic, cell has been employed.

Periodicity of the unit cell requires that the control volume of interest be surrounded in all directions by identical parallelepipeds (or rhombuses, in two dimensions). Physically, the notion of a periodic cell means that if a particle leaves the control volume an identical mirror image particle will enter the unit cell from a contiguous unit cell. Periodicity can be enforced for each pair of potentially contacting particles, A and B, by assuming that particle A could be in contact with

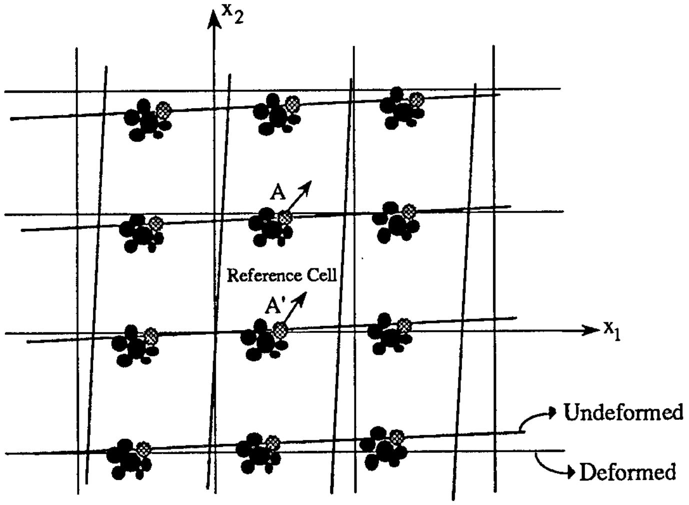

Figure 5. Periodic control volume subjected to a uniform deformation. As a particle A leaves the reference cell an identical mirror image particle A' enters the cell.

either B or one of the images of B in a neighboring parallelepiped (or rhombus). Figure 5 shows a graphical representation of how periodicity may be imposed for implicit two-dimensional plane-strain calculations.

In order to describe the basic repeating unit cell, let the basis vectors $(\boldsymbol{\Phi}_1, \boldsymbol{\Phi}_2, \ldots, \boldsymbol{\Phi}_{n_{sd}})$ represent the sides of a parallelepiped (or rhombus) that defines the control volume V in the reference configuration. Assume that one corner of the parallelepiped (or rhombus) coincides with the origin of the reference frame so that the $\boldsymbol{\Phi}_i$'s become the position vectors of the corners of V. In addition, let the vectors $(\boldsymbol{\varphi}_1, \boldsymbol{\varphi}_2, \ldots, \boldsymbol{\varphi}_{n_{sd}})$ represent the sides of the same volume in the current configuration such that

$$\boldsymbol{\varphi}_i = (\mathbf{1} + \boldsymbol{A}) \cdot \boldsymbol{\Phi}_i\,, \quad i = 1, 2, \ldots, n_{sd}\,. \tag{4.14}$$

Now, let A and B represent two potentially contacting particles with respective centroids at $\tilde{\boldsymbol{x}}^A$ and $\tilde{\boldsymbol{x}}^B$, measured with respect to the current configuration. With respect to the basis vectors $\boldsymbol{\varphi}_i$, the branch vector connecting the particle centroids $\tilde{\boldsymbol{x}}^A$ and $\tilde{\boldsymbol{x}}^B$ can be written as

$$\tilde{\boldsymbol{x}}^B - \tilde{\boldsymbol{x}}^A = \alpha_i \boldsymbol{\varphi}_i\,, \tag{4.15}$$

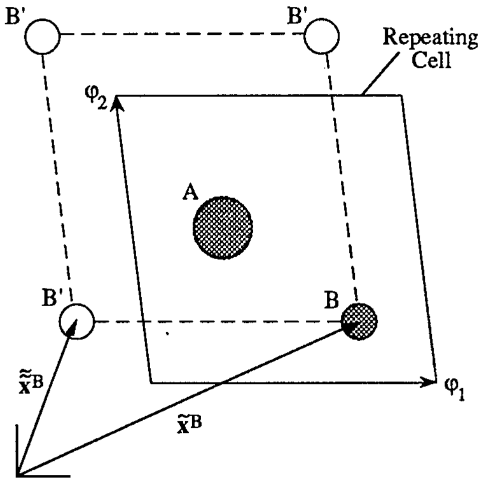

Figure 6. Enforcement of the periodicity condition: contacts are checked between A and B, and between particle A and the three image particles B'.

where a sum is implied on $i = 1, 2, \ldots, n_{sd}$, and the α_i's are some determinate multipliers. Since the $\boldsymbol{\varphi}_i$'s form a basis, then the α_i's are all distinct.

Now, periodicity of the cell can be imposed by assuming that particle B and its images are located at the corners of a parallelepiped (or rhombus) that is identical to the unit cell of interest and inscribes the centroid of particle A as shown in Figure 6. In terms of the current configuration vectors $\boldsymbol{\varphi}_i$, the centroidal coordinates of particle B and its images are given by

$$\tilde{\tilde{\boldsymbol{x}}}^B = \tilde{\boldsymbol{x}}^B - \beta_i \boldsymbol{\varphi}_i \, , \tag{4.16}$$

where a sum is again implied on i, and the β_i's are permutations of $(0, \mathrm{sign}(\alpha_i))$. For example, when $\beta_1 = \beta_2 = \ldots = \beta_{n_{sd}} = 0$, then $\tilde{\tilde{\boldsymbol{x}}}^B = \tilde{\boldsymbol{x}}^B$, which is the centroidal position vector for particle B; when $\beta_1 = \mathrm{sign}(\alpha_1)$ and $\beta_2 = \ldots = \beta_{n_{sd}} = 0$, then $\tilde{\tilde{\boldsymbol{x}}}^B = \tilde{\boldsymbol{x}}^B - \mathrm{sign}(\alpha_1)\boldsymbol{\varphi}_1$, which is the centroidal position vector for an image of B, and so on. Figure 6 shows a graphical representation of the enforcement of the periodicity condition for implicit two-dimensional plane-strain calculations.

Note that if particle A lies in contact with B, it can never be in contact with any of the images of B. The element contributions to the residual force vector $\boldsymbol{r}$ represent particle contact element contributions and not particle contributions. Thus, one and only one contact force vector can be added to the residual regardless of the multiplicity of the particle images.

An important feature of the periodic cell lies in its ability to allow the prediction of the macromechanical response without the imposition of boundary particle displacements. However, since periodic cells inherently contain zero-energy modes, the periodicity condition alone does not guarantee a fully constrained boundary-value problem. Rigid-body modes may be eliminated by fixing the motion of any one particle in V, provided that this particle belongs to the 'principal force chain.' Rigid-body modes cannot be removed by fixing an isolated particle, nor any particle in an isolated cluster. The next section discusses numerical examples and implications of the periodic cell and zero-energy modes.

4.4. Numerical simulations

This section presents the results of two-dimensional plane-strain simulations on granular assemblies composed of either regular or random initial packings of circular disks. Some fundamental properties of granular materials are demonstrated such as softening and anisotropy. Numerical difficulties encountered during the simulation process are reported as well. Unless otherwise stated, Table 1 defines the model parameters used in all analyses. The overall stresses have been calculated using a volume equal to the initial cross sectional area A_0 times a unit thickness. The error tolerance rtol used in (4.8) ensures that the iteration has converged sufficiently, thus minimizing the propagation of numerical errors.

Sixty four-particle regular assembly

The initial granular assembly configuration is shown in Figure 7. In this example, the assembly is assumed to be composed of 64 uniform circular particles of radius $r = 1.0$ units and arranged initially in simple cubic packing except that the adjacent rows of particles have been shifted by 5 degrees. The particle on the lower

Table 1. Model parameters.

Error tolerance: rtol $= 1.0 \times 10^{-8}$.

Normal spring stiffness: $k_N = 1.0 \times 10^4$.

Tangential spring stiffness: $k_T = 1.0 \times 10^4$.

Particle friction angle: $\phi = 30°$.

Particle contact cohesion: $\alpha_0 = 0$.

Contact hardening parameter: $H' = 100$.

Ramp function parameter: $\epsilon = 0.10$.

---

left-hand corner was fixed against translation and rotation to arrest the zero-energy modes present in the assembly.

The assembly was then subjected to combined isotropic compression and shear by prescribing ten increments of motion, each increment defined by the following elements of the tensor operator $\boldsymbol{A}$ in (3.26): $A_{11} = A_{22} = -1.0 \times 10^{-3}$, $A_{12} = A_{21} = -1.0 \times 10^{-2}$. If second-order deformations are ignored, then the total motion corresponds to normal compressions of $\bar{\epsilon}_{11} = \bar{\epsilon}_{22} = -1\%$ and tensorial shear strains of $\bar{\epsilon}_{12} = \bar{\epsilon}_{21} = -10\%$. The final deformed configuration after running the analysis over ten time steps appears in Figure 8.

Figure 8 shows that during the course of deformation, rows of particles have separated into four isolated clusters. This "strain-softening" effect is a typical result when a granular medium with an initially collapsible structure is subjected to shearing deformation which is far beyond the material's ability to compact. Numerically, this phenomenon will manifest in the form of zeros appearing on the diagonal of the factorized tangent operator, which are not operated upon during the back substitution process.

A different result can be obtained with a slightly altered strain history. Using the same initial configuration of Figure 7, the following overall uniform motions are now prescribed: one time step of $A_{11} = A_{22} = -1.0 \times 10^{-2}$, $A_{12} = A_{21} = 0$; followed by one-hundred time steps of $A_{21} = -1.0 \times 10^{-3}$, $A_{11} = A_{22} = A_{12} = 0$. If second-order effects are ignored, this motion corresponds to a total volumetric strain of $\bar{\epsilon}_{11} + \bar{\epsilon}_{22} = -2\%$ followed by a sidesway of 10% (which produces simple shearing and rigid body rotation). Results of the simulations are shown in Figure 9 and Figure 10.

Figure 9 shows the final deformed configuration characterized by a stable microstructure. The isotropic compression produces prestressing effects on the elastic springs and prevents the particle contacts from breaking during the shearing process. Since shearing involved essentially horizontal particle translation and scraping, the overall response of the assembly is a direct function of the tangential spring constant k_T. Thus, for a constant H'/k_T, the overall stresses can be normalized with respect to the spring constant k_T.

In Figure 10, the normalized overall shear stress, $\bar{\sigma}_{12}/k_T$, is plotted versus the overall tensorial shear strain, $\bar{\epsilon}_{12}$. Specifically, the overall shear stress is evaluated from (3.12) as

$$\bar{\sigma}_{12} = \frac{1}{2} N \langle f_1^\alpha l_2^\alpha + l_2^\alpha f_1^\alpha \rangle \tag{4.17}$$

The initial straight-line portion of the overall stress-strain plot represents the elastic stretching of the tangential springs, and is thus also normalizable with respect to the spring constant k_T. On the other hand, decreasing the moduli ratio H'/k_T decreases the $\bar{\sigma}_{12}/k_T$-response at post-yield. The 5-degree initial offset between adjacent rows of particles causes sequential yielding at contact points, thereby resulting in non-uniform tangential shear moduli at post-yield.

Sixty-particle periodic assembly

The initial configuration for this example is the same as in Figure 7 but with four interior particles removed so that the resulting assembly is represented by four repeating cells. The entire assembly is subjected to 50 increments of motion, each increment defined by the following elements of $\boldsymbol{A}$: $A_{11} = A_{22} = -4.0 \times 10^{-4}$, $A_{21} = A_{12} = 1.0 \times 10^{-3}$. If second-order effects are ignored, then the total motion is equivalent to a total volumetric strain of $\bar{\epsilon}_{11} + \bar{\epsilon}_{22} = -2\%$ and a total tensorial shear strain of $\bar{\epsilon}_{12} = \bar{\epsilon}_{21} = 5\%$. The resulting deformed configuration, shown in Figure 11, shows the expected periodicity exhibited by the deformed assembly. If this problem had been analyzed using only one of the four repeating cells, then the macroscopic stresses obtained from the sum of the contact forces for each reduced cell would have been one-fourth of those obtained from the full unit cell.

Fifty eight-particle irregular assembly

The initial configuration of the control volume for this example is shown in Figure 12. Here, the repeating cell resembles the one used in the sixty four-particle simulation except that six of the original particles in the assembly were removed. The control volume was subjected to 38 incremental motions, each increment described by the following elements of $\boldsymbol{A}$: $A_{11} = A_{22} = -7 \times 10^{-4}$ and $A_{12} = A_{21} = 1 \times 10^{-3}$. After the final load step, the deformed configuration is shown in Figure 13.

Figure 13 shows the deformed configuration for the case where no particle in the assembly was fixed against rigid-body motion. When this problem was run with the particle on the lower left-hand corner fixed against translation and rotation, then the results were the same except for the rigid-body modes. Thus, provided that the assembly remains stable, rigid-body modes may be allowed without afflicting the computed overall stress-strain response. In both configurations particle contacts have broken, and new contacts formed.

Figure 14 and Figure 15 show overall stress-strain curves for this example. The 58-particle assembly has been subjected to a total strain of $\bar{\epsilon}_{11} = \bar{\epsilon}_{22} = -2.66\%$ and $\bar{\epsilon}_{12} = \bar{\epsilon}_{21} = -3.8\%$. Several observations already mentioned from the previous examples may be noted again from these results: (a) for a constant H'/k_T, the overall stresses normalized with respect to k_T are the same; (b) fixing a particle in the assembly does not affect the resulting overall stress-strain curve; (c) structural anisotropy is created by the irregular particle assembly; and (d) continued volume-preserving shearing deformation produces an overall softening response. Observation (c) is evident in Figure 14 which shows that during isotropic compression, $\bar{\sigma}_{11}$ does not equal to $\bar{\sigma}_{22}$ even though $\bar{\epsilon}_{11}$ equals $\bar{\epsilon}_{22}$. Observation (d) may be qualified —

the overall response may harden once again as more stable contacts form from a collapsed microstructure, as evidenced by the hardening response represented by the tail of the stress-strain curve of Figure 15.

Finally, the overall stress-strain curve of Figure 16 represents the response of the same 58-particle assembly to the following imposed strain history: (a) total isotropic compression of $\bar{\epsilon}_{11} = \bar{\epsilon}_{22} = -1.0 \times 10^{-2}$; (b) simple shear of $\Delta\bar{\epsilon}_{12} = \Delta\bar{\epsilon}_{21} = -2.2 \times 10^{-2}$; (c) additional isotropic compression of $\Delta\bar{\epsilon}_{11} = \Delta\bar{\epsilon}_{22} = -1.0 \times 10^{-2}$; and (d) simple shear of $\Delta\bar{\epsilon}_{12} = \Delta\bar{\epsilon}_{21} = -2.8 \times 10^{-2}$. The simple shear is applied in steps of $\Delta\bar{\epsilon}_{12} = \Delta\bar{\epsilon}_{21} = -1.0 \times 10^{-3}$. Both the initial and intermediate isotropic compression stages resulted in a change in the overall shear stress $\bar{\sigma}_{12}$ due to anisotropy effects. The application of an intermediate isotropic compression was necessitated by the deteriorating numerical conditioning of the problem, manifested in the form of lack of quadratic convergence in Newton iteration, as the overall stress response reaches a plateau. The additional isotropic compression is seen to have resulted in a gain of shear strength.

One hundred ninety six-particle random assembly

The assembly is composed of 196 randomly arranged circular disks of varying sizes having a mean radius of $r_{\text{ave}} = 0.0092$ units and contained in a cell of dimensions 0.2566 units × 0.2564 units. The initial positions of the particles are shown in Figure 17, and are identical to those used in [36]. The control volume has 410 initial contacts and an initial void ratio of 0.1426 (i.e., ratio between total area of voids to total area of circles) representing a dense packing. To ensure that there are no "numerical slacks" between adjacent particles due to initial placement, and that the particles are indeed touching at the contact points, the control volume was isotropically compressed to initial macroscopic strains of $\bar{\epsilon}_{11} = \bar{\epsilon}_{22} = -1.0\%$.

The numerical algorithm is next tested for convergence. The control volume is compressed further to additional isotropic strains of $\Delta\bar{\epsilon}_{11} = \Delta\bar{\epsilon}_{22} = -1\%$ applied in one, two, four, 10, 20, 50, and 100 increments. Table 2 shows the predicted incremental macroscopic normal stresses, $\Delta\bar{\sigma}_{11}$ and $\Delta\bar{\sigma}_{22}$, at cumulative incremental normal strains of $\Delta\bar{\epsilon}_{11} = \Delta\bar{\epsilon}_{22} = -0.5\%$ and $\Delta\bar{\epsilon}_{11} = \Delta\bar{\epsilon}_{22} = -1.0\%$. Note

Table 2. Convergence test for the 196-particle assembly: isotropic compression ($k_N = k_T = 1 \times 10^4$ units).

Cumulative incremental strain, $\Delta\bar{\epsilon}_{11} = \Delta\bar{\epsilon}_{22} = -0.5\%$:

Strain increment, %	Stress $\Delta\bar{\sigma}_{11}$	Stress $\Delta\bar{\sigma}_{22}$
1.00	n/a	n/a
0.50	45.2789	40.8908
0.25	44.9810	40.6005
0.10	44.7728	40.4470
0.05	44.7013	40.3923
0.02	44.6572	40.3589
0.01	44.6420	40.3467

Cumulative incremental strain, $\Delta\bar{\epsilon}_{11} = \Delta\bar{\epsilon}_{22} = -1.0\%$:

Strain increment, %	Stress $\Delta\bar{\sigma}_{11}$	Stress $\Delta\bar{\sigma}_{22}$
1.00	110.8596	100.1927
0.50	109.6300	99.2609
0.25	108.9399	98.7138
0.10	108.4900	98.4174
0.05	108.3350	98.3125
0.02	108.2407	98.2502
0.01	108.2088	98.2289

n/a = not applicable

in Table 2 that the resulting normal stresses are not the same due to anisotropy effects. In fact, a non-zero macroscopic shear stress of $\Delta\bar{\sigma}_{12}$ is also produced by this simple isotropic compression. The results shown in Table 2 demonstrates that the algorithm is convergent under an isotropic strain field, and that for a volumetric compression of $\Delta\bar{\epsilon}_v = \Delta\bar{\epsilon}_{11} + \Delta\bar{\epsilon}_{22} = -2.0\%$ the error of the one-step solution for the normal stress sum, $\Delta\bar{\sigma}_{11} + \Delta\bar{\sigma}_{22}$, is in the order of 2.2% relative to the 100-step solution.

Next, the algorithm is tested for convergence under a simple shear strain field. The initial condition for this experiment is the final configuration that resulted from the one-step solution of Table 2 (i.e., under cumulative normal strains of $\bar{\epsilon}_{11} = \bar{\epsilon}_{22} = -2.0\%$). From this initial condition, the control volume is then subjected

Table 3. Convergence test for the 196-particle assembly: simple shear ($k_N = k_T = 1 \times 10^4$ units).

Cumulative incremental strain, $\Delta\bar{\epsilon}_{12} = \Delta\bar{\epsilon}_{21} = -0.5\%$:

Strain increment, %	Stress $\Delta\bar{\sigma}_{12} = \Delta\bar{\sigma}_{21}$
−0.50	−21.1606
−0.25	−21.1393
−0.20	n/a
−0.10	−21.1180
−0.05	−21.1104
−0.01	−21.1028

Cumulative incremental strain, $\Delta\bar{\epsilon}_{12} = \Delta\bar{\epsilon}_{21} = -1.0\%$:

Strain increment, %	Stress $\Delta\bar{\sigma}_{12} = \Delta\bar{\sigma}_{21}$
−0.50	n/c
−0.25	n/c
−0.20	−40.0290
−0.10	−40.0154
−0.05	−40.0078
−0.01	−40.0002

n/a = not applicable; n/c = no convergence

to a total simple shear strain of $\bar{\epsilon}_{12} = -1.0\%$ applied in two, four, five, 10, 20, and 100 steps. Results of the convergence study are shown in Table 3 and suggest that, again, the algorithm is convergent in the sense that there exists a shear stress to which the solution tends as the number of steps is increased. However, iterations for the two- and the four-step solutions failed to provide a convergent solution on the last load step.

Note that the strains in the order of 1% are generally considered "small" in the macroscopic sense. However, in the microscopic level, imposed macroscopic strains of this order could produce significant relative motion between adjacent particles, and thus, can hardly be considered "small." Existing numerical solutions [19–22, 26–28] often limit the macroscopic strain increments to values well below 1% in order that the difficulty associated with numerical conditioning may be circumvented. An important feature of the proposed model lies in its ability to provide convergent results even for macroscopic strain fields in the order of 0.1 to 1.0%.

Using the same initial configuration of Figure 17, the particle assembly now experiences a complex strain path characterized by alternating isotropic compression and simple shear. Figure 18 shows a plot of the overall shear stress $\bar{\sigma}_{12}$ versus overall tensorial shear strain $\bar{\epsilon}_{12}$ for the 196-particle assembly. The strain history for this problem is such that the assembly is compressed isotropically by an amount of $\Delta\bar{\epsilon}_{11} = \Delta\bar{\epsilon}_{22} = -1.0\%$ each time that the shear stress-shear strain curve reaches a plateau. Thus, re-hardening takes place immediately after each isotropic compression. The deformed configuration at total strains of $\bar{\epsilon}_{11} = \bar{\epsilon}_{22} = -3\%$ and $\bar{\epsilon}_{12} = -4.5\%$ are shown in Figure 19.

In a separate parametric study, Figure 20 shows that the macroscopic shear stress-shear strain response is not significantly influenced by the assumption of when a contact is initially formed between two previously non-overlapping particles. Recall that for IOPT = 1, initial contact is assumed to take place at time t_{n+1} if contact is detected between two previously separated particles; if IOPT = 0, contact is assumed to take place at time t_n (see Box 1). Since Figure 20 shows that the predicted results are nearly the same, either assumption may be employed in the analysis. The use of IOPT = 0 seems to generally lead to a more stable numerical solution.

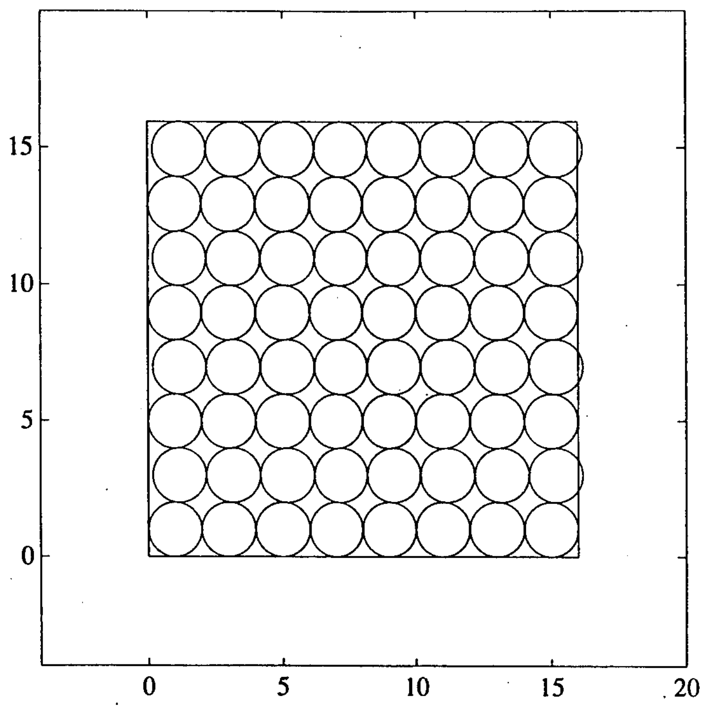
15
10
5
0
0
5
10
15
20

Figure 7. Initial configuration for the 64-particle control volume; particle radius = 1.0 units.

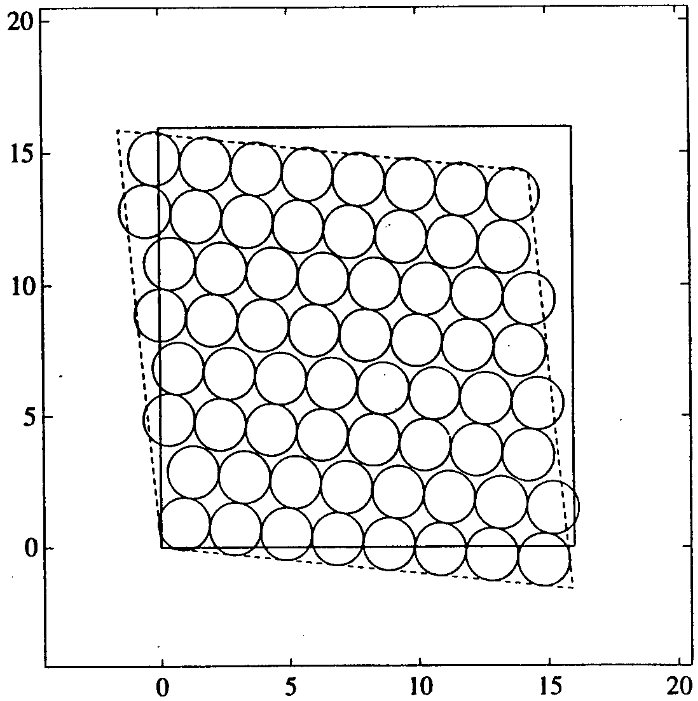
20
15
10
5
0
0
5
10
15
20

Figure 8. Isolated clusters of particles form from an initially loose packing of circular disks; particle radius = 1.0 units.

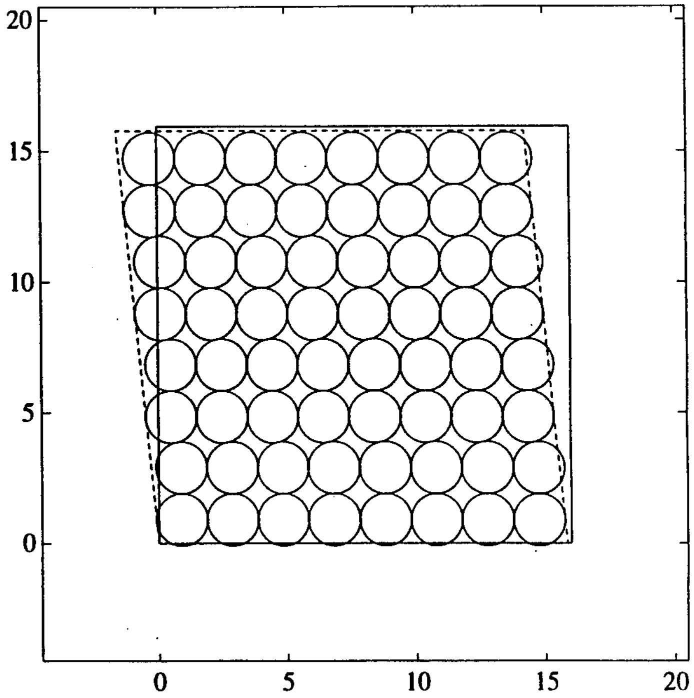
20
15
10
5
0
0
5
10
15
20

Figure 9. Isotropic compression followed by lateral shearing for the 64-particle assembly; particle radius = 1.0 units.

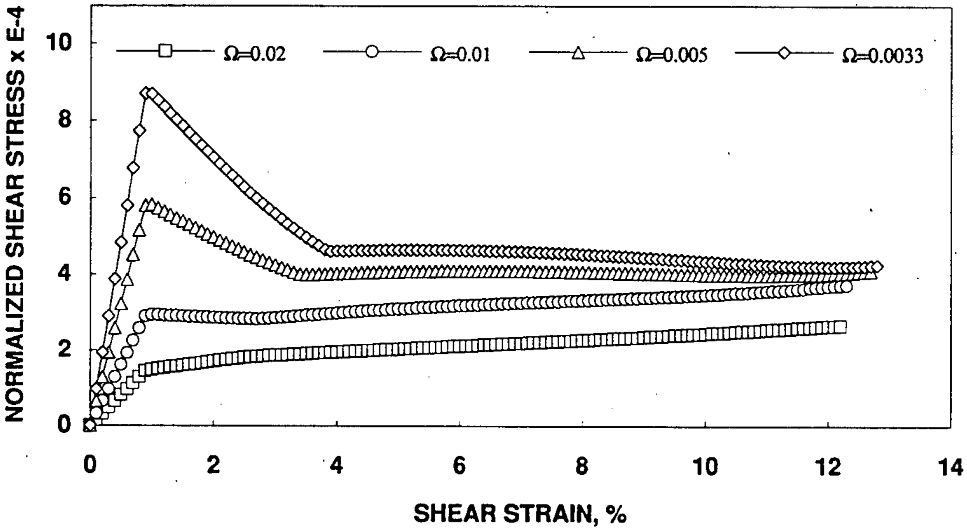

Figure 10. Normalized overall shear stress $\bar{\sigma}^*_{12}/k_T$ versus overall shear strain $\bar{\epsilon}_{12}$ showing the effects of the moduli ratio $= H'/k_T$.

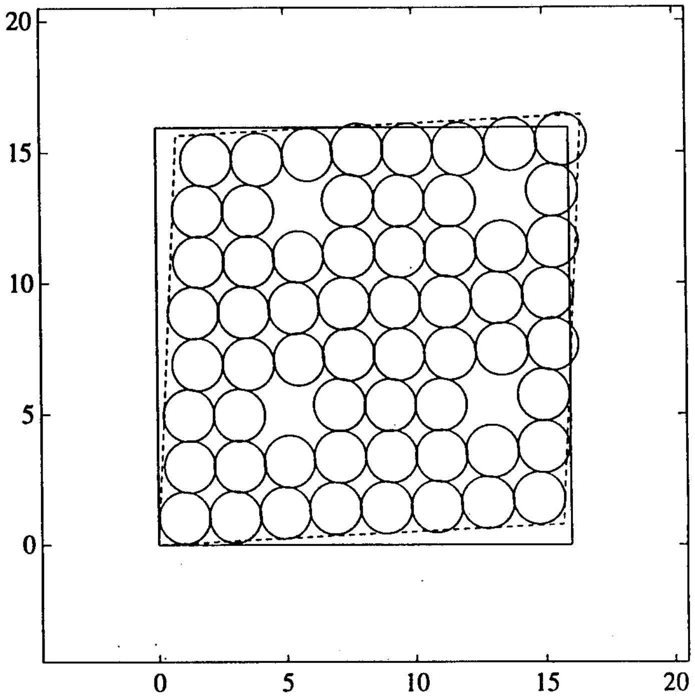
20
15
10
5
0
0
5
10
15
20

Figure 11. Periodicity test: deformed configuration for the 60-particle control volume; particle radius = 1.0 units.

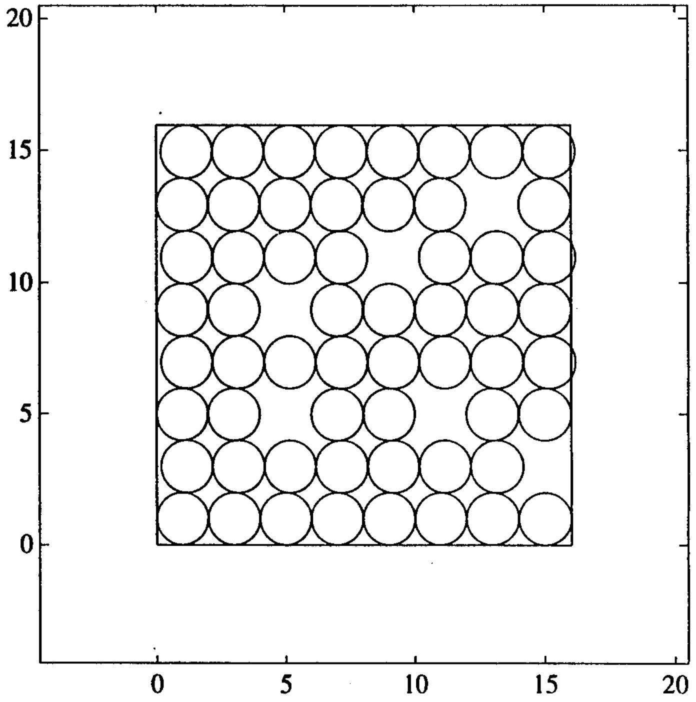

20
15
10
5
0
0
5
10
15
20

Figure 12. Initial configuration for the 58-particle control volume; particle radius = 1.0 units.

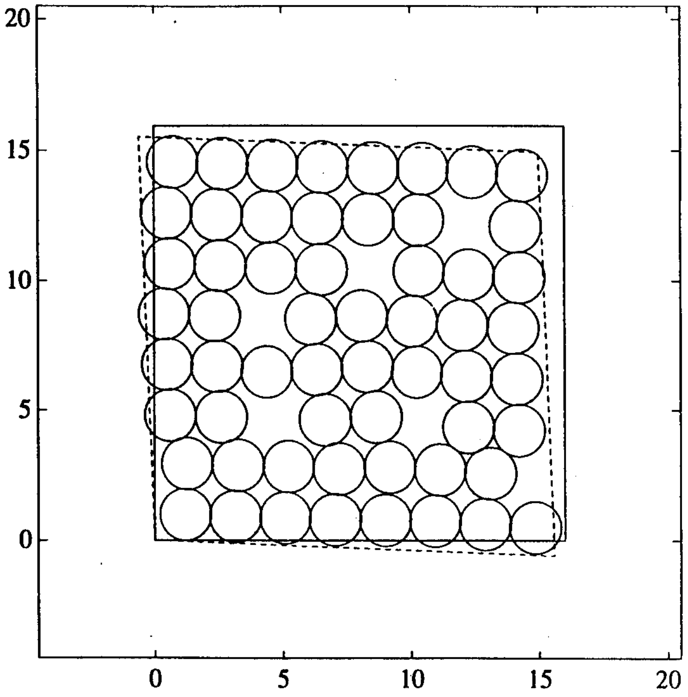
20
15
10
5
0
0
5
10
15
20

Figure 13. Deformed configuration for the 58-particle control volume showing zero-energy modes when the assembly is fully unconstrained; particle radius = 1.0 units.

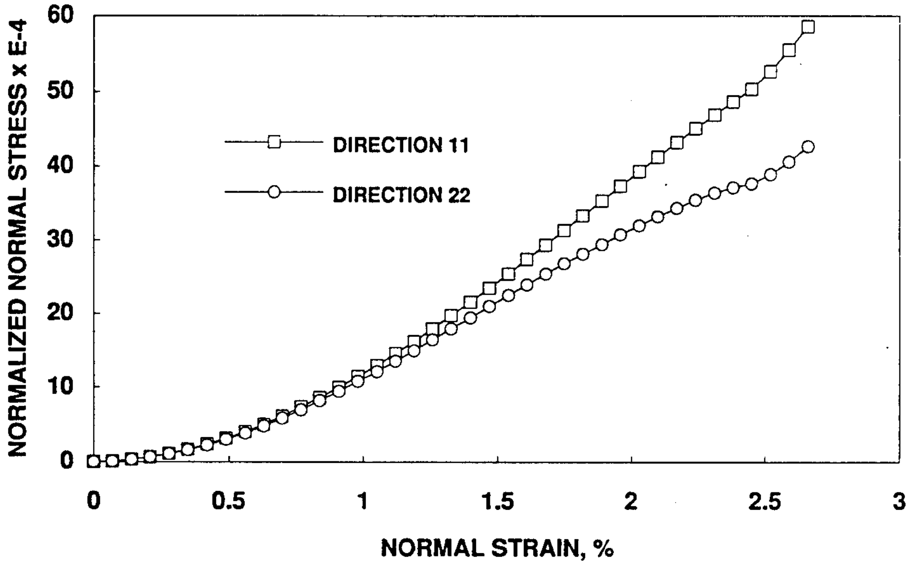

Figure 14. Normalized overall normal stresses $\bar{\sigma}^*_{11}/k_T$ and $\bar{\sigma}^*_{22}/k_T$ versus overall normal strains $\bar{\epsilon}_{11}$ and $\bar{\epsilon}_{22}$, respectively, showing the effects of structural anisotropy for the 58-particle assembly.

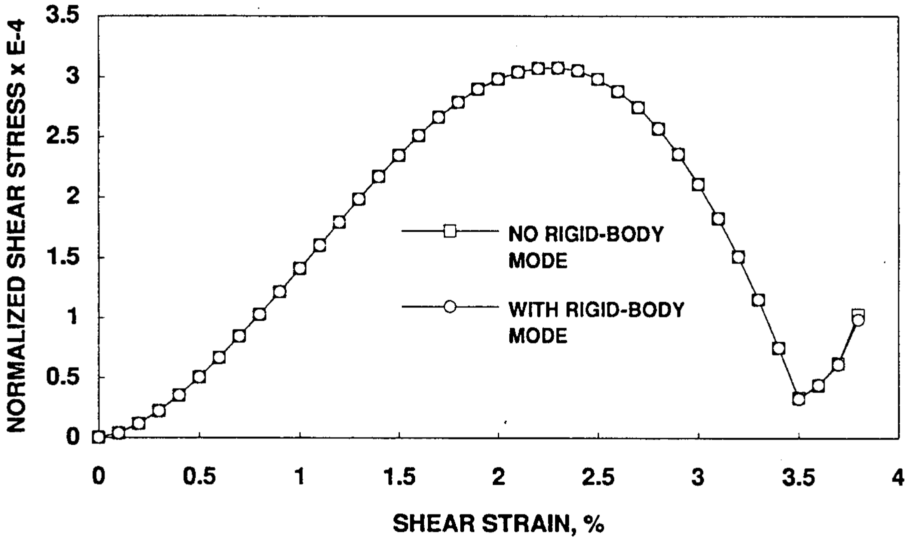

Figure 15. Normalized overall shear stress $\bar{\sigma}^*_{12}/k_T$ versus overall shear strain $\bar{\epsilon}_{12}$ for the 58-particle assembly.

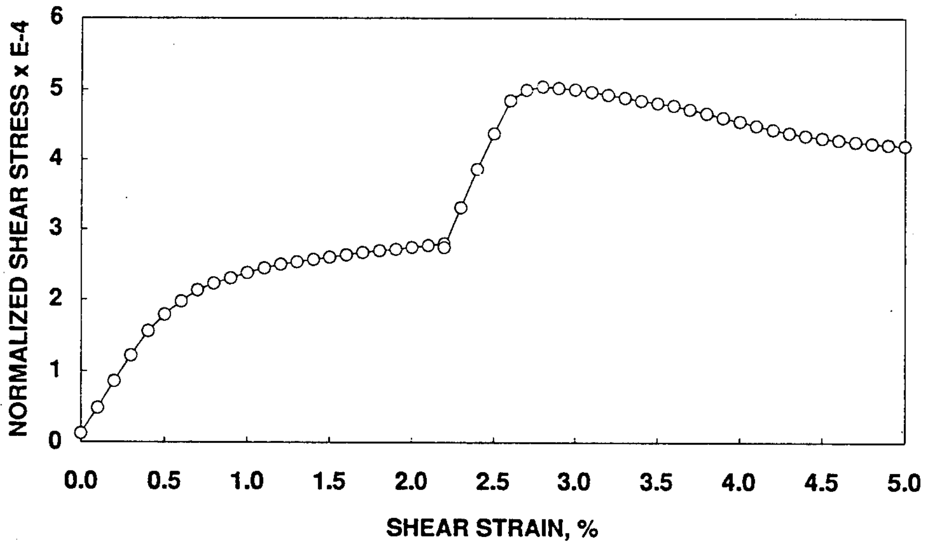

Figure 16. Normalized overall shear stress $\bar{\sigma}_{12}^{*}/k_T$ versus overall shear strain $\bar{\epsilon}_{12}$ for the 58-particle assembly.

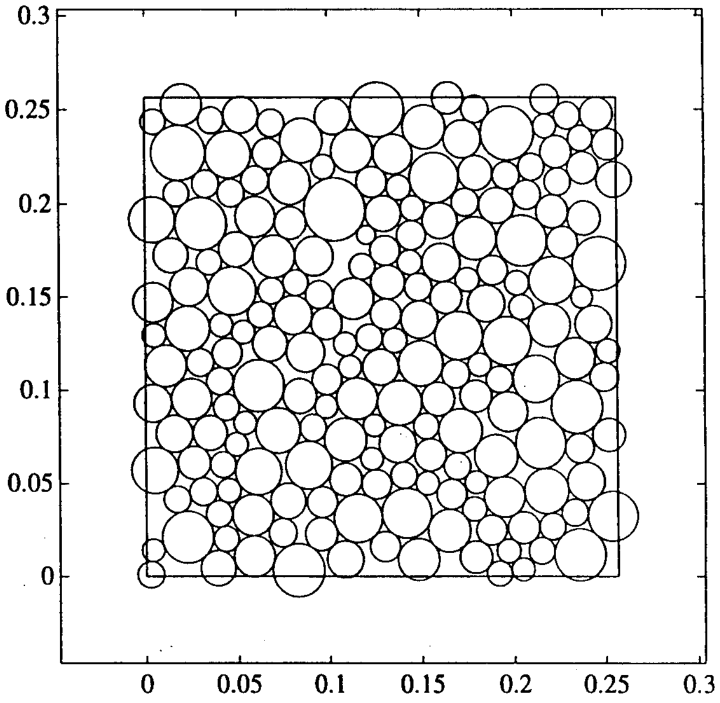
0.3
0.25
0.2
0.15
0.1
0.05
0
0
0.05
0.1
0.15
0.2
0.25
0.3

Figure 17. Initial configuration for the 196-particle assembly. Coefficient of uniformity $C_u = 1.71$; coefficient of curvature $C_c = 0.90$; mean particle radius = 0.0092 units.

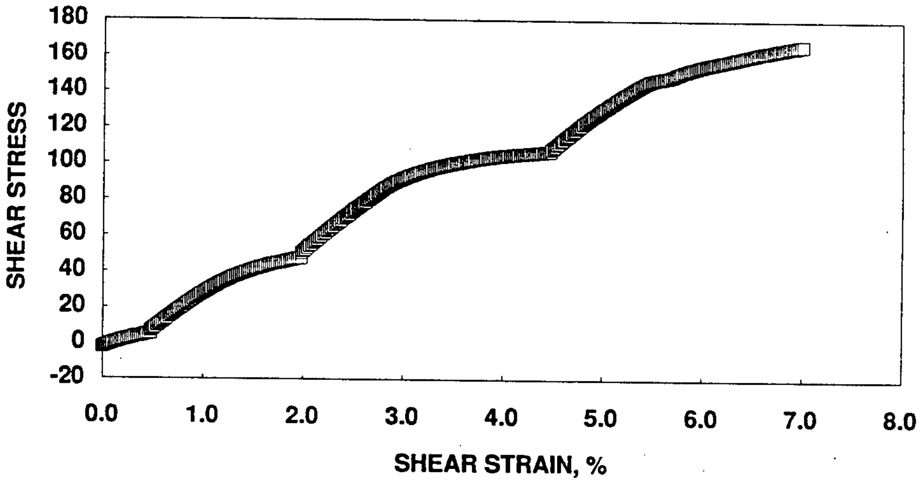

Figure 18. Overall shear stress $\bar{\sigma}^*_{12}$ versus overall shear strain $\bar{\epsilon}_{12}$ for the 196-particle assembly subjected to alternating isotropic compression and simple shear strain history.

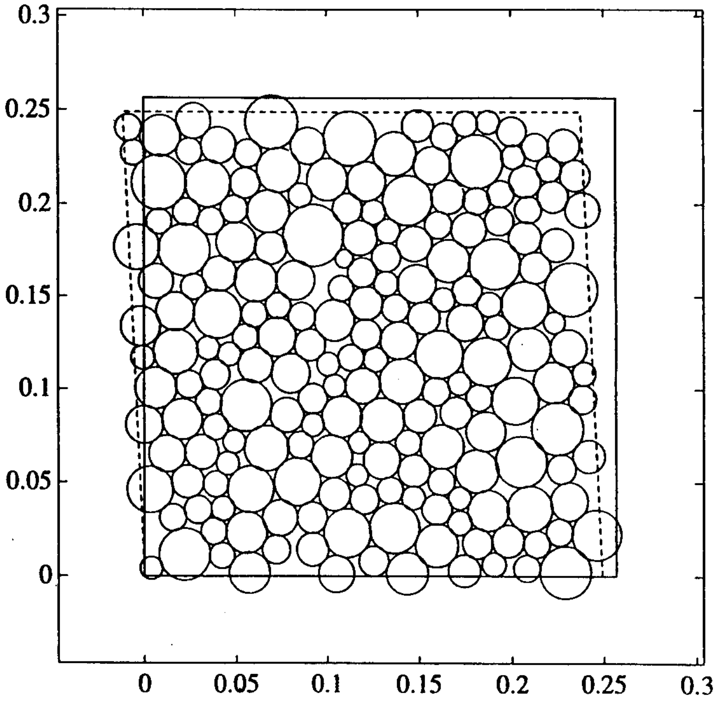
0.3
0.25
0.2
0.15
0.1
0.05
0
0
0.05
0.1
0.15
0.2
0.25
0.3

Figure 19. Deformed configuration for the 196-particle assembly; mean particle radius = 0.0092 units.

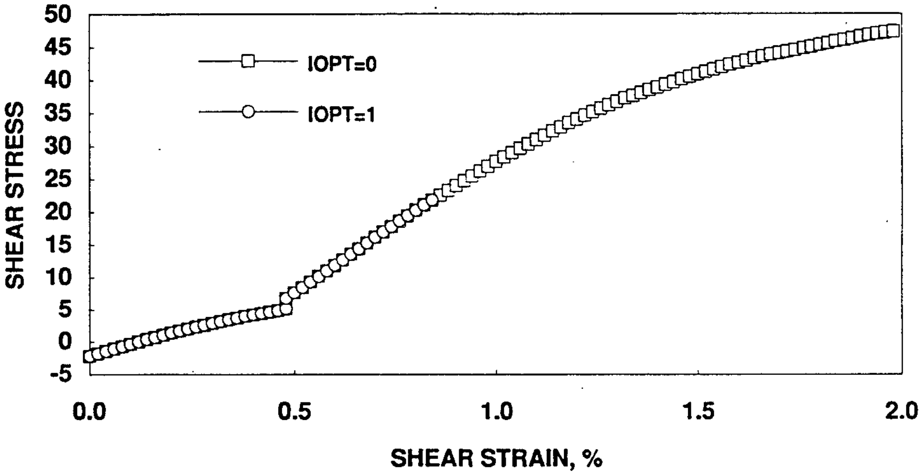

Figure 20. Overall shear stress $\bar{\sigma}_{12}^{*}$ versus overall shear strain $\bar{\epsilon}_{12}$ for the 196-particle assembly; IOPT=0, contact is assumed formed at $t = t_n$ between two previously non-overlapping particles; IOPT=1, contact is formed at $t = t_{n+1}$.

Chapter 5

Stress-driven Problem

5.1. Introduction

When a macroscopic point in a granular material experiences an overall stress history, it responds according with some uniform macroscopic deformation. This overall motion must be compatible with the movement of the individual particles contained in the control volume. Thus, when given a stress history, the macroscopic uniform deformation of the particle assembly and the discrete microscopic particle motions constitute the principal unknowns. In the language of computational plasticity, one has a stress-driven, or inverse, problem. A stress-driven problem requires two levels of analysis:

i. *micromechanical level* to calculate the contact forces and, eventually, the overall stresses $\bar{\boldsymbol{\sigma}}$ resulting from an imposed overall deformation gradient $\boldsymbol{A}$,

ii. *macromechanical level* to iteratively determine the uniform control volume motion $\boldsymbol{A}^*$ which exactly produces the prescribed overall stresses $\bar{\boldsymbol{\sigma}}^*$.

The strain-driven algorithm presented in Chapter 4 forms the basis of the micromechanical level by determining the particle contact forces for a given overall deformation of the control volume.

It is emphasized that while the formulation in this chapter admits finite motions of the individual granules, the overall material response is based on infinitesimal theory, i.e., $\boldsymbol{A}$ is assumed to be 'small.' Consequently, the present formulation captures only the material overall response. Finite rotation and/or large deformation of the control volume, which could be important in many boundary-value problems, may be readily incorporated in the macroscopic formulation in a future extension of the model.

This chapter presents alternative algorithms for solving the inverse problem based on Newton and Newton-type methods. First, a description of the algorithm for the solution of the stress-driven problem is presented. The remainder of the chapter considers the issues surrounding the consistent linearization of the overall elasto-plastic constitutive relations. In order to exactly derive the algorithmic tangent operator, an additive decomposition of the particle motions is presented. The implications of this decomposition on particle contact slip, contact forces, and the overall stress are then investigated to render the derivation of the exact algorithmic tangent. This chapter then devotes special attention to the implementational hurdles surrounding the exact tangent operator. Finally, to circumvent these difficulties, a secant approximation is described that retains the essential properties of the exact description.

5.2. Algorithm for problems with imposed overall stresses

Let $\bar{\boldsymbol{\sigma}}^*_{n+1}$ be the imposed overall stresses. For equilibrium, one can write the macroscopic stress equation at time station t_{n+1} as

$$\bar{\boldsymbol{\sigma}}(\boldsymbol{A}^*_{n+1}, \boldsymbol{\psi}_{n+1}) - \bar{\boldsymbol{\sigma}}^*_{n+1} = \boldsymbol{0}\,, \tag{5.1}$$

where $\boldsymbol{A}^*_{n+1}$ denotes the overall displacement gradients compatible with the imposed overall stresses $\bar{\boldsymbol{\sigma}}^*_{n+1}$, and $\boldsymbol{\psi}_{n+1}$ represents a set of strictly micromechanical variables. This equilibrium equation represents an extension of the functional relation (3.29) to include the effects of the assembly's microstructure. The physical meaning of equation (5.1) is that the applied loads equilibrate the internal stress which depends in a very complex manner upon the uniform control volume motion and upon micromechanical variables such as the particle coordination numbers, the formation and rupture of particle contacts, and the stability of the control volume's microstructure.

In plane strain applications, the applied stress represents a vector with four independent components. However, since the balance of angular momentum (3.4) requires that the calculated overall stress be symmetric, equation (5.1) yields three coupled nonlinear equations for each component of the applied stress:

$$\bar{\boldsymbol{\sigma}}^*_{n+1} = \{\bar{\sigma}^*_{11},\, \bar{\sigma}^*_{22},\, \bar{\sigma}^*_{12}\}^t_{n+1}\,. \tag{5.2}$$

The unknown vector of the uniform motion then becomes

$$\boldsymbol{A}_{n+1} = \{A_{11},\, A_{22},\, A_{12}\}^t_{n+1}\,. \tag{5.3}$$

The applied stress vector in (5.2) will be formed by instantaneously imposing the incremental stress $\bar{\boldsymbol{\sigma}}^*_{n+1} - \bar{\boldsymbol{\sigma}}^*_n$ at discrete time steps $\Delta t = t_{n+1} - t_n$. Likewise, the internal stress $\bar{\boldsymbol{\sigma}}$ instantaneously varies following the application of the incremental stresses.

We now denote $(\boldsymbol{G}_{EXT})_{n+1}$ as the vector of applied overall stresses given by

$$(\boldsymbol{G}_{EXT})_{n+1} = \bar{\boldsymbol{\sigma}}^*_{n+1}\,, \tag{5.4}$$

and $\boldsymbol{G}_{INT}$ as the vector of internal stresses given by

$$\boldsymbol{G}_{INT} = \bar{\boldsymbol{\sigma}}(\boldsymbol{A}_{n+1}, \psi_{n+1})\,. \tag{5.5}$$

The condition of macroscopic stress equilibrium can then be rewritten in residual form in terms of macroscopic quantities as

$$\boldsymbol{R} = \boldsymbol{G}_{INT}(\boldsymbol{A}^*_{n+1}) - (\boldsymbol{G}_{EXT})_{n+1} = \boldsymbol{0} \tag{5.6}$$

where $\boldsymbol{A}^*_{n+1}$ are the roots of the nonlinear system of equations (5.1). Linearizing the residual equation gives

$$-\boldsymbol{G}'_{INT}(\boldsymbol{A}^k_{n+1})\Delta \boldsymbol{A}^k = (\boldsymbol{G}_{EXT})_{n+1} - \boldsymbol{G}_{INT}(\boldsymbol{A}^k_{n+1}) \tag{5.7}$$

where

$$G'_{INT}(\boldsymbol{A}^k_{n+1}) = \boldsymbol{C} = \frac{\partial \bar{\boldsymbol{\sigma}}(\boldsymbol{A}^k_{n+1})}{\partial \boldsymbol{A}^k_{n+1}} \tag{5.8}$$

is the tangent matrix, and $\Delta \boldsymbol{A}^k$ represents the kth search direction for the solution vector $\boldsymbol{A}^k_{n+1}$. Note that the matrix $\boldsymbol{C}$ in (5.8) represents the material stress-strain matrix when the elements of $\boldsymbol{A}^k_{n+1}$ are small.

Applying Newton's method, the next estimate of $\boldsymbol{A}^*_{n+1}$ can be computed from

$$\boldsymbol{A}^{k+1}_{n+1} = \boldsymbol{A}^k_{n+1} - \left[G'_{INT}(\boldsymbol{A}^k_{n+1})\right]^{-1} \boldsymbol{R}^k. \tag{5.9}$$

The method is said to have converged when

$$\|\boldsymbol{R}^k\| / \|\boldsymbol{R}^0\| < \mathrm{RTOL}\,, \tag{5.10}$$

where RTOL is a prescribed error tolerance.

Box 3 summarizes the necessary steps for solving a stress-driven problem. In view of the two levels of analysis required to solve this type of problem, two nested Newton iteration loops are necessary. Inclusion of the call to the micromechanical level clarifies the central role played by the strain-driven algorithm. Note in Box 3 that the inverse algorithm is only at best as stable as the inner Newton loop for the strain-driven algorithm.

5.3. Particle displacement decomposition

Consider the exact evaluation of the algorithmic tangent (5.8). Central to this computation lies the complex micromechanical-macromechanical connection between the independent particle motions and the overall control volume deformation. The micromechanical level subjects the assembly of particles to a prescribed macroscopic uniform motion and then allows the particles to move in a microscopic sense to achieve equilibrium [26–28]. This section derives a decomposition of the particle displacements to formalize this micromechanical-macromechanical connection essential for exactly evaluating the algorithmic tangent.

Box 3. Stress-driven algorithm.

```
Macromechanical level

1. Given $\bar{\boldsymbol{\sigma}}^*_{n+1}$, $\bar{\boldsymbol{\sigma}}^*_n$, and $k = 0$.
2. Compute: $\boldsymbol{G}'_{INT}(\boldsymbol{A}^k_{n+1})$.
3. $\boldsymbol{A}^{k+1}_{n+1} = \boldsymbol{A}^k_{n+1} - \left[\boldsymbol{G}'_{INT}(\boldsymbol{A}^k_{n+1})\right]^{-1} \boldsymbol{R}^k$.
4. Call Micromechanical level in Box 2 with $\boldsymbol{A}^{k+1}_{n+1}$, $\boldsymbol{A}_n$, and $i = 0$.
5. $\bar{\boldsymbol{\sigma}} = \frac{1}{2}\sum_{\alpha=1}^{N}(\boldsymbol{f}^\alpha \otimes \boldsymbol{l}^\alpha + \boldsymbol{l}^\alpha \otimes \boldsymbol{f}^\alpha)$.
6. $\boldsymbol{R}^{k+1} = \bar{\boldsymbol{\sigma}}(\boldsymbol{A}^k_{n+1}) - \boldsymbol{\sigma}^*_{n+1}$.
7. IF $\|\boldsymbol{R}^{k+1}\|/\|\boldsymbol{R}^0\| < \mathrm{RTOL}$, RETURN.
8. $k \leftarrow k + 1$ and GO TO 2. $\square$
```

To this end, the relationship between the particle displacements and the overall displacement gradient must first be constructed.

Recall that the dependence of the contact forces $\boldsymbol{f}^e$ on the imposed displacement gradient $\boldsymbol{A}$ followed directly from the initial imposition of the uniform motion on the particle centroids. This motion causes contacting particles to either slip, overlap, or separate creating unbalanced contact forces and acts as the initial estimate for the Newton solution given in Box 2. The perturbed momentum balance equations given in (4.13) as

$$\boldsymbol{r} = \boldsymbol{F}_{INT}(\boldsymbol{A} \cdot \boldsymbol{X}^A_n) \neq \boldsymbol{0} \tag{5.11}$$

create the residual in the force vector which must be dissipated by the Newton iteration. Thus, the initial particle displacements (i.e., the first guess of the new particle equilibrium positions) depend solely on the uniform motion $\boldsymbol{A}$.

The continued dependence of $\boldsymbol{f}^e$ on the displacement gradient $\boldsymbol{A}$ follows from the dissipation of $\boldsymbol{r}$ in (5.11) through the Newton iteration as the particles displace to the new equilibrium configuration. The sides of the unit cell remain fixed according to the uniform motion of $\boldsymbol{A}$. In other words, after the initial imposition of $\boldsymbol{A}$, the particle displacements to equilibrium continue to depend on $\boldsymbol{A}$, but they also depend on the local effects of the material's microstructure described by the variables $\boldsymbol{\psi}$. Thus, from a typical particle's perspective, the dependency on the displacement gradient $\boldsymbol{A}$ and the micromechanical variables $\boldsymbol{\psi}$ can be formalized as

$$\boldsymbol{d}_{n+1} = \boldsymbol{d}_{n+1}(\boldsymbol{A}_{n+1}, \boldsymbol{\psi}_{n+1})\,. \tag{5.12}$$

This displacement relationship can be understood from a different perspective. Consider a densely packed control volume experiencing a small overall shearing motion that slightly perturbs the momentum balance equations (5.11). The constituent particles need only displace and rotate a small amount depending on the current set of micromechanical variables $\boldsymbol{\psi}$ to reach equilibrium. Therefore, in the limit as the magnitude of the overall motions approaches a small value, say ϵ, the uniform particle motions may accurately describe the total particle displacements,

$$\lim_{\|A_{n+1}\| \to \epsilon} \boldsymbol{d}_{n+1} = \boldsymbol{d}_{n+1}(\boldsymbol{A}_{n+1})\,. \tag{5.13}$$

Since the macroscopic motion is not restricted to be vanishingly small, the particle displacements will also depend on the microscopic variables $\boldsymbol{\psi}$, and therefore

$$\boldsymbol{d}_{n+1} = \boldsymbol{d}_{n+1}(\boldsymbol{A}_{n+1}, \boldsymbol{\psi}_{n+1})\,. \tag{5.14}$$

This displacement relationship can be made explicit by additively decomposing the particles' displacement degrees of freedom into a displacement $\tilde{\boldsymbol{d}}$ due to the uniform control volume motion and a microscopic displacement $\hat{\boldsymbol{d}}$ describing the particles' equilibrium motion

$$\boldsymbol{d}^A(\boldsymbol{A}_{n+1}, \boldsymbol{\psi}_{n+1}) = \tilde{\boldsymbol{d}}^A(\boldsymbol{A}_{n+1}) + \hat{\boldsymbol{d}}^A(\boldsymbol{A}_{n+1}, \boldsymbol{\psi}_{n+1})\,, \tag{5.15}$$

where particle A's point of view has been taken. Note that the microscopic displacement $\hat{\boldsymbol{d}}$ also depends on the uniform motion.

In two-dimensions, the associated displacements for particles A and B connected by contact element 'e' can be written as

$$\boldsymbol{d}^e = \tilde{\boldsymbol{d}}^e + \hat{\boldsymbol{d}}^e\,, \tag{5.16}$$

where

$$\boldsymbol{d}^e_{(6\times 1)} = \left\{ \begin{array}{c} \boldsymbol{d}^A \\ \theta^A_{n+1} \\ \boldsymbol{d}^B \\ \theta^B_{n+1} \end{array} \right\}, \quad \tilde{\boldsymbol{d}}^e_{(6\times 1)} = \left\{ \begin{array}{c} \tilde{\boldsymbol{d}}^A \\ 0 \\ \tilde{\boldsymbol{d}}^B \\ 0 \end{array} \right\}, \quad \hat{\boldsymbol{d}}^e_{(6\times 1)} = \left\{ \begin{array}{c} \hat{\boldsymbol{d}}^A \\ \theta^A_{n+1} \\ \hat{\boldsymbol{d}}^B \\ \theta^B_{n+1} \end{array} \right\}. \tag{5.17}$$

Note that according to this decomposition the uniform control volume motion results in only particle translation. The individual particle rotations result from the locally discrete particle motion to reach equilibrium.

5.4. Displacement decomposition and particle kinematics/contact forces

This section considers the implications of the particle displacement decomposition for the particle contact slip and the contact forces. It pays special attention to the impact of the decomposition on the path of the problem at a typical particle contact.

Consider application of the displacement decomposition (5.15) to the definition of the contact unit normal. As seen in Chapter 2, the definition of the contact normal is central to the kinematic description of particle contact slip. Again taking particle A's point of view, let the contact normal in two dimensions be

$$\boldsymbol{n}^A_{n+1} \equiv \boldsymbol{n}_{n+1} = \boldsymbol{l}_{n+1}/\|\boldsymbol{l}_{n+1}\| = \{n_1, n_2\}^t, \tag{5.18}$$

where

$$\begin{aligned} \boldsymbol{l}_{n+1} &= \hat{\boldsymbol{X}}^B + \boldsymbol{d}^B_{n+1} - (\hat{\boldsymbol{X}}^A + \boldsymbol{d}^A_{n+1}) && (5.19) \\ &= \hat{\boldsymbol{X}}^B + \tilde{\boldsymbol{d}}^B_{n+1} + \hat{\boldsymbol{d}}^B_{n+1} - (\hat{\boldsymbol{X}}^A + \tilde{\boldsymbol{d}}^A_{n+1} + \hat{\boldsymbol{d}}^A_{n+1}). && (5.20) \end{aligned}$$

Similarly, the contact normal after the application of the uniform macroscopic motion is given by

$$\boldsymbol{n}^A_{\tilde{n}} \equiv \boldsymbol{n}_{\tilde{n}} = \boldsymbol{l}_{\tilde{n}}/\|\boldsymbol{l}_{\tilde{n}}\|, \tag{5.21}$$

where

$$\boldsymbol{l}_{\tilde{n}} = \hat{\boldsymbol{X}}^B + \tilde{\boldsymbol{d}}^B_{n+1} - (\hat{\boldsymbol{X}}^A + \tilde{\boldsymbol{d}}^A_{n+1}) \,. \tag{5.22}$$

The normal indentation δ can be written as

$$\delta_{n+1} = r^A + r^B - \|\boldsymbol{l}_{n+1}\| \,, \tag{5.23}$$

where r^A and r^B denote the radius of particle A and B respectively.

The definitions of $\boldsymbol{n}^A_{n+1}$ and $\boldsymbol{n}^A_{\tilde{n}}$ may be used to segregate the total slip increment $\Delta\gamma$ into slip due to the uniform control volume motion $\Delta\gamma_{\tilde{n}}$ and slip due to the particle equilibrium motion $\Delta\gamma_{\hat{n}}$

$$\Delta\gamma = \Delta\gamma_{\tilde{n}} + \Delta\gamma_{\hat{n}}. \tag{5.24}$$

Recall that the total slip increment is written as

$$\Delta\gamma = \Delta\theta^{AC} r^A + \Delta\theta^{BC} r^B \,, \tag{5.25}$$

where

$$\Delta\theta^{AC} = \Delta\theta^C - (\theta^A_{n+1} - \theta^A_n) \,, \tag{5.26}$$

$$\Delta\theta^{BC} = \Delta\theta^C - (\theta^B_{n+1} - \theta^B_n) \,, \tag{5.27}$$

and

$$\Delta\theta^C = \sin^{-1}(\boldsymbol{e}_3 \cdot \boldsymbol{n}^A_n \times \boldsymbol{n}^A_{n+1}) \,. \tag{5.28}$$

Incorporation of $\boldsymbol{n}^A_{n+1}$ and $\boldsymbol{n}^A_{\tilde{n}}$ into these equations leads naturally to the following definitions:

$$\begin{aligned}
\Delta\gamma_{\tilde{n}} &= \Delta\theta^{AC}_{\tilde{n}} r^A + \Delta\theta^{BC}_{\tilde{n}} r^B \,, & \Delta\gamma_{\hat{n}} &= \Delta\theta^{AC}_{\hat{n}} r^A + \Delta\theta^{BC}_{\hat{n}} r^B \,; \\
\Delta\theta^{AC}_{\tilde{n}} &= \Delta\theta^C_{\tilde{n}} \,, & \Delta\theta^{AC}_{\hat{n}} &= \Delta\theta^C_{\hat{n}} - (\theta^A_{n+1} - \theta^A_n) \,; \\
\Delta\theta^{BC}_{\tilde{n}} &= \Delta\theta^C_{\tilde{n}} \,, & \Delta\theta^{BC}_{\hat{n}} &= \Delta\theta^C_{\hat{n}} - (\theta^B_{n+1} - \theta^B_n) \,; \\
\Delta\theta^C_{\tilde{n}} &= \sin^{-1}(\boldsymbol{e}_3 \cdot \boldsymbol{n}_n \times \boldsymbol{n}_{\tilde{n}}) \,, & \Delta\theta^C_{\hat{n}} &= \sin^{-1}(\boldsymbol{e}_3 \cdot \boldsymbol{n}_{\tilde{n}} \times \boldsymbol{n}_{n+1}).
\end{aligned} \tag{5.29}$$

It is important to note that equations (5.24) and (5.29) only redefine the definition of the total slip $\Delta\gamma$ in terms of the displacement decomposition. The path of the problem remains unaltered in the sense that the solution moves from time station t_n to t_{n+1} without updating the path dependent variables at an intermediate station, say, $t_{\tilde{n}}$. For example, the contact plastic slip is defined for the entire increment $\Delta t = t_{n+1} - t_n$ as

$$|\Delta\gamma^p| = \frac{|f_T^{\text{tr}}| - \alpha_n + f_N \tan\phi}{H_\varepsilon k_T + H'}, \tag{5.30}$$

where

$$f_T^{\text{tr}} = (f_T)_n + H_\varepsilon k_T \Delta\gamma. \tag{5.31}$$

The loading/unloading conditions have not been used to compute intermediate values such as $\Delta\gamma_{\tilde{n}}^p$ and $\Delta\gamma_{\hat{n}}^p$. Using the displacement decomposition as the basis for intermediate nonconverged states appears questionable for a problem which, physically, is path-dependent [37]. If unloading of a contact element occurs during the Newton iteration process, each new iteration should start from the converged configuration $\boldsymbol{d}_n$ and not from an intermediate configuration like, say, $\boldsymbol{d}_{\tilde{n}}$.

Likewise, it is important to note that loading/unloading conditions are not employed to derive an intermediate force resulting from the uniform motion, say $(f_T)_{\tilde{n}}$, and a remainder force, say $(f_T)_{\hat{n}}$. The displacement decomposition does not result in a decomposition in the contact forces such as

$$(f_T)_{n+1} \neq (f_T)_{\tilde{n}}(\tilde{\boldsymbol{d}}) + (f_T)_{\hat{n}}(\tilde{\boldsymbol{d}}, \hat{\boldsymbol{d}}). \tag{5.32}$$

Such an application of the displacement decomposition would erroneously change the path of the problem from

$$t_n \xrightarrow{f_{n+1}} t_{n+1} \tag{5.33}$$

to a new path described by

$$t_n \xrightarrow{f_{\tilde{n}}} t_{\tilde{n}} \xrightarrow{f_{\hat{n}}} t_{n+1}, \tag{5.34}$$

where " $\xrightarrow{f_{n+1}}$ " means that the force f_{n+1} is updated from configuration at t_n to t_{n+1}.

5.5. Displacement decomposition and the macroscopic stresses

Now consider the implications of the displacement decomposition on the calculated stress. In Section 3.4, the initial description of the internal stress was simply

$$\bar{\boldsymbol{\sigma}}_{n+1} = \bar{\boldsymbol{\sigma}}_{n+1}(\boldsymbol{A}). \tag{5.35}$$

With the inclusion of the micromechanical variables $\boldsymbol{\psi}$, this expression then became

$$\bar{\boldsymbol{\sigma}}_{n+1} = \bar{\boldsymbol{\sigma}}_{n+1}(\boldsymbol{A}, \boldsymbol{\psi}). \tag{5.36}$$

A thorough examination of the overall stress from a different perspective leads to a more precise expression for the dependency of the stress. The expression for the stress (3.12) shows a dependency on the particle contact forces and the location of the particle centroid,

$$\bar{\boldsymbol{\sigma}} = \bar{\boldsymbol{\sigma}}(\mathcal{F}(\boldsymbol{d}), \boldsymbol{d}). \tag{5.37}$$

With the displacement decomposition, the contact forces $\mathcal{F}$ may be written as

$$\mathcal{F} = \mathcal{F}(\tilde{\boldsymbol{d}}, \hat{\boldsymbol{d}}). \tag{5.38}$$

Thus, the calculated stress can be then viewed as a fundamental function of the uniform and equilibrium displacements

$$\bar{\boldsymbol{\sigma}}_{n+1} = \bar{\boldsymbol{\sigma}}_{n+1}(\tilde{\boldsymbol{d}}, \hat{\boldsymbol{d}}). \tag{5.39}$$

This functional relationship can be reconciled with equation (5.36) by substituting the displacement decomposition to yield

$$\bar{\boldsymbol{\sigma}}_{n+1} = \bar{\boldsymbol{\sigma}}_{n+1}(\tilde{\boldsymbol{d}}(\boldsymbol{A}), \hat{\boldsymbol{d}}(\boldsymbol{A}, \boldsymbol{\psi})). \tag{5.40}$$

Note that equation (5.38) can be easily demonstrated by considering the expression for the tangential contact force

$$(f_T)_{n+1} = (f_T)_n + H_\epsilon k_T \left(\Delta\gamma - \Delta\gamma^p\right). \tag{5.41}$$

Substituting (5.24), (5.30), and (5.31) yields

$$\begin{aligned}(f_T)_{n+1} = {} & \frac{H_\epsilon k_T}{H_\epsilon k_T + H'} \left[H'(\Delta\gamma_{\tilde{n}} - \Delta\gamma_{\hat{n}}) - \mathrm{sign}(\cdot)\alpha_n + \mathrm{sign}(\cdot) f_N \tan\phi\right] \\ & + \frac{H'}{H_\epsilon k_T + H'}\,(f_T)_n\end{aligned} \tag{5.42}$$

where $(\cdot) = (f_T)_n + H_\epsilon k_T \Delta\gamma$. From (5.29), it follows that $\Delta\gamma_{\tilde{n}} = \Delta\gamma_{\tilde{n}}(\tilde{\boldsymbol{d}})$ and $\Delta\gamma_{\hat{n}} = \Delta\gamma_{\hat{n}}(\tilde{\boldsymbol{d}}, \hat{\boldsymbol{d}})$, and therefore

$$(f_T)_{n+1} = f_T(\tilde{\boldsymbol{d}}, \hat{\boldsymbol{d}}) \tag{5.43}$$

which leads directly to equation (5.38).

5.6. Exact algorithmic tangent operator and concentration tensor

Now, with the expression (5.39) for the stress, an exact expression for the tangent operator can be derived. Employing the chain rule on the calculated stress $\bar{\boldsymbol{\sigma}}$ gives (dropping the subscripts $n+1$ and superscripts k)

$$\boldsymbol{G}'_{INT}(\boldsymbol{A}) = \frac{\partial\bar{\boldsymbol{\sigma}}(\tilde{\boldsymbol{d}}, \hat{\boldsymbol{d}})}{\partial\boldsymbol{A}} = \frac{\partial\bar{\boldsymbol{\sigma}}}{\partial\tilde{\boldsymbol{d}}}\frac{\partial\tilde{\boldsymbol{d}}}{\partial\boldsymbol{A}} + \frac{\partial\bar{\boldsymbol{\sigma}}}{\partial\hat{\boldsymbol{d}}}\frac{\partial\hat{\boldsymbol{d}}}{\partial\boldsymbol{A}}. \tag{5.44}$$

The derivatives of the stress $\bar{\boldsymbol{\sigma}}$ can be explicitly derived from (3.12) as

$$\frac{\partial\bar{\sigma}_{ij}}{\partial\tilde{d}_k} = \tfrac{1}{2}\sum_{\alpha=1}^{N}\left(\frac{\partial f_i^\alpha}{\partial\tilde{d}_k} l_j^\alpha + f_i^\alpha\frac{\partial l_j^\alpha}{\partial\tilde{d}_k} + \frac{\partial f_j^\alpha}{\partial\tilde{d}_k} l_i^\alpha + f_j^\alpha\frac{\partial l_i^\alpha}{\partial\tilde{d}_k}\right) \tag{5.45}$$

$$\frac{\partial\bar{\sigma}_{ij}}{\partial\hat{d}_k} = \tfrac{1}{2}\sum_{\alpha=1}^{N}\left(\frac{\partial f_i^\alpha}{\partial\hat{d}_k} l_j^\alpha + f_i^\alpha\frac{\partial l_j^\alpha}{\partial\hat{d}_k} + \frac{\partial f_j^\alpha}{\partial\hat{d}_k} l_i^\alpha + f_j^\alpha\frac{\partial l_i^\alpha}{\partial\hat{d}_k}\right) \tag{5.46}$$

Appendix D contains a complete discussion of these force derivatives.

The displacement derivatives in equation (5.44) can be summarized in terms of the displacement decomposition as

$$\frac{\partial\boldsymbol{d}}{\partial\boldsymbol{A}} = \frac{\partial\tilde{\boldsymbol{d}}}{\partial\boldsymbol{A}} + \frac{\partial\hat{\boldsymbol{d}}}{\partial\boldsymbol{A}}. \tag{5.47}$$

Taking the point of view of particle A, the first derivative on the right-hand side can be found from

$$\tilde{\boldsymbol{d}}^A = \boldsymbol{A} \cdot \boldsymbol{X}_n^A \,. \tag{5.48}$$

The derivative can be written as

$$\frac{\partial \tilde{\boldsymbol{d}}^A}{\partial \boldsymbol{A}} = \begin{bmatrix} X_1^A & 0 & X_2^A \\ 0 & X_2^A & X_1^A \\ 0 & 0 & 0 \end{bmatrix} . \tag{5.49}$$

Equation (5.47) represents the change in the total particle motion with respect to the change in the overall motion of the control volume — the so-called 'concentration tensor' [23–28,38].

The exact evaluation of the concentration tensor requires explicitly extending the displacement decomposition into the micromechanical level residual $\boldsymbol{r}$ which can be written as

$$\boldsymbol{r} = \boldsymbol{F}_{INT}(\boldsymbol{d}_{n+1}) = \boldsymbol{0} \tag{5.50}$$

$$= \boldsymbol{F}_{INT}(\tilde{\boldsymbol{d}},\, \hat{\boldsymbol{d}}) \tag{5.51}$$

$$= \bigcup_{e=1}^{n_{el}} \boldsymbol{f}^e(\tilde{\boldsymbol{d}},\, \hat{\boldsymbol{d}}). \tag{5.52}$$

The first variation of this expression yields

$$\frac{\partial \boldsymbol{r}}{\partial \tilde{\boldsymbol{d}}}\, \delta \tilde{\boldsymbol{d}} + \frac{\partial \boldsymbol{r}}{\partial \hat{\boldsymbol{d}}}\, \delta \hat{\boldsymbol{d}} = \boldsymbol{0}\,. \tag{5.53}$$

where δ denotes a small variation. Since the displacements $\tilde{\boldsymbol{d}}$ and $\hat{\boldsymbol{d}}$ depend on the macroscopic motion $\boldsymbol{A}$, use of the chain rule on (5.53) gives

$$\left[\frac{\partial \boldsymbol{r}}{\partial \tilde{\boldsymbol{d}}} \frac{\partial \tilde{\boldsymbol{d}}}{\partial \boldsymbol{A}} + \frac{\partial \boldsymbol{r}}{\partial \hat{\boldsymbol{d}}} \frac{\partial \hat{\boldsymbol{d}}}{\partial \boldsymbol{A}} \right] \delta \boldsymbol{A} = \boldsymbol{0}. \tag{5.54}$$

It follows that for an arbitrary $\delta \boldsymbol{A}$

$$\frac{\partial \boldsymbol{r}}{\partial \tilde{\boldsymbol{d}}} \frac{\partial \tilde{\boldsymbol{d}}}{\partial \boldsymbol{A}} + \frac{\partial \boldsymbol{r}}{\partial \hat{\boldsymbol{d}}} \frac{\partial \hat{\boldsymbol{d}}}{\partial \boldsymbol{A}} = \boldsymbol{0}. \tag{5.55}$$

Substituting equation (5.52) into (5.55) yields an exact expression for the concentration tensor as

$$\frac{\partial \boldsymbol{d}}{\partial \boldsymbol{A}} = -\hat{\boldsymbol{K}}^{-1}\tilde{\boldsymbol{K}}\frac{\partial \tilde{\boldsymbol{d}}}{\partial \boldsymbol{A}}, \tag{5.56}$$

where

$$\hat{\boldsymbol{K}} = \bigcup_{e=1}^{n_{el}} \hat{\boldsymbol{k}}^e = \bigcup_{e=1}^{n_{el}} \frac{\partial \boldsymbol{f}^e}{\partial \hat{\boldsymbol{d}}^e}, \tag{5.57}$$

$$\hat{\boldsymbol{K}} + \tilde{\boldsymbol{K}} = \bigcup_{e=1}^{n_{el}} \left(\hat{\boldsymbol{k}}^e + \tilde{\boldsymbol{k}}^e\right) = \bigcup_{e=1}^{n_{el}} \frac{\partial \boldsymbol{f}^e}{\partial \tilde{\boldsymbol{d}}^e}. \tag{5.58}$$

The element contributions to the matrices $\hat{\boldsymbol{K}}$ and $\tilde{\boldsymbol{K}}$ can be found in Appendix D. The definition of the algorithmic tangent matrix which can now be written as

$$G'_{INT}(\boldsymbol{A}) = \left[\frac{\partial \bar{\boldsymbol{\sigma}}}{\partial \tilde{\boldsymbol{d}}} - \frac{\partial \bar{\boldsymbol{\sigma}}}{\partial \hat{\boldsymbol{d}}}\left(1 + \hat{\boldsymbol{K}}^{-1}\tilde{\boldsymbol{K}}\right)\right]\frac{\partial \tilde{\boldsymbol{d}}}{\partial \boldsymbol{A}}. \tag{5.59}$$

As seen from Box 3, the algorithmic tangent will be evaluated after the micromechanical level has reached convergence for the given macroscopic motion.

The numerical simulations of Section 4.4 showed that when a control volume with an initially collapsible structure experiences a shearing deformation beyond its ability to compact, particles separated into isolated clusters. Numerically, this phenomenon manifested itself as zeros on the diagonal of the factorized microscopic tangent operator. These zeros are not operated upon during the back substitution process. The stress-driven problem does not preclude such a phenomenon. In fact, such a 'strain softening' effect could have disastrous implications for the exact evaluation of the tangent and in particular the evaluation of $\hat{\boldsymbol{K}}^{-1}$. If $\hat{\boldsymbol{K}}$ becomes singular, the zeros on the diagonal cannot be ignored and will make the calculation of the exact algorithmic tangent intractable.

In addition, the complexity of the exact algorithmic tangent should be noted. Equation (5.59) requires the considerable effort to evaluate the derivatives contained in $\hat{\boldsymbol{K}}$ and $\tilde{\boldsymbol{K}}$ and also the explicit computation of $\hat{\boldsymbol{K}}^{-1}$. The matrices $\hat{\boldsymbol{k}}^e$ and $\tilde{\boldsymbol{k}}^e$ represent contact element contributions and therefore must be computed for every particle contact in the control volume. Therefore, the intensive computational and assembly effort expended in the exact evaluation of $\hat{\boldsymbol{K}}$, $\hat{\boldsymbol{K}}^{-1}$, and $\tilde{\boldsymbol{K}}$ also represents a significant difficulty engendered with the implementation of the exact algorithmic tangent operator.

5.7. Discretized Newton method

Although Newton's method is theoretically attractive for the stress-driven problem, it is expensive and difficult (if not impossible) to implement. Each iteration not only requires the calculation of the components of the macroscopic residual but also the components of the algorithmic tangent. As Section 3.5 and Appendix D show, the partial derivatives in the tangent matrix do not have a simple functional form. The most direct approach to circumventing the explicit computation of these derivatives is simply to approximate the algorithmic tangent by difference quotients. In what follows, two such approximations for the general stress-driven problem in three dimensions are considered.

Two commonly used difference approximations to the algorithmic tangent operator take the form

$$\frac{\partial R_i(\boldsymbol{A})}{\partial \mathrm{A}_j} \doteq \frac{1}{h_{ij}} \left[R_i \left(\boldsymbol{A} + h_{ij} \boldsymbol{e}^k \right) - R_i \left(\boldsymbol{A} \right) \right] , \tag{5.60}$$

and

$$\frac{\partial R_i(\boldsymbol{A})}{\partial \mathrm{A}_j} \doteq \frac{1}{h_{ij}} \left[R_i \Big(\boldsymbol{A} + \sum_{k=1}^{j} h_{ik} \boldsymbol{e}^k \Big) - R_i \Big(\boldsymbol{A} + \sum_{k=1}^{j-1} h_{ik} \boldsymbol{e}^k \Big) \right] , \tag{5.61}$$

where h_{ij} denotes discretization parameters, and $\boldsymbol{e}^j$ represents the jth coordinate vector. The residual $\boldsymbol{R}$ and parameter vector $\boldsymbol{h}$ have the mapping $\boldsymbol{R} \subset \Re^6$ and $\boldsymbol{h} \subset \Re^6 \times \Re^6$ respectively.

Let $\boldsymbol{\Phi}(\boldsymbol{A}, \boldsymbol{h})$ denote the difference approximations (5.60) and (5.61) with the property that whenever algorithmic tangent exists, then

$$\lim_{\boldsymbol{h} \to \boldsymbol{0}} \boldsymbol{\Phi}(\boldsymbol{A}, \boldsymbol{h}) = \boldsymbol{G}'_{INT}(\boldsymbol{A}, \boldsymbol{h}) . \tag{5.62}$$

Thus, the next estimate of $\boldsymbol{A}^*_{n+1}$ can be computed from

$$\boldsymbol{A}^{k+1}_{n+1} = \boldsymbol{A}^k_{n+1} - \left[\boldsymbol{\Phi}(\boldsymbol{A}^k_{n+1}, \boldsymbol{h}^k)\right]^{-1} \boldsymbol{R}^k. \tag{5.63}$$

This iteration scheme is the so-called 'discretized-Newton' method and represents a special case of the general secant method. Note that the discretization parameters $\boldsymbol{h}$ vary with each iteration.

Now consider several possible ways of choosing $\boldsymbol{h}$. If $h_{ij} = h_i$ such that

$$\boldsymbol{h}^k = \boldsymbol{A}^{k-1} - \boldsymbol{A}^k\,, \tag{5.64}$$

the difference approximation (5.60) yields

$$\begin{aligned}\frac{\partial \boldsymbol{R}(\boldsymbol{A})}{\partial \boldsymbol{A}^k} = \Bigg[\frac{1}{h^k_1}\left[\boldsymbol{R}\left(\boldsymbol{A}^k + h^k_1 \boldsymbol{e}^1\right) - \boldsymbol{R}\left(\boldsymbol{A}^k\right)\right]\,, \ldots\,, \\ \frac{1}{h^k_6}\left[\boldsymbol{R}\left(\boldsymbol{A}^k + h^k_6 \boldsymbol{e}^6\right) - \boldsymbol{R}\left(\boldsymbol{A}^k\right)\right]\Bigg]\,,\end{aligned} \tag{5.65}$$

and the approximation (5.61) gives

$$\begin{aligned}\frac{\partial \boldsymbol{R}(\boldsymbol{A}^k)}{\partial \boldsymbol{A}^k} = \Bigg[\frac{1}{h^k_1}\left[\boldsymbol{R}\left(\boldsymbol{A}^k + h^k_1 \boldsymbol{e}^1\right) - \boldsymbol{R}\left(\boldsymbol{A}^k\right)\right]\,, \ldots\,, \\ \frac{1}{h^k_6}\left[\boldsymbol{R}\left(\boldsymbol{A}^k + \sum_{j=1}^{6} h^k_j \boldsymbol{e}^j\right) - \boldsymbol{R}\left(\boldsymbol{A}^k + \sum_{j=1}^{5} h^k_j \boldsymbol{e}^j\right)\right]\Bigg].\end{aligned} \tag{5.66}$$

The auxiliary points $\boldsymbol{A}^k + (A^{k-1}_j - A^k_j)\boldsymbol{e}^j$ and $\boldsymbol{A}^k + \sum_{i=1}^{j}(A^{k-1}_i - A^k_i)\boldsymbol{e}^i$ in these difference approximations denote the points in $\Re^6$ used to approximate the tangent $G'_{INT}(\boldsymbol{A}^k_{n+1})$.

The methods defined by (5.65) and (5.66) retain the essential properties of Newton's method, and have satisfactory local convergence theorems [34]. An important property of the method defined by (5.63) is that it exhibits the same quadratic convergence as Newton's method while not requiring any derivatives of the residual function $\boldsymbol{R}$.

Note that for a plane strain formulation, the approximation defined by (5.65) requires three function evaluations of the macroscopic residual $\boldsymbol{R}$. However, since

$\boldsymbol{R}(\boldsymbol{A}^{k-1})$ is available from the previous iteration, the approximation (5.66) requires only two new evaluations of $\boldsymbol{R}$. Thus, with only two evaluations of the macroscopic residual $\boldsymbol{R}$, one can circumvent the intensive calculations for the exact algorithmic tangent.

5.8. Numerical simulations

This section presents the results of two-dimensional plane-strain simulations on granular assemblies composed of either regular or random initial packing of circular disks. It also demonstrates some fundamental properties of our numerical model such as quadratic convergence of the discretized-Newton approximation, the invariance of the model under rigid body rotation of the control volume, and the prediction of the onset of localization, as well as reports the numerical difficulties encountered during the simulation process.

Unless otherwise stated, Table 4 defines the model parameters used in all analyses for the macroscopic level and the microscopic level. The overall stresses have been calculated using a volume equal to the initial cross sectional area A_0 times a unit thickness. The error tolerances RTOL and rtol used in (4.8) and (5.10) respectively ensure that the iteration has sufficiently converged, thus minimizing the propagation of numerical errors. For the examples considered throughout this section, the discretized Newton approximation (5.66) has been employed. The same results can be obtained with the approximation (5.65).

Sixty four-particle closest packing assembly

The initial granular assembly configuration is shown in Figure 21. In this example, the assembly consists of sixty four uniform circular particles of radius $r = 1.0$ units arranged in a closest packed configuration. The same configuration can be obtained by rotating the control volume by 60°. The particle on the lower left-hand corner has been fixed against translation and rotation to arrest the zero energy modes present in the assembly. The two initial auxiliary points $\boldsymbol{A}^0$ and $\boldsymbol{A}^1$ are

Table 4. Model parameters.

Macromechanical level

Error tolerance: RTOL $= 1.0 \times 10^{-7}$.

Micromechanical level

Error tolerance: rtol $= 1.0 \times 10^{-8}$.

Normal spring stiffness: $k_N = 1.0 \times 10^4$.

Tangential spring stiffness: $k_T = 1.0 \times 10^4$.

Particle friction angle: $\phi = 30°$.

Particle contact cohesion: $\alpha_0 = 0$.

Contact hardening parameter: $H' = 100$.

Ramp function parameter: $\epsilon = 0.10$.

---

arbitrarily chosen as $\{-0.02, -0.02, 0.0\}^t$ and $\{-0.0275, -0.0275, -5.5 \times 10^{-6}\}^t$, respectively, to launch the discretized Newton approximation (5.66). The converged algorithmic tangent from the previous time step is employed as the initial estimate of the tangent operator for each new time step. Otherwise, these examples follow the Newton algorithm outlined in Box 3, i.e., update the algorithmic tangent each iteration.

The particle assembly experiences a stress history consisting of one increment of isotropic compression $\Delta\bar{\sigma}^*_{11} = \Delta\bar{\sigma}^*_{22} = -200 * A_0 = -0.9021$, $\Delta\bar{\sigma}^*_{21} = \Delta\bar{\sigma}^*_{12} = 0.0$, followed by 35 increments of shear stress $\Delta\bar{\sigma}^*_{11} = \Delta\bar{\sigma}^*_{22} = 0.0$; $\Delta\bar{\sigma}^*_{21} = \Delta\bar{\sigma}^*_{12} = -10.0 * A_0 = -0.0451$. The plot of the normalized overall shear stress $\bar{\sigma}^*_{12}/k_T$ versus the uniform shear motion A_{12} appears in Figure 22 and shows the stress point reaching a yield plateau. At this plateau, the localization function (3.41) becomes negative at the last time step indicating that the localization criterion is satisfied at an intermediate point between the last two time steps. The deformed configuration at the end of the loading history appears in Figure 23.

The same analysis was rerun with a shear stress loading in the opposite direction: $\Delta\bar{\sigma}^*_{12} = 10.0 * A_0 = 0.0451$. The same results for the final configuration, contact forces, and uniform motion were obtained under the appropriate rotation. Thus, the model is invariant under rigid body rotations and can capture the isotropy of the assembly packing.

Fifty eight-particle irregular assembly

The initial control volume configuration for this example is shown in Figure 12. This control volume represents a first step towards the general analysis of randomly arranged and randomly sized particles. This repeating cell configuration isolates the effect of a random arrangement of particles on the overall response of the material and the performance of our model. All particles in the control volume have a radius $r = 1.0$ units. For these experiments, the two auxiliary points are arbitrarily chosen to be $\boldsymbol{A}^0$ and $\boldsymbol{A}^1$ to be $\left\{-0.002, -0.002, -1.0 \times 10^{-5}\right\}^t$ and $\left\{-0.00175, -0.00174, -2.55 \times 10^{-5}\right\}^t$, respectively.

For the examples considered here, the control volume experiences six increments of isotropic compression. The first two increments consist of $\Delta\bar{\sigma}^*_{11} = \Delta\bar{\sigma}^*_{22} = -200.0 * A_0 = -0.7842$, and the next four increments consist of $\Delta\bar{\sigma}^*_{11} = \Delta\bar{\sigma}^*_{22} = -900.0 * A_0 = -3.5291$. The isotropic compression produces prestressing effects on the elastic springs and prevents the particle contacts from breaking during the shearing process. The compression may be thought of as stabilizing the particles which may initially lie in an unstable configuration.

The particle assembly now experiences a shear stress loading in increments of $\Delta\bar{\sigma}^*_{12} = -40.0 * A_0 = -0.1568$ for different values of the hardening parameter H'. Figure 24 shows the variation of the normalized shear stress $\bar{\sigma}^*_{12}/k_T$ with the shear motion A_{12} for each choice of H'. The straight line portions of each response represent the elastic stretching of the tangential springs. As H' becomes smaller, the overall response approaches an elastic-perfectly plastic behavior.

With the same initial configuration and a hardening parameter $H' = 100.0$, the control volume is subjected to a cyclic shear loading consisting of 80 increments of $\Delta\bar{\sigma}^*_{12} = -10.0 * A_0 = -0.0392$; followed by 180 increments of $\Delta\bar{\sigma}^*_{12} = 10.0 * A_0 = 0.0392$; and finally 191 increments consisting of $\Delta\bar{\sigma}^*_{12} = -10.0 * A_0 = -0.0392$. Figure 25 shows a plot of the normalized overall shear stress response versus the uniform shear motion A_{12}. This overall response clearly indicates a hardening response resulting from the incorporation of particle contact hardening. Note that localization does not occur during any stage of loading, unloading, or reloading. The plot of the localization function near the region of the function minima and at the end of the first loading appears in Figure 26.

One hundred ninety six-particle random assembly

The initial positions of the particles are shown in Figure 17. For the examples in this section, the two auxiliary points are chosen to be $\{-0.02, -0.02, 0.0\}^t$ and $\{-0.0275, -0.0275, -5.5 \times 10^{-6}\}^t$, respectively. To ensure an initially stable initial configuration and that the particles indeed touch at contact points the control volume was isotropically compressed to an initial macroscopic stress of $\Delta\bar{\sigma}^*_{11} = \Delta\bar{\sigma}^*_{22} = -5.0 * A_0 = -75.9968$.

The numerical algorithm is next tested for convergence. Following the Newton algorithm in Box 3, the control volume is compressed with an additional isotropic stress of $\Delta\bar{\sigma}^*_{11} = \Delta\bar{\sigma}^*_{22} = -5.0 * A_0 = -75.9668$ applied in one, two, four, 10, 20, and 50 increments. Table 5 shows the predicted incremental macroscopic control volume motions ΔA_{11} and ΔA_{22}, at cumulative incremental normal stresses of $\Delta\bar{\sigma}^*_{11} = \Delta\bar{\sigma}^*_{22} = -2.5 * A_0 = -37.9984$ and $\Delta\bar{\sigma}^*_{11} = \Delta\bar{\sigma}^*_{22} = -5.0 * A_0 = -75.9968$. Note that the normal uniform motions of the control volume are not equal due to anisotropy effects, and a non-zero macroscopic shear motion $\Delta A_{12} = \Delta A_{21}$ is also produced by the isotropic stress history. The results shown in Table 5 demonstrate that the inverse algorithm is convergent under an isotropic stress field and that for a volumetric stress of $\Delta\bar{\sigma}_v = \Delta\bar{\sigma}^*_{11} + \Delta\bar{\sigma}^*_{22} = -10.0 * A_0 = -151.9936$ the error of the one-step solution for the normal motion sum, $\Delta A_{11} + \Delta A_{22}$, is in the order of 1.0% relative to the 50-step solution.

Table 5 also shows the convergence profile of the one-step solution. This profile

Table 5. Convergence test for the 196-particle assembly: isotropic compression ($k_N = k_T = 1 \times 10^4$ units).

Cumulative incremental stress, $\Delta\bar{\sigma}_{11} = \Delta\bar{\sigma}_{22} = -2.5 * A_0 = -37.9984$:

Stress increment	ΔA_{11}, %	ΔA_{22}, %
-5.00	n/a	n/a
-2.50	-0.31043	-0.34583
-1.00	n/a	n/a
-0.50	-0.31160	-0.34810
-0.25	-0.31176	-0.34841
-0.10	-0.31186	-0.34859

Cumulative incremental stress, $\Delta\bar{\sigma}_{11} = \Delta\bar{\sigma}_{22} = -5.0 * A_0 = -75.9968$:

Stress increment	ΔA_{11}, %	ΔA_{22}, %
-5.00	-0.57729	-0.64472
-2.50	-0.57976	-0.64837
-1.00	-0.58129	-0.65089
-0.50	-0.58184	-0.65176
-0.25	-0.58213	-0.65220
-0.10	-0.58230	-0.65246

n/a = not applicable

Convergence profile for stress increment, $\Delta\bar{\sigma}_{11} = \Delta\bar{\sigma}_{22} = -5.0 * A_0 = -75.9968$:

Iteration	Residual
1	7.0710678
2	1.2514259
3	1.6524780×10^{-1}
4	4.0669135×10^{-3}
5	2.0566571×10^{-5}
6	3.0604956×10^{-9}

typifies the performance of the discretized Newton method used for all numerical simulations presented thus far. The approximation (5.66) to the algorithmic tangent retains the characteristic quadratic rate of convergence typical of a Newton method when sufficiently close to the solution. Note that for the last two iterations the elements of the discretization parameters $\boldsymbol{h}^k$ become close to zero. Thus, as shown in [34], the difference approximation to the algorithmic tangent satisfies the property

(5.62) and displays the essential characteristics of the Newton method.

Next, the algorithm is tested for convergence under a shear stress field. However, the Newton method presented in Box 3 is modified to streamline the efficiency of the macroscopic level. Recognizing that the majority of the computational expense lies in each call to the microscopic level, the previous time step's converged tangent is used for the first two iterations of the new time step to establish the auxiliary points $\boldsymbol{A}^0$ and $\boldsymbol{A}^1$. Also, the tangent operator is updated every other iteration instead of at every iteration. When using the approximation (5.65), this modification utilizes a minimum of three fewer calls to the micromechanical level as outlined in Box 3 for every two iterations. When employing equation (5.66), the modification uses one fewer call for every iteration.

For this convergence test, the final configuration resulting from the one-step solution of Table 5 (i.e., under a cumulative normal stress of $\bar{\sigma}^*_{11} = \bar{\sigma}^*_{22} = -10.0 * A_0 = -151.9936$) is used as the initial configuration. From this initial condition, the control volume experiences a total shear stress of $\Delta\bar{\sigma}^*_{12} = -3.0 * A_0 = -45.5981$ applied in two, three, four, six, 12, and 30 steps. Table 6 shows the results of the convergence study and suggests that the algorithm is convergent in the sense that there exists a macroscopic shear motion to which the solution tends as the number of steps increases. Iterations for the two-step and six-step solutions failed to provide a convergent solution because the micromechanical level did not find an equilibrium configuration at the start of a time step. Table 6 also gives the convergence profile for the two-step solution. This profile again displays rapid convergence in the neighborhood of the solution but with less computational effort than the Newton method in Box 3.

Recall that the previous time step's tangent operator is employed for the first iteration of the next time step. In terms of the discretized Newton method described in Box 3, this estimate provides the auxiliary point $\boldsymbol{A}^1$ which in turn is used with $\boldsymbol{A}^0$ to approximate the algorithmic tangent operator according to either (5.65) or (5.66). If the previous step's converged tangent operator produces a poor approximation of the variation of the overall motion with respect to the macroscopic stress for the new time step, the micromechanical level may not converge to an equilibrium

Table 6. Convergence test for the 196-particle assembly: shear ($k_N = k_T = 1 \times 10^4$units).

Cumulative incremental stress, $\Delta\bar{\sigma}_{12} = -1.5 * A_0 = -22.7990$:

Stress increment	ΔA_{12}, %
-1.50	-0.26453
-1.00	n/a
-0.75	-0.26434
-0.50	-0.26429
-0.25	-0.26425
-0.10	-0.26423

Cumulative incremental stress, $\Delta\bar{\sigma}_{12} = -3.0 * A_0 = -45.5981$:

Stress increment	ΔA_{12}, %
-1.50	n/c
-1.00	-0.62574
-0.75	-0.62614
-0.50	n/c
-0.25	-0.62698
-0.10	-0.62727

n/a = not applicable; n/c = no convergence

Convergence profile for stress increment, $\Delta\bar{\sigma}_{12} = -1.5 * A_0 = -22.7990$:

Iteration	Residual
1	1.5000000
2	9.6489208×10^{-2}
3	1.2397293×10^{-2}
4	4.0669135×10^{-3}
5	1.5293010×10^{-4}
6	$1.1355753 \times 10^{-11}$

configuration. Figure 27 shows the highly non-linear relationship between the shear stress $\bar{\sigma}^*_{12}$ and the overall motion A_{11} for the smallest stress increment of the shear convergence test. This plot also contains the data from the non-converged six-step experiment. The initial estimate of the tangent operator yields a uniform motion which when combined with the converged particle configuration of the previous time step causes the micromechanical level not to converge. Thus, it is important to reiterate that whether the exact tangent operator or some approximation is employed, the inverse algorithm is at best as stable as the micromechanical level strain driven algorithm.

Using the same initial configuration and tangent updating modification as in the shear convergence test, the particle assembly now experiences a complex stress history consisting of alternating shear stress $\Delta\bar{\sigma}^*_{12} = -0.10 * A_0 = -1.5199$ and isotropic compression. Figure 28 shows the plot of the overall shear stress $\bar{\sigma}^*_{12}$ versus the macroscopic shear motion A_{12}. When the micromechanical level no longer converges, the control volume experiences two steps of isotropic compression $\Delta\bar{\sigma}^*_{11} = \Delta\bar{\sigma}^*_{22} = -5.0 * A_0 = -75.9968$. Figure 29 shows the variation of the localization function minima with the shear stress. Despite the stress point reaching a yield plateau during the second shear loading, the localization function does not become zero or negative during this experiment. The deformed control volume configuration at the end of this test appears in Figure 30.

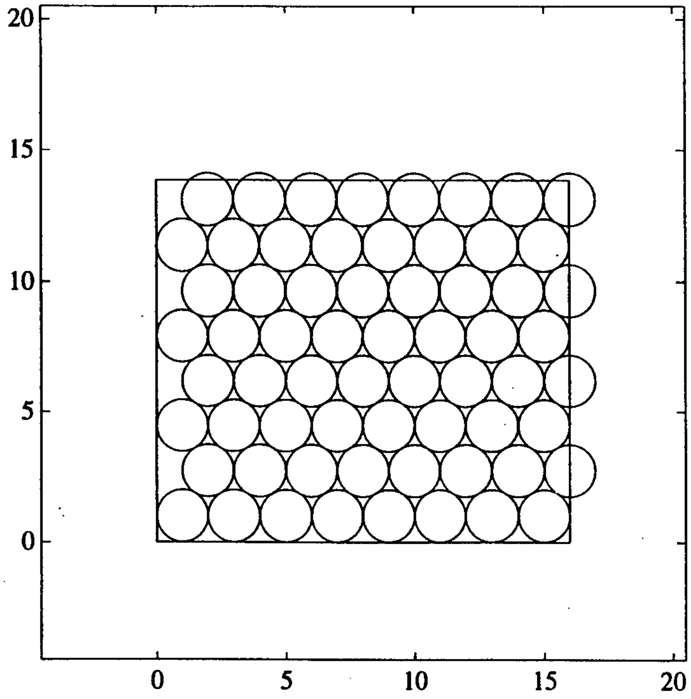
20
15
10
5
0
0
5
10
15
20

Figure 21. Initial configuration for the 64-particle closest packing control volume; particle radius = 1.0 units.

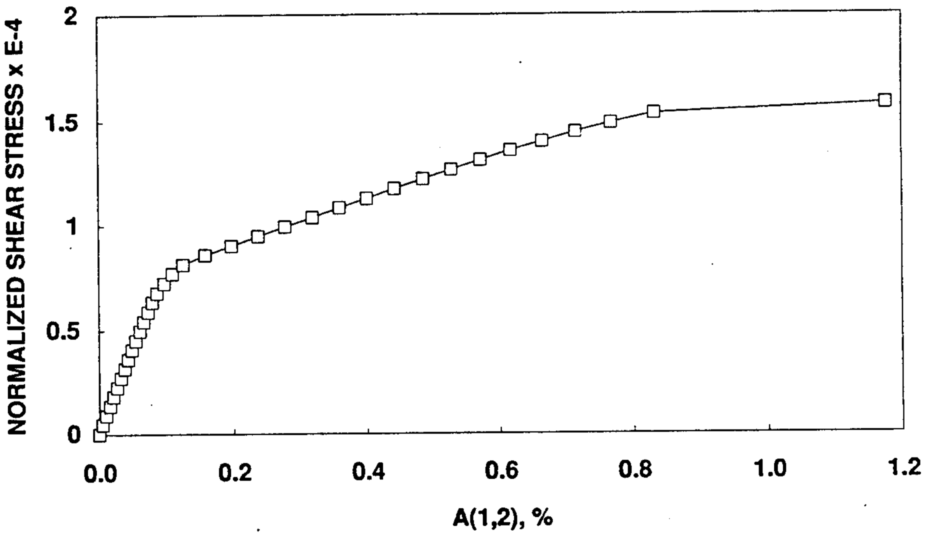

Figure 22. Normalized overall shear stress $\bar{\sigma}^*_{12}/k_T$ versus overall shear motion A_{12} showing formation of a yield plateau.

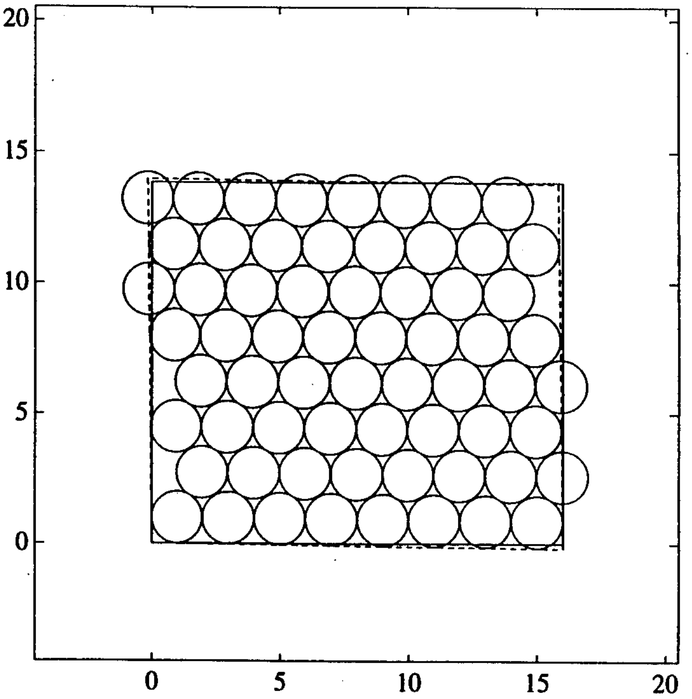

Figure 23. Deformed configuration of the 64-particle closest packed control volume at the end of the shear loading of $\Delta\bar{\sigma}^*_{12} = -10.0 * A_0 = -151.9936$; particle radius = 1.0 units.

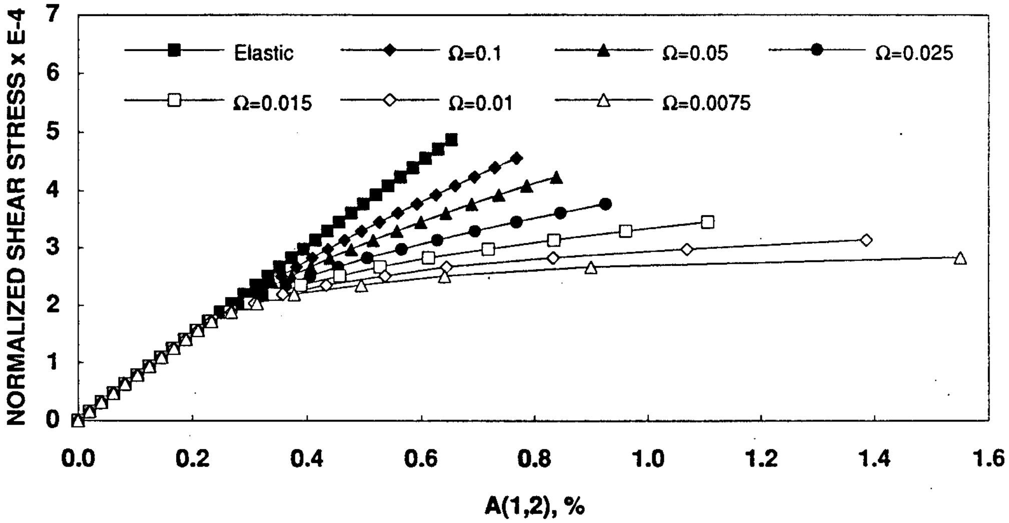

Figure 24. Normalized overall shear stress $\bar{\sigma}^*_{12}/k_T$ versus overall shear motion A_{12} showing the effects of the moduli ratio $\Omega = H'/k_T$.

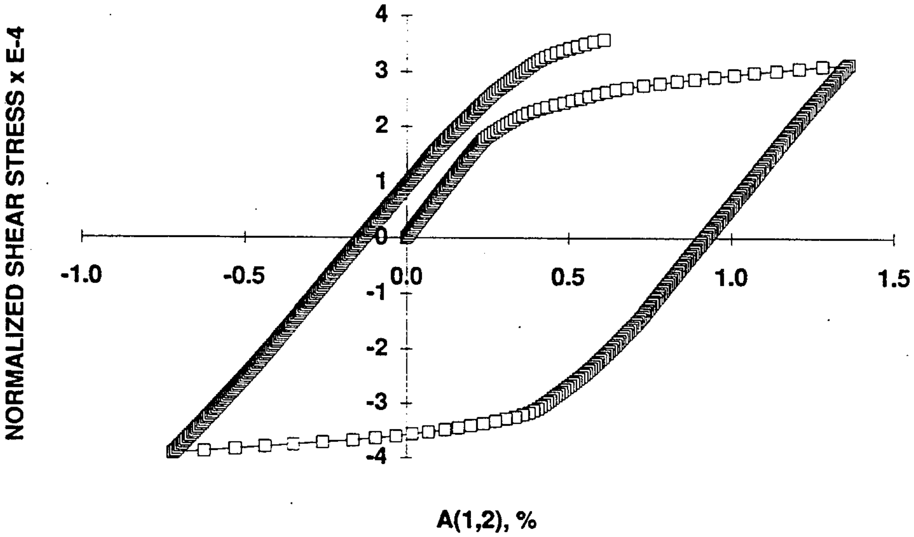

Figure 25. Cyclic testing of the 58-particle control volume showing the hysteretic response of the normalized overall shear stress $\bar{\sigma}^*_{12}/k_T$ versus overall shear motion A_{12}.

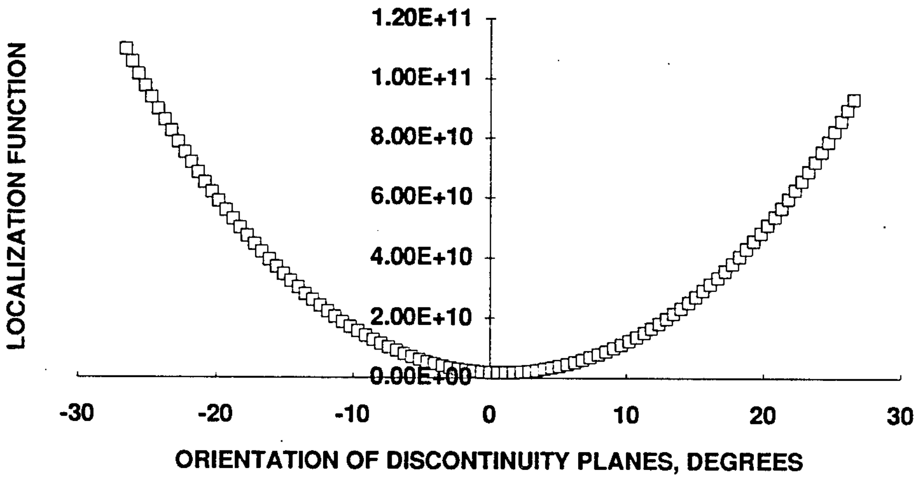

Figure 26. Localization function versus orientation of the plane of discontinuity, θ, at the end of the first loading in the cyclic test.

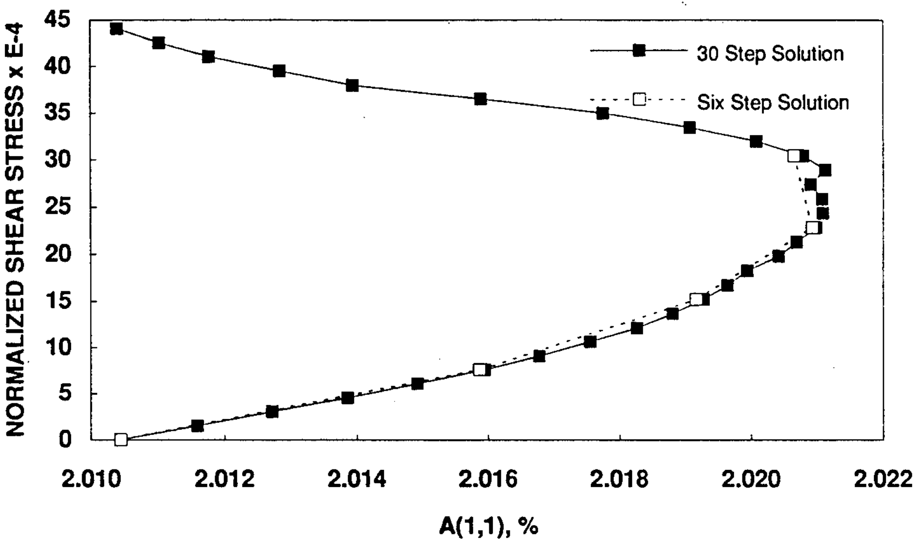

Figure 27. Normalized overall shear stress $\bar{\sigma}^*_{12}/k_T$ versus overall normal motion A_{11} showing nonlinear expansion in the x-direction during shear loading.

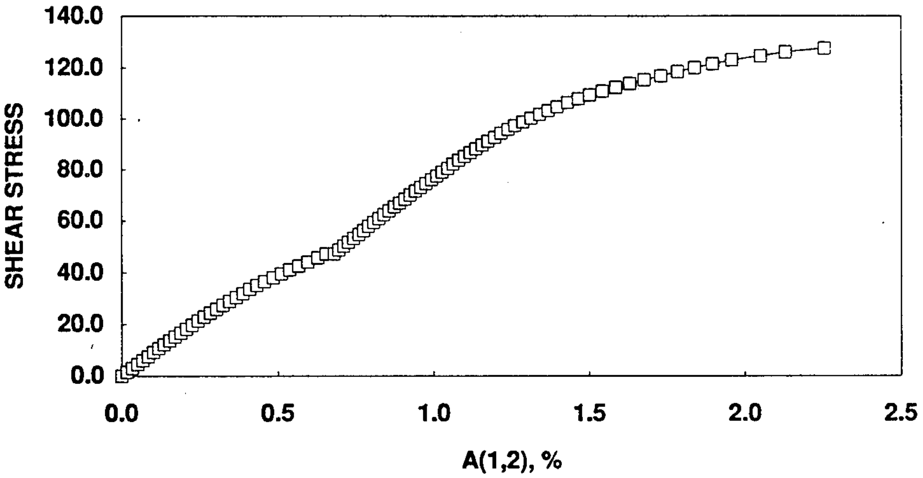

Figure 28. Overall shear stress $\bar{\sigma}^*_{12}$ versus overall shear motion A_{12} for shear loading followed by isotropic loading.

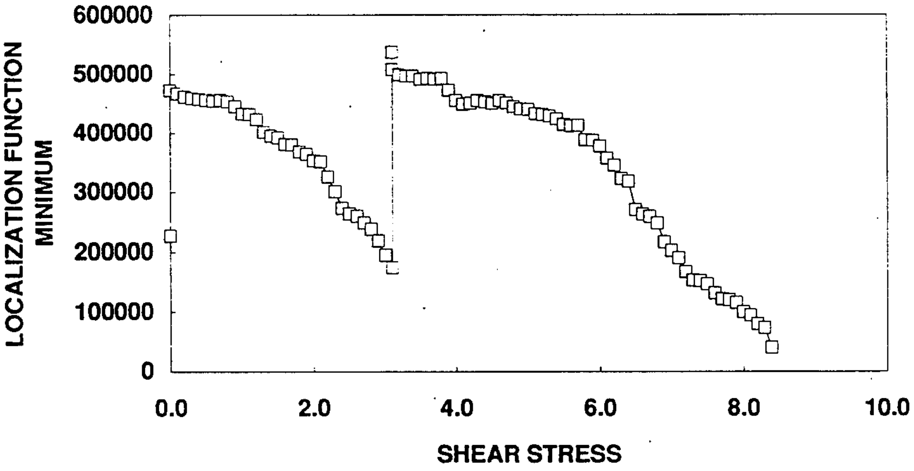

Figure 29. Localization function minimum versus overall shear stress $\bar{\sigma}^*_{12}$.

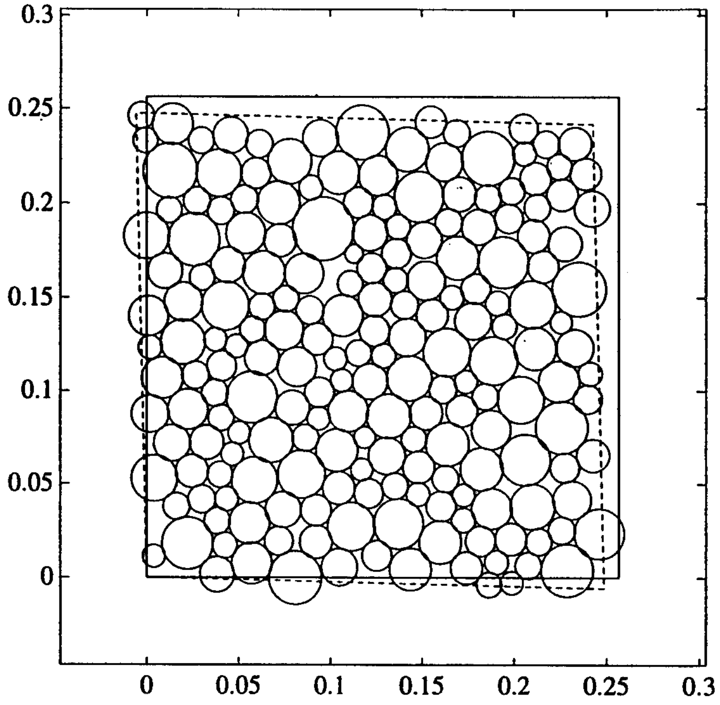

0.3
0.25
0.2
0.15
0.1
0.05
0
0
0.05
0.1
0.15
0.2
0.25
0.3

Figure 30. Deformed configuration for the 196-particle assembly; mean particle radius = 0.0092 units.

Chapter 6

Elastic Contact Laws and Validation

6.1. Introduction

In 1882, Heinrich Hertz introduced the basic premise used in contact stress theory — two bodies in contact can each be regarded as an elastic half space in the proximity of the contact region. The highly concentrated contact stresses can then be treated separately from the general distribution of existing stresses which arise from the shape of the bodies and the manner in which they are supported. Hertz's contact theory relies upon a set of basic assumptions which may be summarized as follows:

i. the surfaces are continuous and non-conforming: the significant dimension of the contact area a is much less than the the relative radius of curvature R where $1/R = 1/R_1 + 1/R_2$ and R_1 and R_2 represent the radii of the bodies in contact (i.e., $a \ll R$);

ii. the strains are small;

iii. each solid is considered as an elastic half-space: $a \ll R_1$, $a \ll R_2$, $a \ll l$ where l denotes the dimension of the bodies in depth;

iv. the surfaces are frictionless.

Assumption (i) ensures that the surfaces just beyond the contact region approximate a plane surface of a half-space. Assumption (ii) guarantees that the strains within the contact region remain within the realm of the theory of elasticity. Assumption (iii) ensures that the stress field calculated on the basis of a infinite solid will not be significantly influenced by the location of its boundaries to the highly stressed region. Finally, assumption (*iv*) is made to guarantee that only a normal pressure is transmitted between the contacting bodies.

Hertz's contact theory will be employed to derive contact laws for the normal and tangential interaction between two infinitely long cylinders. A secant approximation will be used to transform Hertz 's nonlinear contact expressions into a linear contact law dependent upon the material properties of the contacting bodies. The resulting contact stiffnesses k_N and k_T will then be substituted in the strain-driven or stress-driven algorithm. The ability of these algorithms to predict typical soil behavior will be verified by subjecting a 196-particle control volume to a specific loading history. The results of the numerical simulation will then be compared with similar plane strain experimental data.

6.2. Cylindrical bodies in contact: normal interaction

Consider two cylindrical bodies lying parallel to their axes and pressed together by a force P as shown in Figure 31. The bodies make contact over a long strip of width $2a$ parallel to the y-axis. The center of cylinder 1 and the center of cylinder 2 move towards the $x-y$ plane by displacements δ_1 and δ_2, respectively. If the cylinders did not deform, their profiles would overlap as shown in the insert of Figure 31. The displacements δ_1 and δ_2 which are measured positive into each cylinder may be found as the limiting case of an elliptical contact area where the major axis of contact corresponds to the long axis of the cylinders and becomes large compared with the semi-contact width a as shown in Mindlin [39]. The contact of two long cylindrical bodies then becomes two-dimensional in nature.

However, the cylinder contact problem may be simplified from the outset by employing assumptions $i-iv$ in the manner of Poritsky [40]. Hertz's assumptions $i-iv$ neglect the curvature of the cylinder's boundaries except near the contact region such that the spreading of the stress takes place in the same manner as in a semi-infinite solid. The two-dimensional plane strain contact configuration can then

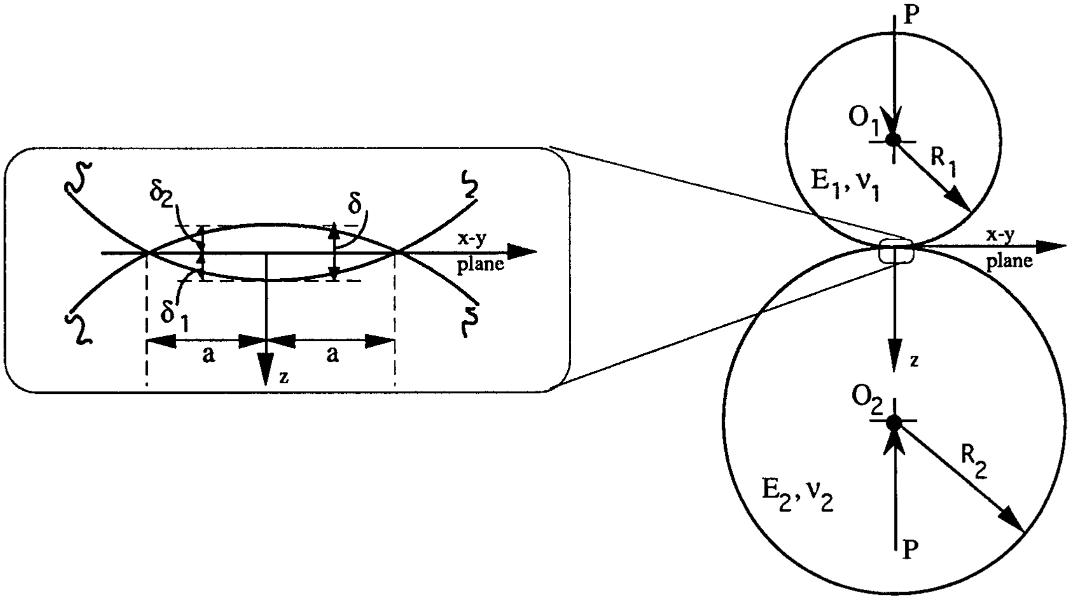

Figure 31. Cylindrical bodies in contact under a normal load P.

be transformed into an equivalent half-space loaded by the Hertz contact pressure distribution. The distribution of pressure can be written as

$$p(x) = \frac{2P}{\pi a^2}\sqrt{(a^2 - x^2)}\,, \qquad |x| < a; \tag{6.1}$$

where

$$a^2 = \frac{8PR}{\pi E^*}\,; \tag{6.2}$$

$$\frac{1}{R} = \frac{1}{R_1} + \frac{1}{R_2}\,; \tag{6.3}$$

$$\frac{1}{E^*} = \frac{1 - v_1^2}{E_1} + \frac{1 - v_2^2}{E_2}\,; \tag{6.4}$$

and where P represents the compressive force between the cylinders per unit axial length, R is the relative radius of curvature, and E^* denotes the composite modulus of the cylinders in which v_n and E_n represent the Poisson's ratio and Young's modulus respectively of cylinder n.

Now, consider cylinder 2 in Figure 31. For $z > 0$, the cylinder may be replaced by a semi-infinite solid loaded by the pressure distribution (6.1). The semi-infinite solid retains the cylinder's Poisson's ratio v_2 and Young's modulus E_2 . Following Poritsky [40], the normal deflection $\delta_2(x)$ of the half space along $z = 0$ in the direction of the pressure can be written as

$$\delta_2(x) = -\frac{4(1-v_2^2)}{\pi E_2}\frac{2P}{\pi a^2}\int_{-a}^{a}\sqrt{a^2-s^2}\ln|x-s|\,ds\ . \tag{6.5}$$

Evaluation of this integral yields

$$\delta_2(x) = \begin{cases} -\frac{4P(1-v_2^2)}{\pi E_2}\left[\frac{x^2}{a^2}+C_1\right]\ , & |x| < a \\ -\frac{4P(1-v_2^2)}{\pi E_2}\left[\ln w + \frac{1}{2w^2}\right] + C_2\,, & x > a\,; \end{cases} \tag{6.6}$$

where

$$w = \frac{1}{a}\left[x + \sqrt{x^2-a^2}\right]. \tag{6.7}$$

The constants C_1 and C_2 can be evaluated by considering the displacement δ_2 relative to some reference point where δ_2 can be considered vanishingly small. Ideally, the displacement would be evaluated relative to the region at infinity. In the case of a finite object such as a cylinder, however, the displacement must be evaluated relative to some reference point in the interior of the cylinder. As seen from the logarithmic term in equation (6.6), the displacement increases slowly with distance causing the overall displacement not to be too sensitive of the choice of the reference point. Hertz's assumptions, namely that $a \ll R_2$, guide the choice of the reference point as equal to the radius of cylinder 2. The constants C_1 and C_2 then become

$$C_1 = -\ln\frac{2R_2}{a} - \frac{1}{2}\,; \tag{6.8}$$

$$C_2 = \frac{4P(1-v_2^2)}{\pi E_2}\left[\ln\frac{2R_2}{a}\right]. \tag{6.9}$$

Now, the shortening of the branch vector connecting the centers of cylinders 1 and 2 can be evaluated. As seen from the particle kinematics developed in Chapter 2, the compression of the contact branch vector is of special interest for developing the particle contact constitutive relationship. The shortening of the branch vector lying within cylinder 2 can be evaluated from equation (6.6) to yield:

$$\delta_2(0) = \frac{4P(1-v_2^2)}{\pi E_2}\left[\ln\frac{2R_2}{a} + \frac{1}{2}\right]. \tag{6.10}$$

A similar expression can be obtained for the compression of the branch vector within cylinder 1.

The total compression δ of the two cylinders equals the summation of their individual displacements δ_1 and δ_2 as seen in Figure 31. The total compression of the branch vector can be written as

$$\delta(0) = \delta_1(0) + \delta_2(0) \tag{6.11}$$

$$= \frac{4P(1-v^2)}{\pi E}\left[\ln\frac{2R_1}{a} + \ln\frac{2R_2}{a} + 1\right]. \tag{6.12}$$

This expression for the relative approach of the centers of two infinitely long cylinders represents a nonlinear relation in terms of the contact force per unit length P. The nonlinearity arises from the dependence of the semi-contact width a on the contact force P as seen in equation (6.2).

6.3. Cylindrical bodies in contact: tangential interaction

When considering a tangentially loaded point of contact, a distinction must be made between slip and sliding. Slip occurs when there is a relative tangential displacement over only a portion of the contact surface. The region within which no relative tangential displacement occurs is termed the 'stick' region. In contrast, sliding occurs when tangential force reaches a critical value to cause relative displacement over the whole contact surface. The particular case considered here will be elastic bodies in contact under the condition of no slip. When the tangential traction does not exceed the limiting value, the no slip condition requires that all surface points within the 'stick' region undergo the same tangential displacement.

The specific case of interest consists of the compression of two infinitely long cylinders by a normal force P per axial length and the subsequent application of a

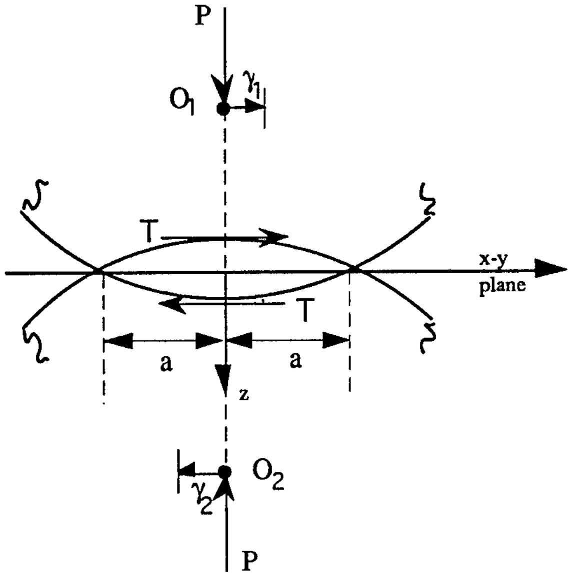

Figure 32. Tangential displacements of two contacting cylinders.

tangential force T per unit length. The Hertz contact theory of the previous section gives the pressure distribution arising from the force P, the semi-contact width a, and the total normal displacement δ of the cylinders. The complete contact width $-a \leq x \leq a$ represents the 'stick' area where no slip occurs. Figure 32 shows the tangential force T at the contact interface and the resulting tangential, elastic displacements of the contact strip. The tangential displacements γ_1 and γ_1 represent the tangential displacement of the center of cylinder 1 and 2 respectively. Note that the center of each cylinder has been considered distant from the loaded region.

Mindlin [39] recognized that if no slip occurs at the contact surface, no change in the normal component of traction occurs across the surface. Thus, when the bodies have the same elastic properties, the shape and size of the contact area and the distribution of the normal pressure will be independent of the tangential force [41]. The profiles of the two contacting surfaces fix the shape and size of the contact area. The stresses and deformations resulting from a normal pressure and the tangential traction will be independent of each other, and superposition can be employed to find the resultant stress.

Consider two cylinders 1 and 2 in contact over a region $|x| < a$ on $z = 0$ and subject to a tangential traction given by

$$t(x) = \frac{2T}{\pi a^2}\sqrt{(a^2 - x^2)}\,, \qquad |x| < a. \tag{6.13}$$

Again, the assumptions of Hertz can be employed to transform the problem into an elastic half space loaded by the tangential traction (6.13) over $|x| < a$.

The tangential displacements γ_1 and γ_2 can be evaluated by employing their basic analogy with the normal displacements δ_1 and δ_2. Under the action of identical distributions of tangential and normal tractions $t(x)$ and $p(x)$, the tangential displacements γ_1 and γ_2 analogous with the normal displacements δ_1 and δ_2. For example, the normal tractions given in (6.1) along the plane boundary of the half space can be replaced by the tangential tractions (6.13), and the normal displacements δ_1 and δ_2 found in the previous section can be replaced by the tangential displacements γ_1 and γ_2 respectively. The analogy assumes that the same reference point has been used to evaluate the constants.

By employing the normal–tangential analogy, the solution for the relative approach of the centers of the cylinders given in equation (6.12) can be employed to write the total tangential displacement γ of the centers of the cylinders as

$$\gamma(0) = \gamma_1(0) - \gamma_2(0) \tag{6.14}$$

$$= \frac{4T(1 - v^2)}{\pi E}\left(\ln\frac{2R_1}{a} + \ln\frac{2R_2}{a} + 1\right). \tag{6.15}$$

Note that since the cylinders experience mutually equal and opposite tangential tractions, their displacements $\gamma_2(0)$ and $\gamma_1(0)$ in (6.14) will be of opposite signs.

Mindlin [39] considered the general case of a normal and tangential forces applied across an elliptic contact surface of a pair of elastic bodies. For example, the solution of the tangential displacements for an elliptical contact assuming no slip is given by

$$\gamma = \frac{T}{\pi G}\left[\boldsymbol{K} - \frac{v}{\kappa^2}(\boldsymbol{K} - \boldsymbol{E})\right] \tag{6.16}$$

$$\kappa^2 = 1 - a^2/\ell^2\,, \tag{6.17}$$

and G denotes the shear modulus, $\boldsymbol{K}$ and $\boldsymbol{E}$ are complete elliptic integrals of the first and second kind, respectively, and ℓ is the axial length of the contact area. The contact stresses for the two-dimensional case of contact between two cylinders may be obtained from these solutions as a limiting case by allowing the contact area to become infinitely long along the long axis of the cylinders. The resulting relations for the normal and tangential displacements are then given by equations (6.12) and (6.15).

6.4. Linearization of the contact laws

The contact laws for the normal and tangential interaction of long cylindrical bodies given by equations (6.12) and (6.15) represent nonlinear relationships between the contact force and displacement. The nonlinearity arises from the displacement's logarithmic variation with the normal contact force P. Simplified expressions for the normal and tangential contact laws can be derived with a secant approximation.

Consider minimum and maximum normal contact forces P_{min} and P_{max}. The slope of the line connecting these two points on the nonlinear contact laws given in equations (6.12) and (6.15) defines the secant approximation. For choosing a value of the minimum normal contact force, the condition of incipient contact requires $P_{min} = 0$. Two criterion guide the choice of the maximum normal contact force P_{max}. First, the Hertz assumptions $i - iv$ demand that P_{max} satisfy the requirements of small strain, namely $a \ll R$. Second, the accuracy of the secant approximation demands that P_{max} be similar to the actual maximum normal force between the two cylindrical bodies. With $P_{min} = 0$ and the appropriate choice for P_{max} that satisfies these criterion, the secant approximation to the Hertzian contact laws given in equations (6.12) and (6.15) take the form

$$P = k_N \delta \tag{6.18}$$

$$T = k_T \gamma \tag{6.19}$$

where k_N and k_T denote the slopes of the normal and tangential linear relations, respectively. Physically, k_N and k_T may be interpreted as linear normal and tangential contact spring constants.

Consider expressions for the normal and tangential contact stiffnesses k_N and k_T. The normal Hertzian contact law (6.12) repeated here for convenience as

$$\delta(0) = \frac{4(1-v^2)}{\pi E}\left[\ln\frac{R_1 R_2 \pi E^*}{2RP} + 1\right] P \tag{6.20}$$

where the semi-contact width a (6.2) has been employed. Substituting the minimum and maximum normal forces $(0, P_{max})$ into this expression defines the slope of the normal contact approximation and gives

$$k_N = \frac{\pi E}{4(1-v^2)}\left[\ln\frac{R_1 R_2 \pi E^*}{2RP_{max}} + 1\right]^{-1}. \tag{6.21}$$

Thus, the normal secant approximation (6.18) can be written as

$$P = \underbrace{\frac{\pi E}{4(1-v^2)}\left[\ln\frac{R_1 R_2 \pi E^*}{2RP_{max}} + 1\right]^{-1}}_{k_N} \delta\,. \tag{6.22}$$

In a similar manner, the secant approximation to the Hertzian tangential law can be written as

$$T = \underbrace{\frac{\pi E}{4(1-v^2)}\left[\ln\frac{R_1 R_2 \pi E^*}{2RP_{max}} + 1\right]^{-1}}_{k_T} \gamma\,. \tag{6.23}$$

Note that the normal and tangential contact stiffnesses are equal and depend upon the material properties and radii of the contacting cylinders.

Figure 33 contains a comparison of the nonlinear Hertz contact law and its secant approximation (6.22) for similar cylinders. The cylinders possess identical material and geometric properties. The basis of the comparison consists of the nondimensionalized contact force $P/(kR_1)$ and the normal indentation δ/R_1 where $k = \pi E/4(1-v^2)$ and $R_1 = R_2 = 1.0$ consistent units implied. The range of the secant approximation has been restricted to the region where $0 \leq P/k \leq 1/625$. In general, over the region of interest the linearized contact law provides a good approximation to the Hertzian law.

Expressions for the contact forces $\mathcal{F}_{n+1}$ discussed in Chapter 2 can be obtained from the discretization of the linearized contact laws (6.22)-(6.23). Assume that at time t_n the contacting cylinders A and B — particles in plane strain — have well defined centroids $\boldsymbol{x}^A$ and $\boldsymbol{x}^B$. The contact force P between two cylinders can now represent the normal component of the contact force f_N at time t_{n+1}. The normal contact law can now be written in incremental form as

$$f_{n+1} = -H_\epsilon(\delta_{n+1}) k_N \delta_{n+1} \tag{6.24}$$

where the ramp function $H_\epsilon(\delta_{n+1})$ is as defined in Chapter 2, the overlap δ_{n+1} equals the shortening of the branch vector $\delta(0)$, and k_N denotes the normal contact stiffness as defined by (6.21).

For the tangential interaction, the contact stiffness in (6.23) defines the elastic tangential force. When the contact mode is 'stick,' the tangential component of the contact force f_T at time t_{n+1} can be written as

$$(f_T)_{n+1} = (f_T)_n + H_\epsilon(\delta_{n+1}) k_T \Delta\gamma \tag{6.25}$$

where the $\Delta\gamma$ represents the increment of tangential displacement. Note that the tangential displacement γ of (6.23) represents the total elastic tangential displacement at the contact. If the contact is in 'sliding' mode, the tangential force then becomes

$$(f_T)_{n+1} = (f_T)_n + H_\epsilon(\delta_{n+1}) k_T (\Delta\gamma - \Delta\gamma^p) \tag{6.26}$$

The remaining results of Chapter 2 apply for these contact modes assuming that over the finite incremental motion the particles remain in contact throughout the time step. Now, the incremental normal and tangential contact laws (6.24)-(6.26) form the basis of the contact model between two particles. Thus, the Hertz solution to the contact of infinite circular cylinders forms the foundation of the contact model underlying the numerical algorithms of Chapter 4 and Chapter 5.

6.5. Numerical simulations

With the addition of the Hertz solution to the contact model, the behavior of the numerical material takes on the added physical meaning of the response of a similarly graded granular material subject to plane strain loading. Herein, the circular cylinders represent the action of individual soil particles contained in a repeating control volume subject to plane strain loading. The predicted behavior of the numerical material can now be compared with experimental plane strain test data.

Before comparing the numerical model and experimental tests, one must consider and clarify the limitations and shortcomings of such a comparison. Consider the plane strain basis of the comparison. The numerical model represents a classical plane strain formulation with infinitely long cylinders identified as soil particles. However, actual three-dimensional tests model plane strain behavior by restricting deformation in the longest specimen direction. The typically tabular shaped samples contain a very large number of finite sized particles. Thus, the comparison reduces to a purely plane strain numerical model and a three-dimensional experiment configured to model plane strain behavior.

Also, consider the boundary condition basis of the comparison. Recall that the assumption of homogeneous deformation is implicit in the numerical model. The basis for comparison of the numerical model and experimental results rests on the experimental apparatus' ability to allow homogeneous deformation. However, such effects such as end plate friction and membrane-soil interaction are inherent in physical experiments. The prevalence of these factors in experimental results directly influences the applicability of the homogeneous deformation assumption for the experiment.

Finally, consider the possible scaling effects produced by using a relatively small number of particles to represent a soil sample. The numerical model assumes that the particles in the control volume are sufficiently representative to capture the geometric characteristics of the soil. Yet, a large number of particles are typically necessary to capture a soil's gradation, packing, and overall void structure. Thus, a trade off typically exists between the cost of the numerical simulation, i.e., the number of particles in a control volume, and how representative the control volume will be of the model soil.

Experimental results

Many investigators [42–47] have studied the plane strain behavior of granular materials. Vardoulakis [48] and Vardoulakis and Graf [49] present extensive studies of the plane strain compression of dry sand that appear representative of the behavior of granular materials in plane strain loading. Their test samples appear tabular in shape with their long axis perpendicular to the loading direction. The sample is placed in a conventional triaxial loading frame with two stiff frictionless plates to restrict the strain to two dimensions. The cell pressure remains constant while the loading piston compresses the sample under constant driving speed. The piston displacement and force are measured throughout the test. Vardoulakis and Goldscheider [50] explain in greater detail the biaxial apparatus and testing procedure.

Two different experimental results will be used for comparison with the numerical model. The first test from Vardoulakis [48] consists of the plane strain compression of a dry Osterchelde sand at a confining pressure of 29.43 $\mathrm{N/cm^2}$. The sample's initial void ratio equaled $e = 0.621$ and specific gravity was $G_s = 2.66$. The second test from Vardoulakis and Graf [49] was performed at a confining pressure of 19.62 $\mathrm{N/cm^2}$ on a dry sample of Karlsruhe sand with an initial void ratio equal to $e = 0.577$.

The reported experimental data for both tests consists of the variation of the axial force P_a with the axial displacement u_a. For comparison with the numerical simulations, the deviator stress $\Delta\sigma_a$ and the axial strain ϵ_a have been calculated with the following equations:

$$\Delta\sigma_a = \sigma_1 - \sigma_3 = \frac{P_a}{A_0} \tag{6.27}$$

$$\epsilon_a = \frac{u_a}{l_a} \tag{6.28}$$

where A_0 represents the initial unloaded cross-sectional area of the sample, and l_a

denotes the sample's initial length in the direction of loading. The variation of the deviator stress $\Delta\sigma_a$ and axial strain ϵ_a can now be plotted.

Numerical material properties

The two control volumes used in the numerical simulations consist of parallelepipeds of infinite circular cylinders. Each volume contains 49 and 196 particles (cylinders) randomly arranged. All loading takes place perpendicular to the axis of the cylinders. Recall that the control volumes represent one cell within a periodic structure. The control volume of interest is surrounded in all directions by identical parallelepipeds. All particles within the cell possess the same material properties but not necessarily the same geometric properties. The particles may be randomly dispersed throughout the cell and have varying radii.

In choosing the material properties, namely, the Young's modulus and Poisson's ratio, of the repeating cell particles consideration must be given to the composition and origin of soil particles. The principal constituents of the solid phase of soils are various amounts of crystalline and noncrystalline clay materials, nonclay minerals, and precipitated salts. In particular, nonclay materials such as sands, gravels, and the majority of silts are typically comprised of rock fragments or mineral grains of the common rock-forming minerals. Thus, the properties of the pre-existing rock from which the individual grains originate can be used to estimate the material properties of the particles in the numerical model.

Consider numerical soil particles that originate from rock fragments or mineral grains of common sedimentary rocks such as sandstone, siltstone, shale, and claystone. The particle size of the reference materials varies from $.2 - .00625$ cm for sandstone, $.00625 - .00039$ cm for siltstone, and $< .00039$ cm for shale and claystone. The Young's modulus and Poisson's ratio of these common quartz materials have been determined from unconfined compression tests. The rock samples are typically core specimens of length approximately twice the diameter. A summary of these properties for the reference materials and many other common rock materials can be found in Physical Properties of Rocks and Minerals [51]. The Young's modulus and Poisson's ratio of the numerical soil particles are chosen to lie within the range

Table 7. Model and material parameters.

Model parameters

Macromechanical error tolerance: RTOL $= 1.0 \times 10^{-7}$.

Micromechanical error tolerance: rtol $= 1.0 \times 10^{-8}$.

Material constants

Particle Young's modulus: $E = 0.25 - 2.0$ GPa.

Particle Poisson's ratio: $v = 0.20$.

Particle friction angle: $\phi = 30°$.

Particle contact cohesion: $\alpha_0 = 0$.

Contact hardening parameter: $H' = 0$.

---

of the reference material's properties.

Table 7 summarizes the model and material parameters of interest. The error tolerances listed represent the convergence criterion used in the numerical algorithms described in Chapter 4 and Chapter 5. A Young's modulus in the range of 0.25 – 2.0 GPa and a Poison's ratio equal to 0.20 has been used. All numerical simulations assume an elastic-perfectly plastic contact model for each particle contact by employing a contact hardening parameter equal to $H' = 0$.

Forty nine-particle control volume

The initial control volume configuration for this example is shown in Figure 34. The control volume configuration isolates the effect of a random arrangement of particles from the effect of randomly sized particles. All particles in the repeating cell have a radius equal to 0.0092 cm. This particular radius has been chosen to equal the mean particle radius of a randomly sized and randomly arranged 196-particle control volume. The voids in the particle configuration seen in Figure 34 have been created by removing seven particles from a closest packed arrangement of 56 particles. The initial cell contains 126 particle contacts and has dimensions of 0.12880 cm × 0.12748 cm.

For all simulations, the value of the maximum normal contact force between two particles equals $P_{max} = 2.0$ N for all particle contacts in the repeating cell. Thus, the normal and tangential contact stiffnesses remain constant for all particle contacts. Also, the ramp function ε equals zero. Recall that ε defines a finite transition zone from no-contact to full-contact. With $\varepsilon = 0$, an exact simulation of the abrupt transition to full contact can be obtained. As a result, the ramp function $H_\varepsilon(\delta_{n+1})$ exactly models the Heaviside function $H(\delta)$ and has the form

$$H_\varepsilon(\delta_{n+1}) = \begin{cases} 1, & \text{if } \delta_{n+1} > 0; \\ 0, & \text{if } \delta_{n+1} \leq 0. \end{cases} \tag{6.27}$$

Finally, the overall stress state of the control volume at the end of each timestep has been calculated using a volume equal to the current cross sectional area times a unit thickness. The stress field then becomes a Cauchy representation of the stress state since the current deformed configuration has been used.

The first numerical experiment reproduces the confining stress of 29.43 N/cm^2 in the Vardoulakis [48] test on dry Osterchelde sand. The control volume experiences two increments of isotropic stress of $\Delta\bar{\sigma}^*_{11} = \Delta\bar{\sigma}^*_{22} = -14.715$ N/cm^2; $\Delta\bar{\sigma}^*_{12} = 0.0$. Following the isotropic compression, the control volume experiences increments of axial loading of $\Delta\bar{\sigma}^*_{11} = -0.50$ N/cm^2; $\Delta\bar{\sigma}^*_{22} = \Delta\bar{\sigma}^*_{12} = 0.0$ until the algorithm no longer converges.

Figure 35 presents the response of the control volume by plotting the variation of the deviator stress $\Delta\bar{\sigma}^* = \Delta\bar{\sigma}^*_{11} - \Delta\bar{\sigma}^*_{22}$ versus the axial strain ϵ_1 along with the experimental results obtained by Vardoulakis [48]. The numerical simulations have been run for four different Young's moduli of 0.25, 0.50, 1.00, and 2.00 GPa. Figure 35 indicates that as the Young's modulus increases the response of the control volume becomes stiffer as indicated by a steeper deviator stress-axial strain curve. Figure 36 shows an enlargement of the initial stress-strain behavior of the numerical and experimental results. All four values of the Young's modulus provide good correlations with the experimental results. Figure 37 shows the deformed configuration of the control volume at the end of the numerical simulation with the Young's modulus equal to $E = 0.25$ GPa. At the end of this loading, the control volume contains 119 particle contacts of which 35 have plastified, i.e., entered "slip" mode, and a maximum normal contact force equal to 3.09856 N.

Figure 38 presents the behavior of the control volume to a loading history similar to the one employed by the Vardoulakis and Graf [49] on Karlsruhe sand. The control volume experiences an isotropic stress of $\Delta\bar{\sigma}^*_{11} = \Delta\bar{\sigma}^*_{22} = -9.81$ N/cm^2; $\Delta\bar{\sigma}^*_{12} = 0.0$ applied in two increments to provide a confining stress of 19.62 N/cm^2. Next, the loading consists of axial stress increments of $\Delta\bar{\sigma}^*_{11} = -0.50$ N/cm^2; $\Delta\bar{\sigma}^*_{22} = \Delta\bar{\sigma}^*_{12} = 0.0$. The predicted behavior at the same four different Young's moduli appear along side the experimental test data. Like the previous simulation, the predicted stress-strain behavior appears similar to the experimental data. In particular, Figure 39 shows the comparison of predicted and experimental data at small strains. The deformed control volume at the end of the loading with Young's modulus equal to $E = 0.25$ GPa can be seen in Figure 40. At this point, the repeating cell contains 119 contact of which 37 have plastified and a maximum normal contact force equal to 2.11516 N.

One hundred ninety six-particle control volume

The initial control volume configuration for this example is shown in Figure 41. The repeating cell contains 196 randomly sized randomly arranged particles originally configured by Kuhn [36]. The mean particle radius equals 0.0092 cm, and the initial cell dimensions are 0.2566 cm × 0.2565 cm. Unless otherwise noted the model and material parameters equal those listed in Table 7. Three analyses have been performed to evaluate the performance of the numerical model on a randomly configured control volume. The first analysis considers the sensitivity of the model to certain parameters such as the ramp function ε and maximum normal contact force P_{max}. The second analysis evaluates the convergence characteristics of the model. The final analysis compares the deviator stress-axial strain behavior with experimental results.

Sensitivity analysis

The numerical model performance is tested for sensitivity to variations in the ramp function ε and maximum normal contact force P_{max}. For all sensitivity simulations, the control volume experiences a loading history consisting of two increments of isotropic compression followed by axial loading increments of $\Delta\bar{\sigma}^*_{11} = -0.50$ N/cm^2; $\Delta\bar{\sigma}^*_{22} = \Delta\bar{\sigma}^*_{12} = 0.0$.

In the ramp function study, the two isotropic compression increments equal $\Delta\bar{\sigma}^*_{11} = \Delta\bar{\sigma}^*_{22} = -14.715$ N/cm^2; $\Delta\bar{\sigma}^*_{12} = 0.0$, and the Young's modulus and P_{max} equal 2.0 GPa and 2.0 N, respectively. Three different values of ε have been defined: 0, $0.05 * R_{min}$, and $0.1 * R_{min}$ where R_{min} equals the radius of the smallest particle in the control volume. For the 196-particle control volume, R_{min} equals 0.00503 cm. Thus, the ramp function creates a constant layer of softer material of thickness $\varepsilon/2$ around each particle in the control volume. For example, when $\varepsilon = 0.05 * R_{min}$, every particle in the repeating cell has a softer layer of thickness equal to 5% of the smallest particle radius or 0.0025 mm.

With the ramp function ε equal to zero, the model failed to converge for the initial increments of isotropic compression. The random sizes of the particles within the repeating cell naturally cause relatively large particles to come into contact with smaller particles. Since the contact stiffnesses k_N and k_T depend on the radii of the contacting particles, the contact stiffnesses throughout the repeating cell vary depending on which particles lie in contact. Thus, the different sized particles in the 196-particle control volume produces a numerically "stiff" system. This behavior can be contrasted with the performance of the 49-uniformly sized particle control volume. In this case, the contact stiffnesses k_N and k_T are constant for all contacts in the control volume. A ramp function equal to zero does not hinder the convergence as shown in Figure 35 and Figure 38.

The performance of the model with non-zero ramp function can be seen in Figure 42. The deviator stress-axial strain behavior for ε equal to $0.05 * R_{min}$ and $0.1 * R_{min}$ have been plotted against the experimental data for Osterchelde sand [48]. The figure shows the better convergence behavior of the model as it becomes less stiff with a larger ramp function. However, the stress-strain behavior does not differ significantly in the initial portion of the loading history. Thus, a larger ramp function enhances the convergence of the model without significantly sacrificing accuracy. Yet, care should be exercised while choosing a value of ε. A large of a ramp function could contaminate the accuracy of the solution by creating too large of a soft band around the particles.

The sensitivity of the model to the choice of the maximum normal contact force P_{max} is investigated next. The two increments of isotropic compression equal $\Delta\bar{\sigma}^*_{11} = \Delta\bar{\sigma}^*_{22} = -9.81$ N/cm^2; $\Delta\bar{\sigma}^*_{12} = 0.0$. Figure 43 contains the stress-strain behavior with a Young's modulus of 0.25 GPa and P_{max} equal to 35.0, 10.0, and 2.0 N. Also, indicated in the figure are the values of the actual maximum normal contact force P^{act}_{max} in the control volume at the end of the simulation. Figure 43 shows a similar stress-strain behavior for different values of P_{max} in the early portions of the simulations. As the value of P_{max} approaches the value of P^{act}_{max}, the secant approximation to the Hertzian contact laws becomes more accurate. Correspondingly, the convergence properties of the model improve.

Convergence analysis

The numerical model is next tested for convergence. The Young's modulus and ramp function for the two convergence analyses equal 0.50 GPa and $0.1 * R_{min}$, respectively. In the first convergence test, the control volume initially experiences a confining stress of 29.43 N/cm^2 applied in two increments of $\Delta\bar{\sigma}^*_{11} = \Delta\bar{\sigma}^*_{22} = -14.715$ N/cm^2; $\Delta\bar{\sigma}^*_{12} = 0.0$. The second test uses a confining stress of 19.62 N/cm^2 applied in two increments of $\Delta\bar{\sigma}^*_{11} = \Delta\bar{\sigma}^*_{22} = -9.81$ N/cm^2; $\Delta\bar{\sigma}^*_{12} = 0.0$. The control volume is then compressed axially to a deviator stress of $\Delta\bar{\sigma}^* = 15$ N/cm^2 in 3, 30, 150 increments of $\Delta\bar{\sigma}^*_{11}$.

Table 8 presents the results of the convergence study. The results indicate that the model is convergent in the sense that an axial strain exists to which the solution tends as the number of steps increases. For the simulation with a confining stress of 29.43 N/cm^2, the error of the three-step solution is in the order of 0.5% relative to the 150-step solution. For the test with a confining stress of 19.62 N/cm^2, the model failed to converge for the largest increment of axial strain. As the increment size

Table 8. Convergence test for the 196-particle assembly: $E = 0.50$ GPa.

Confining stress: $\bar{\sigma}^*_{11} = \bar{\sigma}^*_{22} = 29.43$ N/cm^2; deviator stress: $\Delta\bar{\sigma}^* = 15.0$ N/cm^2.

Axial stress increment (N/cm^2)	ΔA_{11}, %
-5.0	-0.38375
-0.5	-0.38539
-0.1	-0.38555

Confining stress: $\bar{\sigma}^*_{11} = \bar{\sigma}^*_{22} = 19.62$ N/cm^2; deviator stress: $\Delta\bar{\sigma}^* = 15.0$ N/cm^2.

Axial stress increment (N/cm^2)	ΔA_{11}, %
-5.0	n/c
-0.5	-0.48953
-0.1	-0.48982

n/c = no convergence

decreased, the results appeared convergent in the same manner as the convergence test at the higher confining stress.

Simulations of experimental tests

The behavior of the 196-particle control volume is compared to the experimental data for Osterchelde and Karlsruhe sands. The loading history for these numerical simulations is identical to the corresponding tests on the 49-particle repeating cell. Again, the effect of different Young's moduli has been investigated with $E = 0.25$, 0.50, 1.00, and 2.00 GPa. The ramp function, however, now equals $0.1 * R_{min}$.

Figure 44 shows a comparison of the deviator stress-axial strain behavior of the repeating cell at a confining stress of 29.43 N/cm^2 with that of the Osterchelde sand [48]. The predicted behavior at all four values of the Young's modulus provide good correlations with the experimental results particularly in the initial portion of the loading history. Figure 45 shows an enlargement of this region of the stress-strain graph. The simulation with the Young's modulus of 2.0 GPa provides the best correlation with the experimental data. Figure 46 presents the deformed control volume at the end of the test with $E = 0.25$ GPa. For this configuration, the control

Table 9. Initial secant modulus.

Confining stress: $\bar{\sigma}^*_{11} = \bar{\sigma}^*_{22} = 29.43$ N/cm^2.

Young's Modulus (GPa)	Secant Modulus (N/cm^2) 49 Particle Repeating Cell	Secant Modulus (N/cm^2) 196 Particle Repeating cell
0.25	33.7338	29.8073
0.50	59.1248	38.5258
1.00	99.3776	49.7157
2.00	158.3656	63.1377*

Experimental data: initial secant modulus = 76.8263 N/cm^2.

Confining stress: $\bar{\sigma}^*_{11} = \bar{\sigma}^*_{22} = 19.62$ N/cm^2.

Young's Modulus (GPa)	Secant Modulus (N/cm^2) 49 Particle Repeating Cell	Secant Modulus (N/cm^2) 196 Particle Repeating cell
0.25	33.3035	23.7078
0.50	56.6170	30.6107
1.00	90.7327	39.0597*
2.00	150.4227*	48.7559*

Experimental data: initial secant modulus = 65.6802 N/cm^2.

* Secant modulus based on the final axial stress and strain.

volume contains 428 particle contacts of which 56 have plastified, and the maximum normal contact force in the control volume equals 2.07579 N.

Figure 47 shows the stress-strain behavior of the numerical and experimental tests at a confining stress of 19.62 N/cm^2. The experimental data is for a Karlsruhe sand [49]. Again, the predicted behavior compares well with the experimental data. The observed trend of the simulations with lower Young's modulus providing better convergence is apparent in this simulation. A smaller Young's modulus makes the model less numerically "stiff" in a similar manner to the effect of a larger ramp function. Figure 48 shows the initial stress-strain behavior. Figure 49 shows the deformed repeating cell at the end of the test with $E = 0.25$ GPa. Here the control volume contains 408 contacts of which 60 have plastified, and the maximum normal contact force in the control volume equals 1.69781 N.

Table 9 contains a comparison between the initial secant modulus of the numerical simulations and experimental data. The secant modulus has been calculated for an axial strain equal to 0.5% for the 49 and 196-particle control volumes at confining stresses of 29.43 N/cm^2 and 19.62 N/cm^2. The results indicate that for the range of the Young's moduli considered the model produces an initial secant modulus of the same order of magnitude as the experimental data. In general, the 196-particle control volume performs better than the more uniform 49-particle volume in capturing the initial behavior of the material at higher Young's modulus. In both cases, however, good correlation with the experimental data can be seen.

Throughout these comparisons the numerical model predicts similar behavior under plane strain compression as reported in the experimental tests. The numerical model for the 196-particle control volume has not been proposed to exactly reproduce the observed behavior of the plane strain compression of sand reported in the literature. However, the behavior of the algorithmic specimen can only be expected to appear similar and consistent with the experimental results. The similarity of the numerical and experimental responses demonstrates the validity of the numerical model to predict plane strain responses of granular materials. Further extension of the model is now possible to such areas as creep modeling.

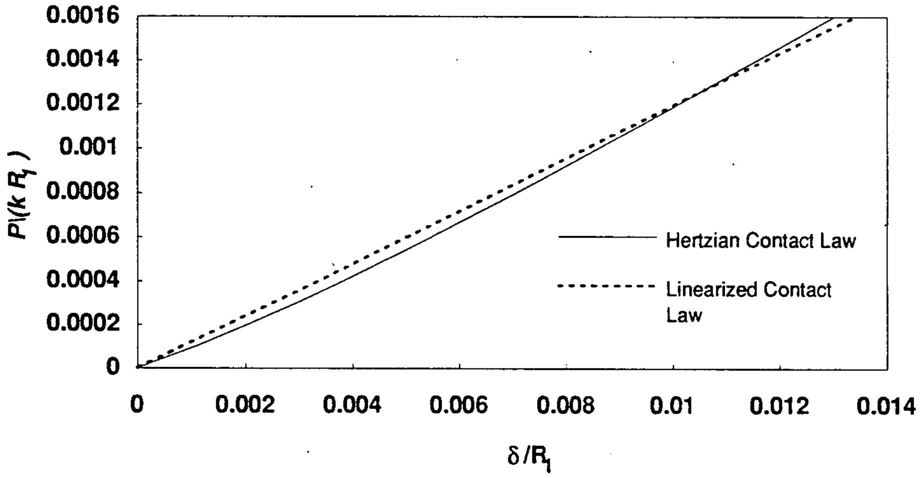

Figure 33. Comparison between the Hertzian normal contact law and the linearized contact law for similar cylinders.

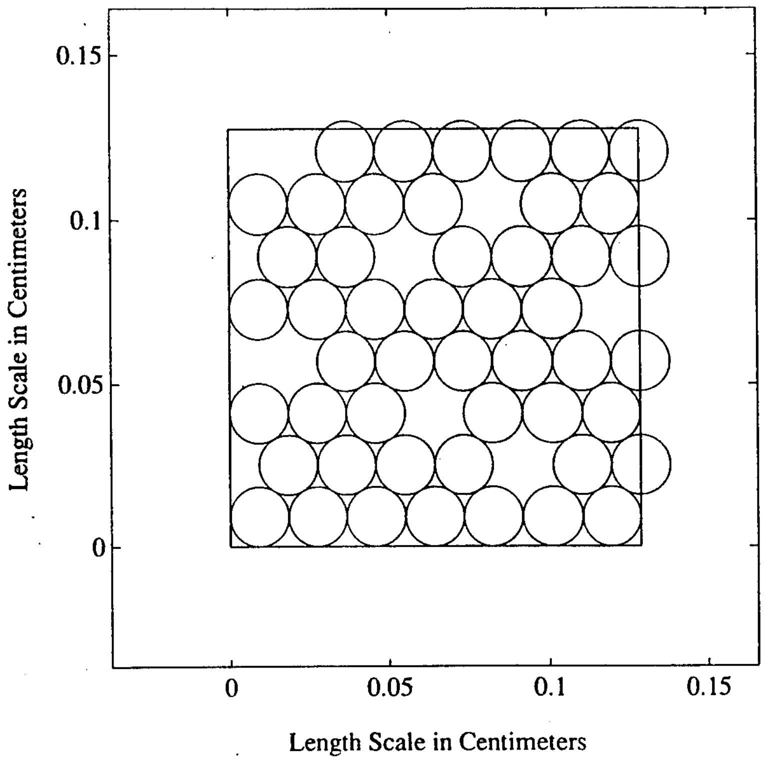
0.15
0.1
0.05
0
0
0.05
0.1
0.15
Length Scale in Centimeters
Length Scale in Centimeters

Figure 34. Initial configuration for the 49-particle control volume; particle radius $r = 0.0092$ cm.

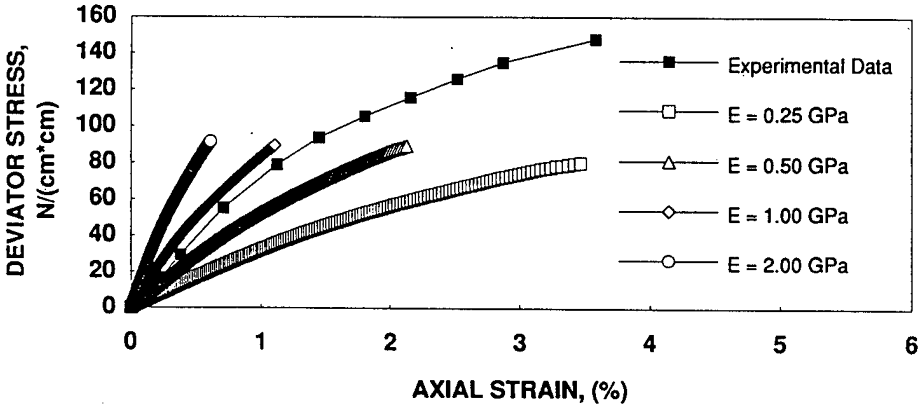

Figure 35. Deviator stress $\Delta\bar{\sigma}^*$ versus axial strain ϵ_1 for the 49-particle control volume at different Young's moduli and Osterchelde sand. Confining stress = 29.43 N/cm^2.

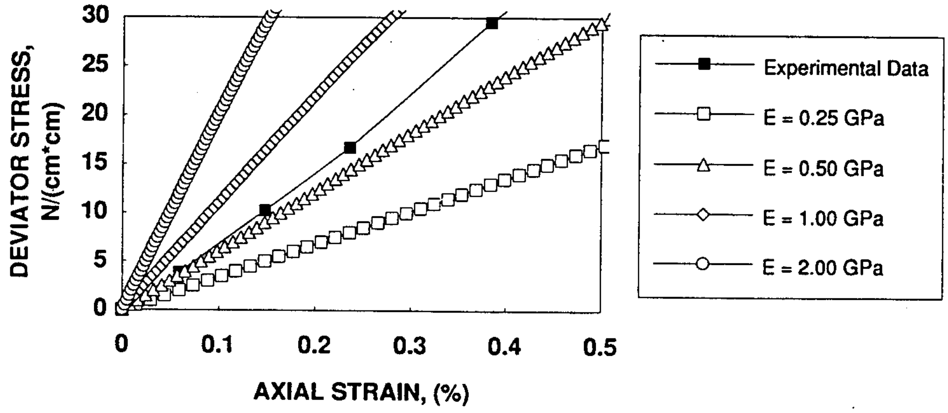

Figure 36. Initial deviator stress $\Delta\bar{\sigma}^*$ versus axial strain ϵ_1 for the 49-particle control volume at different Young's moduli and Osterchelde sand. Confining stress = 29.43 N/cm^2.

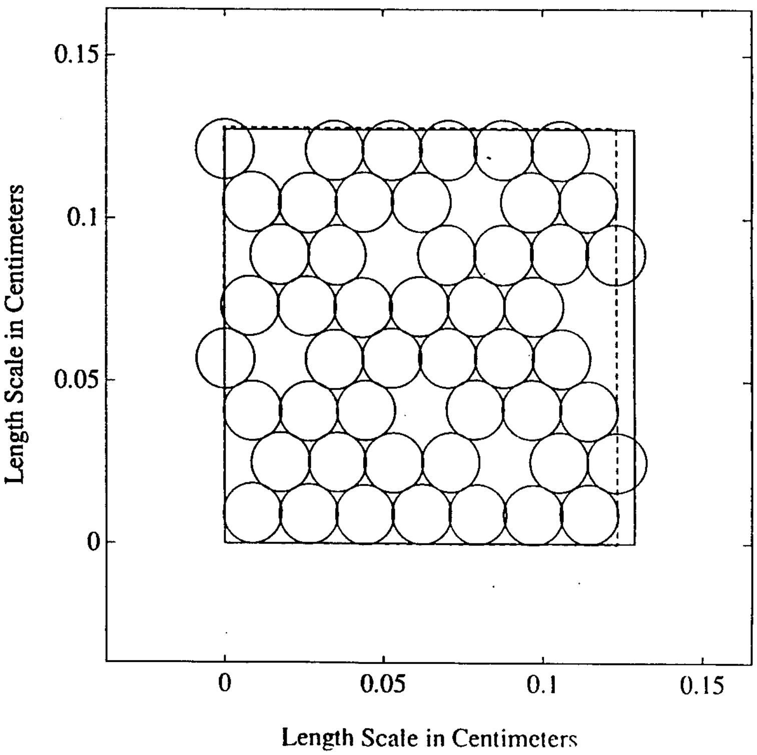

Figure 37. Deformed configuration for the 49-particle control volume. Confining stress = 29.43 N/cm^2; particle radius $r = 0.0092$ cm.

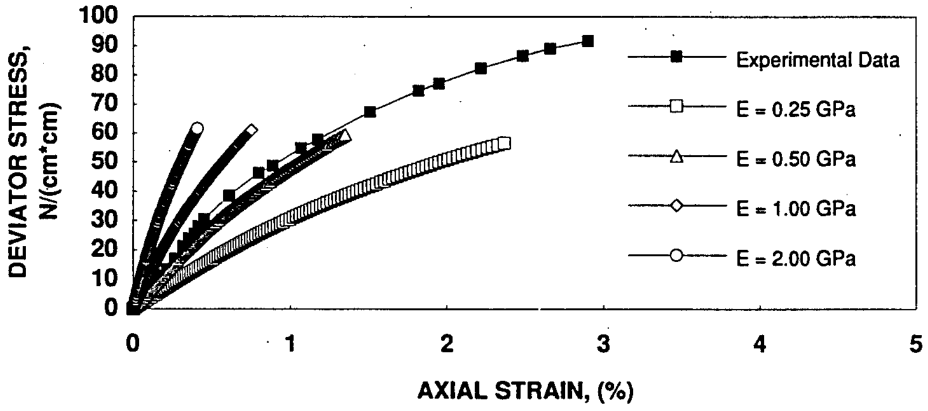

Figure 38. Deviator stress $\Delta\bar{\sigma}^*$ versus axial strain ϵ_1 for the 49-particle control volume at different Young's moduli and Karlsruhe sand. Confining stress = 19.62 N/cm^2.

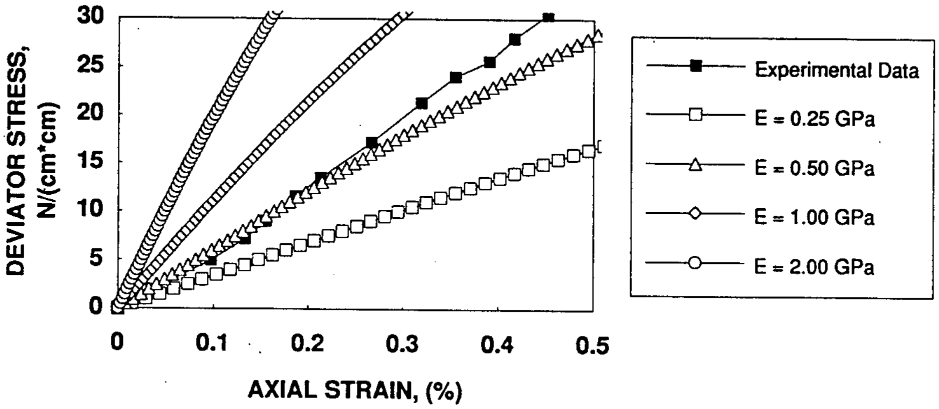

Figure 39. Initial deviator stress $\Delta\bar{\sigma}^*$ versus axial strain ϵ_1 for the 49-particle control volume at different Young's moduli and Karlsruhe sand. Confining stress = 19.62 N/cm^2.

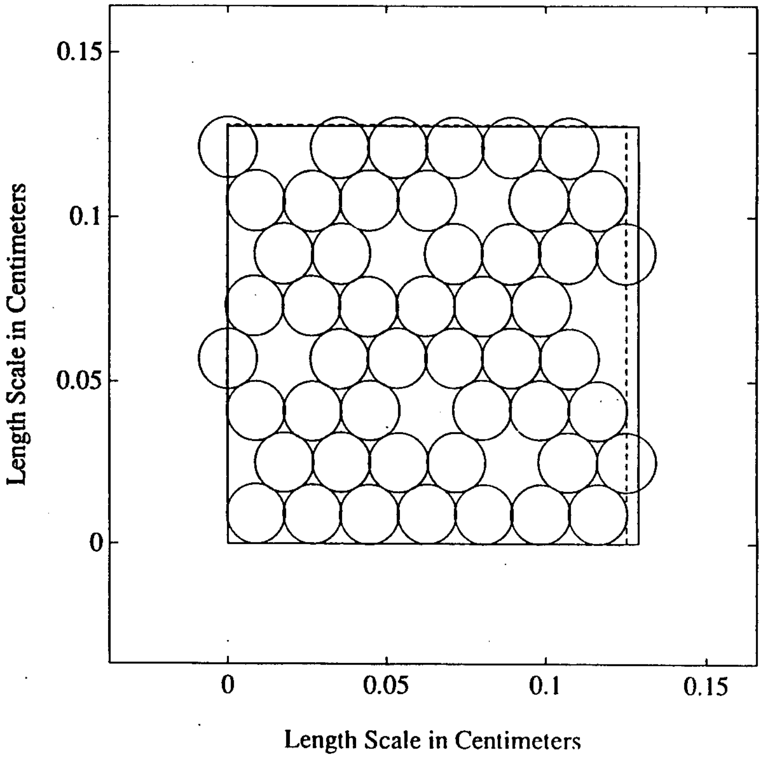

Figure 40. Deformed configuration for the 49-particle control volume. Confining stress = 19.62 N/cm^2; particle radius $r = 0.0092$ cm.

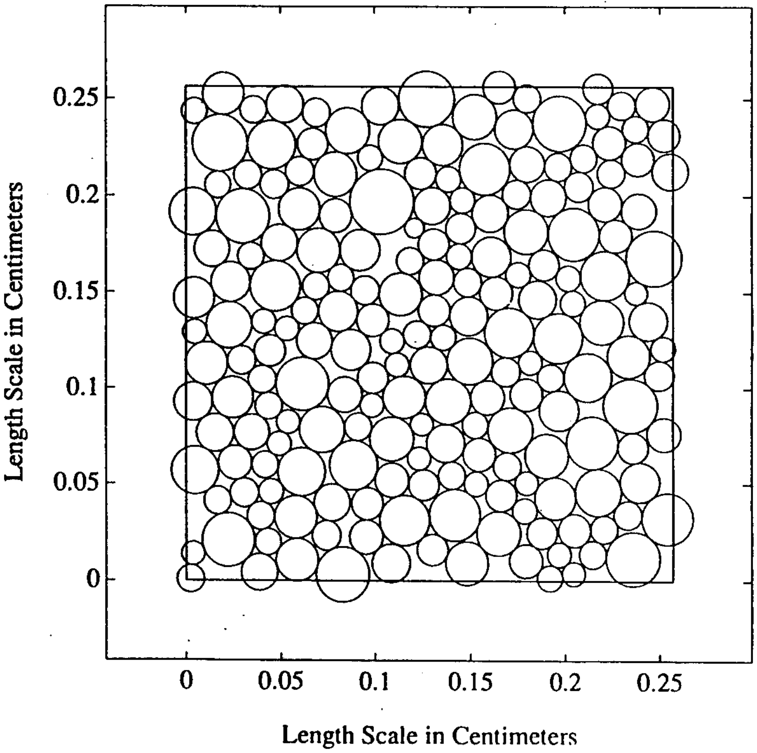
0.25
0.2
0.15
0.1
0.05
0
Length Scale in Centimeters
0
0.05
0.1
0.15
0.2
0.25
Length Scale in Centimeters

Figure 41. Initial configuration for the 196-particle control volume. Coefficient of uniformity $C_u = 1.71$; coefficient of curvature $C_c = 0.90$; mean particle radius = 0.0092 cm.

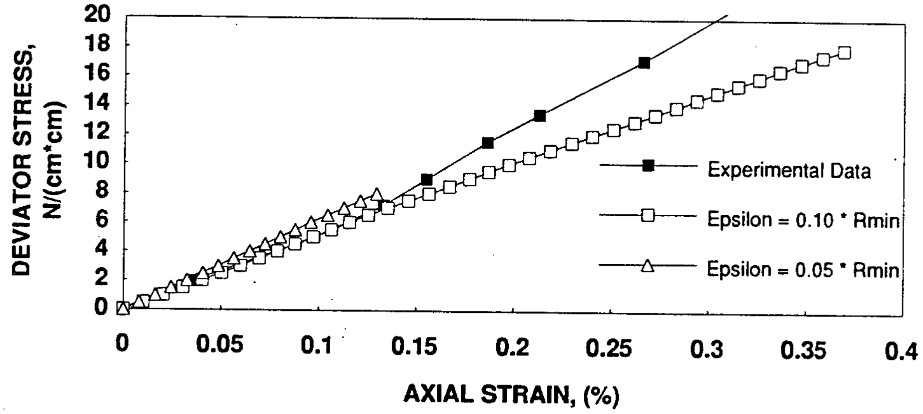

Figure 42. Sensitivity analysis: ramp function ε.

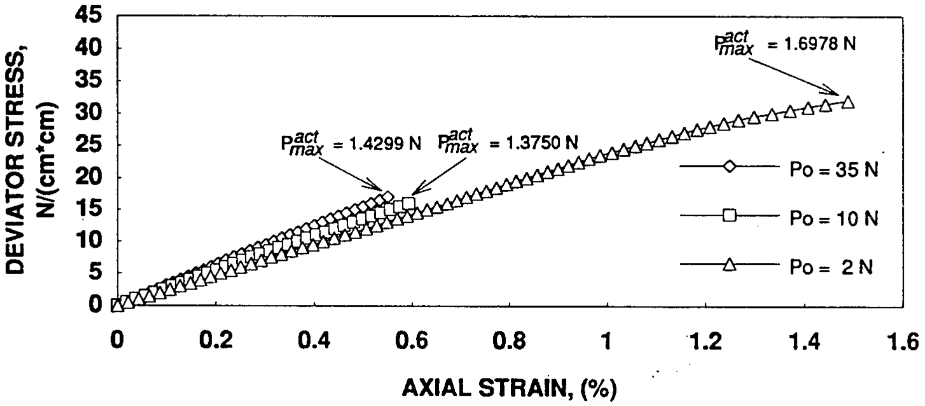

Figure 43. Sensitivity analysis: maximum normal contact force P_{max}.

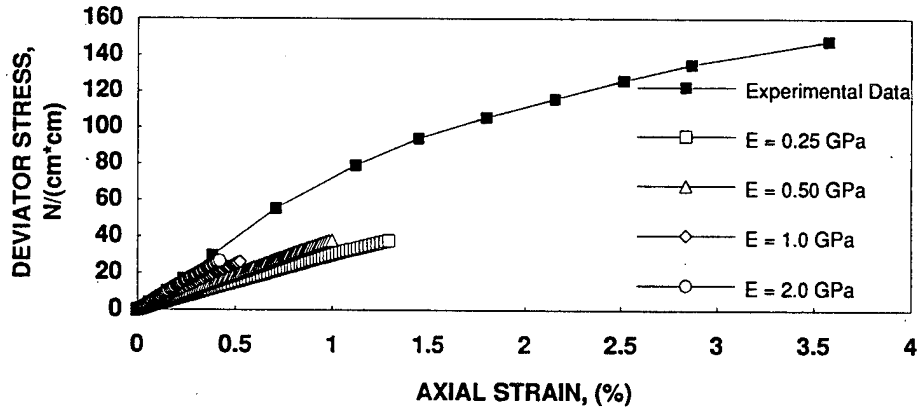

Figure 44. Deviator stress $\Delta\bar{\sigma}^*$ versus axial strain ϵ_1 for the 196-particle control volume at different Young's moduli and Osterchelde sand. Confining stress = 29.43 N/cm^2.

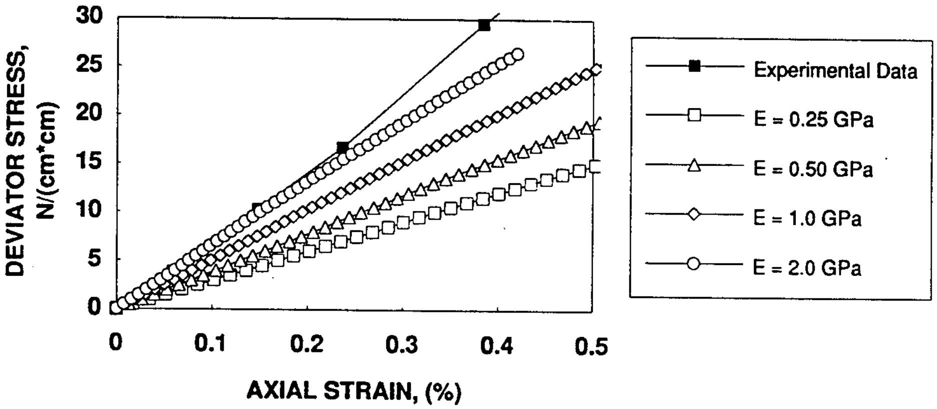

Figure 45. Initial deviator stress $\Delta\bar{\sigma}^*$ versus axial strain ϵ_1 for the 196-particle control volume at different Young's moduli and Osterchelde sand. Confining stress $= 29.43\ \mathrm{N/cm^2}$.

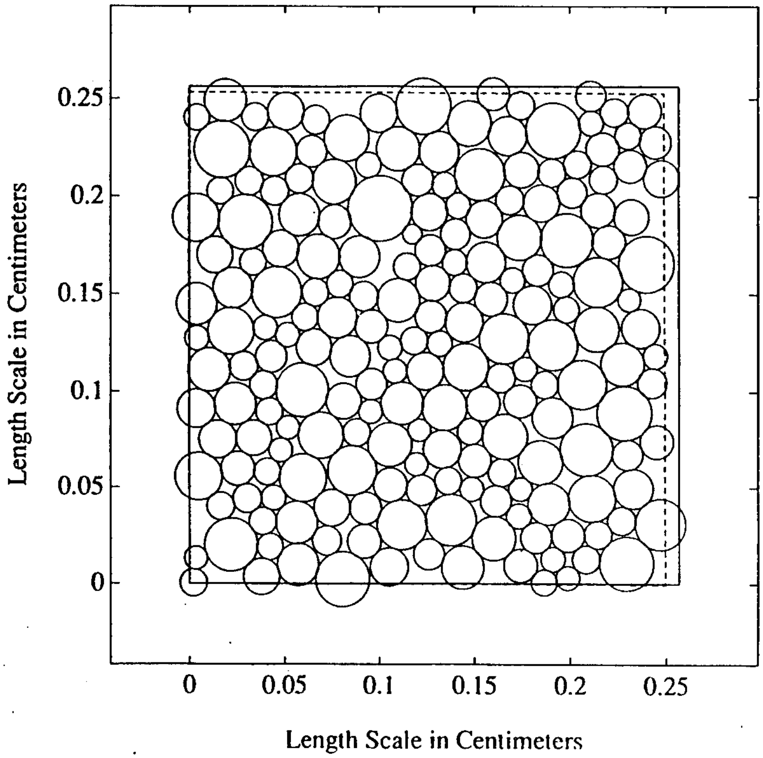

Figure 46. Deformed configuration for the 196-particle control volume. Confining stress = 29.43 N/cm^2.

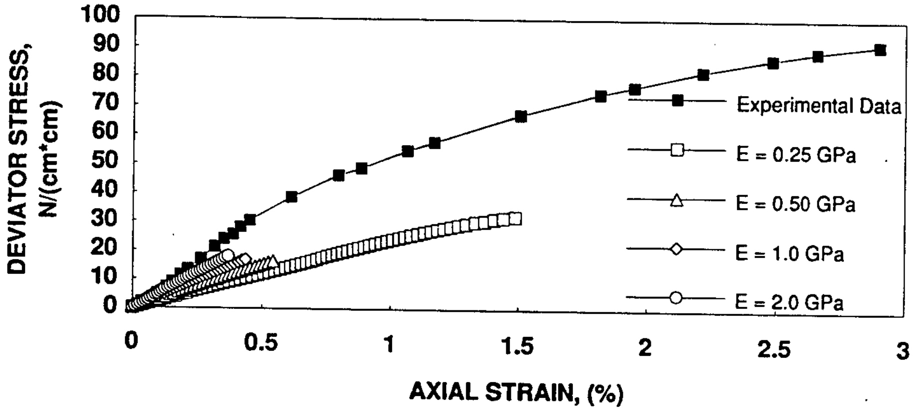

Figure 47. Deviator stress $\Delta\bar{\sigma}^*$ versus axial strain ϵ_1 for the 196-particle control volume at different Young's moduli and Karlsruhe sand. Confining stress = 19.62 N/cm^2.

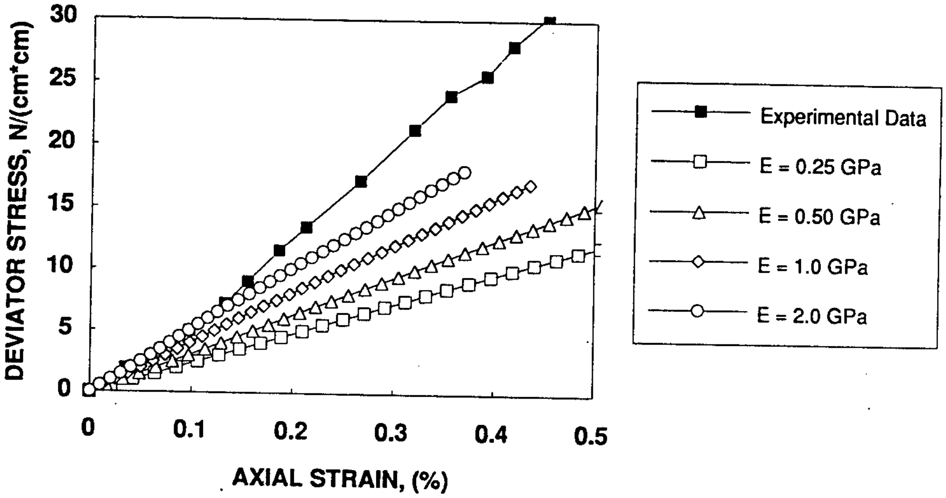

Figure 48. Initial deviator stress $\Delta\bar{\sigma}^*$ versus axial strain ϵ_1 for the 196-particle control volume at different Young's moduli and Karlsruhe sand. Confining stress = 19.62 N/cm^2.

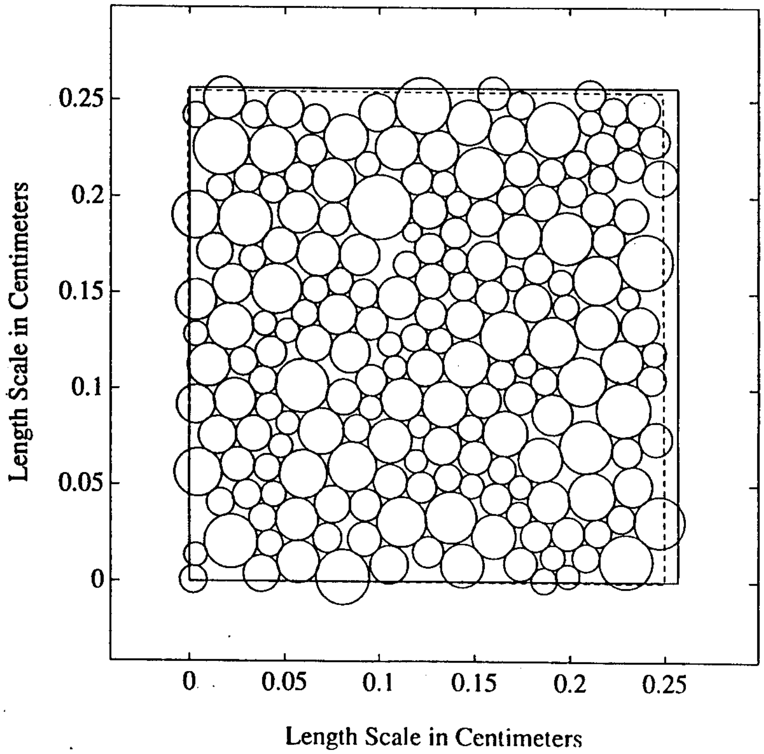
0.25
0.2
0.15
0.1
0.05
0
Length Scale in Centimeters
0
0.05
0.1
0.15
0.2
0.25
Length Scale in Centimeters

Figure 49. Deformed configuration for the 196-particle control volume. Confining stress = 19.62 N/cm^2.

Chapter 7

Fluid Flow Model

7.1. Introduction

Since the dry model discussed in the previous chapters is capable of predicting the volume changes resulting from simple shearing, we can use it to predict the pore pressure changes in fully saturated granular assemblies as a result of changes in the soil's microstructure. In reality, the pore pressures in a saturated granular assembly can vary microscopically in the same random fashion as the particle-to-particle contact stresses because of local variations in the volume of voids between particles. For example, water squirted between particle contacts could be one source of such local variation in the pore water pressure [52]. However, the overall pore pressures on the macroscale level must be consistent with the overall macroscopic motion. In this study, we assume that the pore pressure variable is a macroscopic quantity that is homogeneous throughout the cell of interest. A consequence of this assumption is that the presence of water only serves to impose a macroscopic constraint on the overall volume change of the particle assembly, but does not directly impact the local motion of the individual particles. The following discussion elaborates this latter point.

7.2. Balance Laws

Let $\bar{\boldsymbol{\sigma}}^*$ be the tensor of overall imposed stresses on the granular assembly, $\bar{\boldsymbol{\sigma}}$ be the overall stresses arising from the particle-to-particle contacts, and θ be the homogeneous macroscopic pore pressure in the assembly; then the effective stress equation reads

$$\bar{\boldsymbol{\sigma}}^* = \bar{\boldsymbol{\sigma}} + \theta\,\mathbf{1} \tag{7.1}$$

where $\mathbf{1}$ is the Kronecker delta. Now, let us consider the influence of undrained deformation on the overall deformation represented by the strain tensor $\bar{\boldsymbol{\epsilon}}$. Since $\bar{\boldsymbol{\sigma}} = \bar{\boldsymbol{\sigma}}(\bar{\boldsymbol{\epsilon}})$ and fluid flow is inhibited, then we can use the constitutive equation $\theta = \lambda_w \operatorname{tr}(\bar{\boldsymbol{\epsilon}})/n$, where n is the porosity of the assembly, to obtain

$$\bar{\boldsymbol{\sigma}}^* = \bar{\boldsymbol{\sigma}}(\bar{\boldsymbol{\epsilon}}) + \frac{\lambda_w}{n} \operatorname{tr}(\bar{\boldsymbol{\epsilon}})\,\mathbf{1} \tag{7.2}$$

where λ_w is the bulk modulus of the water phase. Now, if the water phase itself is assumed to be incompressible, then $\lambda_w \gg 1$, which yields $\operatorname{tr}(\bar{\boldsymbol{\epsilon}}) \to 0$, i.e., the deformation becomes macroscopically volume-preserving. Note that this constraint impacts the motion of the particles collectively rather than individually. Thus, the volume constraint due to the presence of water may be viewed either as a factor that alters the overall stress-strain behavior of the granular assembly, or as a driving force that causes a change in the pore water pressure due to the assembly's tendency to change in volume.

An integral equation for balance of momentum can be developed in terms of the overall stress tensor $\bar{\boldsymbol{\sigma}}^*$. Balance of momentum over the entire total domain with volume $\mathcal{U}$ and outer surface $\partial\mathcal{U}$ takes the form

$$\int_{\mathcal{U}} \rho_0 \boldsymbol{G}\, dV + \int_{\partial\mathcal{U}} \bar{\boldsymbol{\sigma}}^* \cdot \boldsymbol{n}\, dA = \mathbf{0} \tag{7.3}$$

where ρ_0 is the reference mass density of the infinitesimal volume element dV, $\boldsymbol{G}$ is the gravity acceleration vector, and $\boldsymbol{n}$ is the outward unit normal to the surface dA. In the context of particulate mechanics, the periodic cell V defined in the previous chapters now takes the meaning of the macroscopic differential volume element dV.

Assuming that both the solid grains and fluids are incompressible, balance of mass for the solid-water mixture takes the form (see [53])

$$\operatorname{div} \boldsymbol{v} + \operatorname{div} \widetilde{\boldsymbol{v}} = 0 \tag{7.4}$$

where $\boldsymbol{v}$ is the macroscopic intrinsic velocity of the solid phase, $\widetilde{\boldsymbol{v}}$ is the macroscopic superficial Darcy velocity, and div is the spatial divergence operator. For undrained condition, $\widetilde{\boldsymbol{v}} = \boldsymbol{0}$ since the solid and fluid phases move as one body. Consequently, this condition gives rise to the constraint $\operatorname{div} \boldsymbol{v} = \operatorname{tr}(\bar{\boldsymbol{\epsilon}}) = 0$, which is precisely recovered from (7.2) when $\lambda_w \gg 1$.

A mathematical formulation casting (7.3) and (7.4) into the framework of a finite element (FE) continuum model is presented in [53]. The standard FE solution methodology entails dividing the domain into smaller finite elements and evaluating the FE matrix counterparts of equations (7.3) and (7.4). The domain integrals are then evaluated numerically by Gauss integration rule to form a FE consolidation model. The numerical formulation of the FE consolidation model is well documented and is beyond the scope of this report (see e.g. [54]). However, the link to particulate mechanics can be established through the macroscopic response of each Gauss integration point, which may be evaluated from the overall response of the particle assembly according to the theory presented earlier in this report. In the following section we shall assume that such link has already been established, and describe a numerical example which illustrates the impact of fluid flow on a continuum material model exhibiting a dilatant behavior.

7.3. Numerical Example

The objective of this numerical example is to study the impact of fluid flow on the deformation behavior of granular assemblies treated as a continuum material. Here, we consider a two-dimensional plane-strain FE mesh shown in Fig. 50. The elements are Q9P4 (9-noded Lagrangian for displacements and 4-node bilinear for pore pressures) in which the material behavior is given by the Drucker-Prager plasticity model with associative flow rule. This material model is phenomenological and not derived from the particulate mechanics theory. However, since the objective of this example is to study the general behavior of the continuum model, such substitution is not critical to the results of the formulation. Ideally, a full numerical analysis would have entailed two levels of modeling, the first being the micromechanical level and the second being the continuum level; however, the computations engendered by this type of analysis are extensive and prohibitively expensive, and so the first level of modeling will be suppressed altogether and will be replaced with a phenomenological constitutive model.

Figure 50 also shows all the boundary conditions and imposed deformation. The elastic material parameters are: Young's modulus $E = 5 \times 10^4$ kPa, and Poisson's ratio $v = 0.1$; regular elements have cohesion $c = 80$ kPa, friction angle $\phi = 35°$, and hardening parameter $H' = 10$ kPa; weak elements are placed on the side of the mesh of Fig. 50 to trigger localized deformation, and are defined by a material having cohesion of $c = 30$ kPa, friction angle of $\phi = 15°$, and hardening parameter of $H' = 0$. All boundary pore water pressures are assumed zero.

Figure 51 shows plots of average normal stress in the x_2-direction ($\bar{\sigma}^*_{22}$) versus the imposed average nominal strain ($\bar{\epsilon}_{22}$), assuming the response to be fully drained (no excess pore water pressure). The deformation is applied in increments of 0.0625 m, or 1.25%, with a final compressed deformation of 20%. The mesh with weak elements substituted at the side begins to yield and reaches a plateau at stresses lower than those attained without weak elements; hence, the stress-strain curve for the mesh with weak elements plots on the lower side relative to the curve for the mesh without weak elements. This phenomenon is a standard result.

Figure 52 shows plots of average normal stress in the x_2-direction ($\bar{\sigma}^*_{22}$) versus the imposed average nominal strain ($\bar{\epsilon}_{22}$) for meshes without weak elements, assuming the responses to be fully drained and fully undrained. For the fully undrained case, consolidation is turned on at the end of the last loading phase, with the total imposed deformation held fixed during this transient period of pore pressure dissipation. Note that the stresses produced in the mesh for the undrained case are greater than those reached for the drained case because the pore water pressure is negative due to a dilating mesh. Consequently, the inclusion of the fluid flow effect "strengthens" the mesh for this case dilating material. Again, this is a standard result.

While the results presented in this chapter are fairly standard, it sheds light onto the possible connection between the micromechanical theory presented in this report and the existing continuum models available for granular materials. In principle, this connection should be clear from the outset as elaborated in this numerical example. The modeling approach presented in this report is not the same as the many particulate mechanics models available in the literature, in which the micro- and the macromechanical aspects of the problem are combined directly to form a single particle assembly that is subjected to a non-homogeneous mode of deformation. The latter approach may have some difficulty tracing the actual effect of material behavior and that of the nonhomogeneous boundary condition. Computationally, the modeling approach presented in this study is amenable to parallel computation, and with the current advances in computational hardware and software modeling tools, the prognosis for a full analysis entailing two levels of modeling is indeed positive.

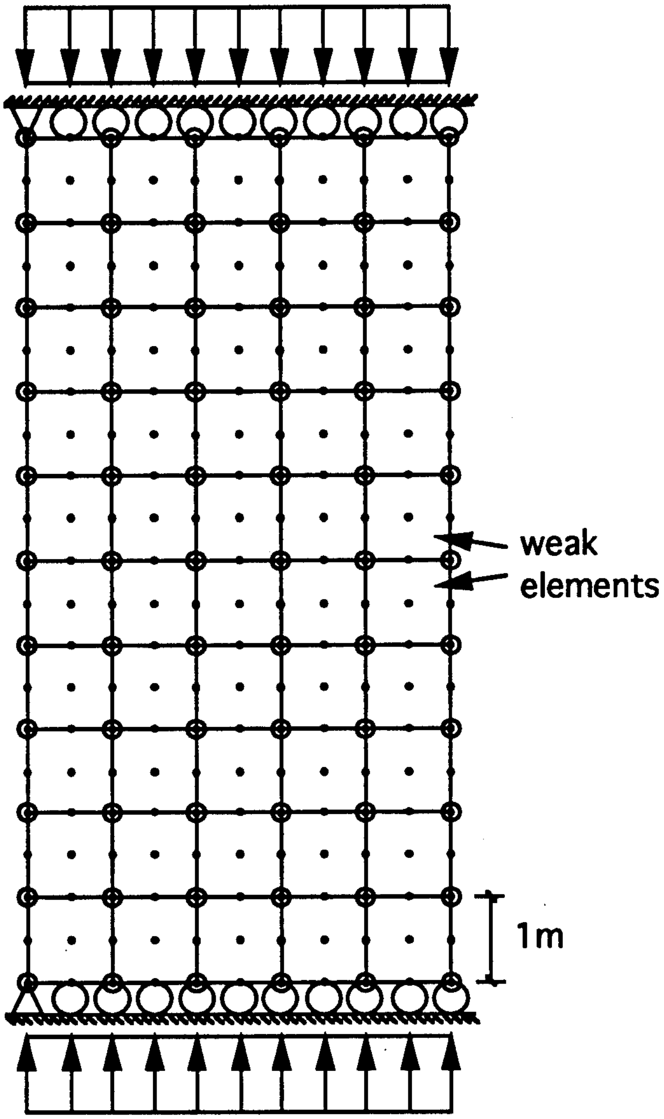
weak
elements
1m

Figure 50. Two-dimensional plane-strain FE mesh

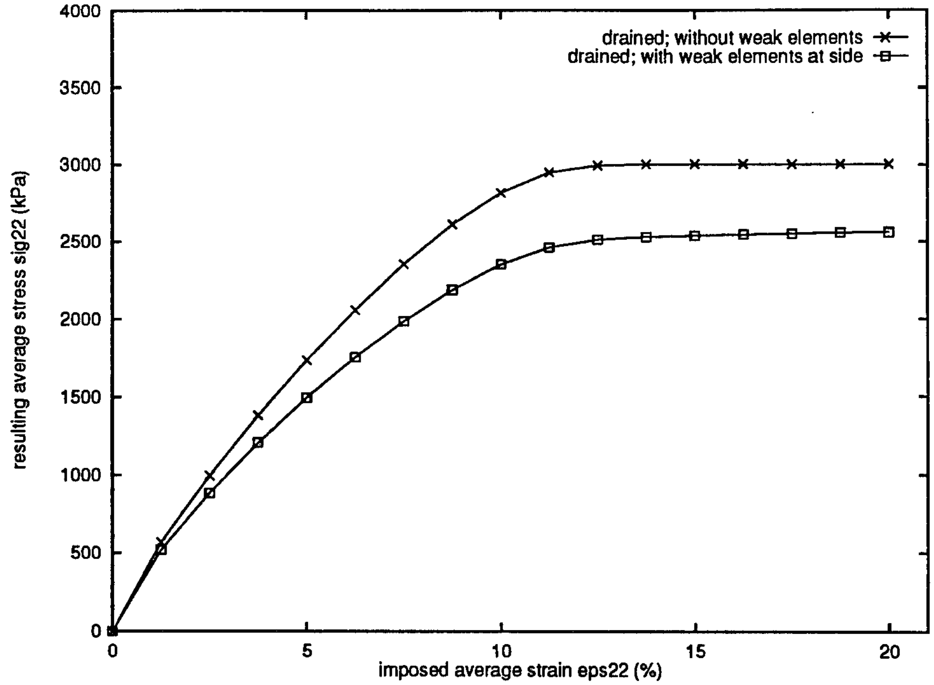

Figure 51. Resulting average stress $\bar{\sigma}^*_{22}$ versus imposed average strain $\bar{\epsilon}_{22}$ demonstrating a lower stress plateau reached when two weak elements are incorporated at side of mesh.

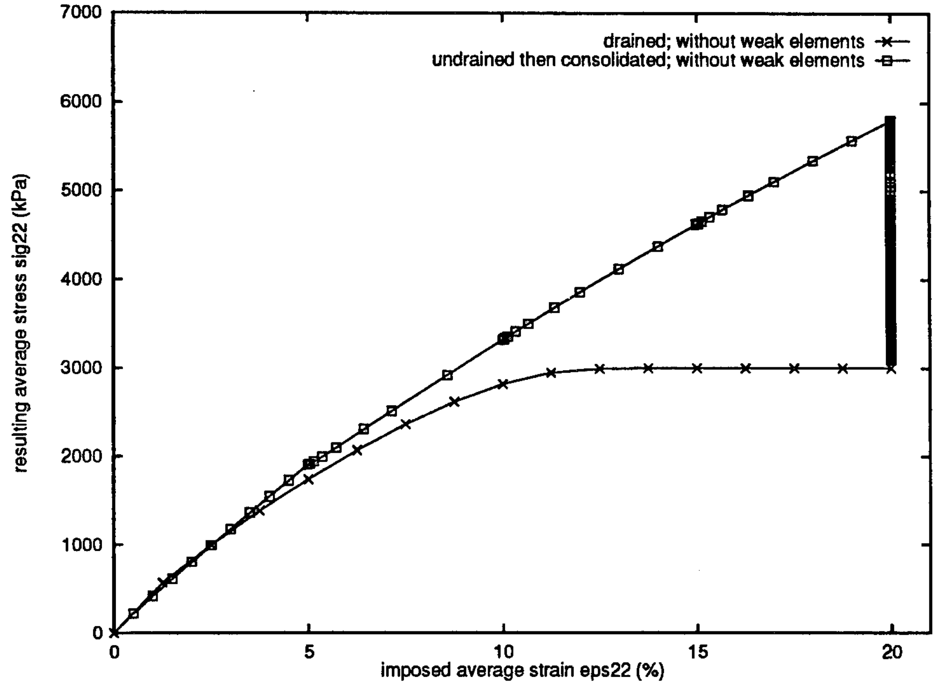

Figure 52. Resulting average stress $\bar{\sigma}^*_{22}$ versus imposed average strain $\bar{\epsilon}_{22}$ demonstrating a "strengthening" effect due to negative pore pressures generated in a dilating material.

Chapter 8

Summary and Conclusions

A methodology has been presented for determining the overall response of a granular material based on the fundamental mechanism of particle-to-particle interaction. The mathematical foundation rests on a particulate mechanics description of the behavior of two contacting particles. With this micromechanical framework, a numerical algorithm solves the problem of a prescribed deformation history for an assembly of particles representing a point in a granular material. To make the overall assembly response independent of the imposed boundary displacements, the formulation employs the notion of a repeating cell. An important feature of the mathematical formulation lies in its generation of the micromechanical responses quasi-statically, and not dynamically. These fundamental features make the model amenable to incorporation into conventional finite element codes.

To assess the performance of the model, two-dimensional plane-strain simulations with regular and random initial packing of circular disks were performed. The model captures some of the most important features of granular material behavior such as anisotropy, hardening, and softening responses. In general, the numerical stability of the solution depends upon the character of the imposed overall motion—convergence of the iteration is easy whenever the shearing is preceded by isotropic compression, but is difficult whenever the imposed motion lacks the isotropic compression needed to keep the microstructure from collapsing.

Interestingly, this characteristic of the numerical model reflects the property of the subject prototype—that the stress response of granular media depends strongly upon the imposed confining load.

In a natural extension of the deformation driven model, a methodology has been developed for determining the overall deformation response of a granular material to an imposed stress history. This formulation allows finite motions of the individual particles, but the macroscopic material response is postulated based on infinitesimal theory. An important by-product of the mathematical formulation is the overall tensor of material moduli derived from the consistent linearization of the elasto-plastic constitutive equation. Owing to the complexity associated with the implementation of the exactly linearized algorithm, an alternative secant approximation has been implemented that retains the essential properties of the exact description. These moduli are then used to predict the onset of localized deformation in granular materials on the macro-scale level. Again, a unique feature of the model is its use of first principles to predict the stability behavior of an assembly of discrete particles.

Numerical simulations with uniform as well as non-uniform assemblies of two-dimensional circular disks demonstrate the model's capability to capture some of the most important features of granular material behavior. The stress-driven format of the numerical algorithm allows the model to capture naturally such mechanical responses as structural anisotropy, pressure dependency, and volume change characteristics of granular materials. Thus, a fundamental understanding of the behavior of particulate materials is available based on the interaction of the constituent particles.

Appendix A. Virtual contact separation

To calculate $\boldsymbol{\Delta}^\alpha$ in equation (3.8) consider two rigid control volume particles A and B in contact at c. Let the virtual displacement field produce a relative displacement at contact c given by

$$\boldsymbol{\Delta}^c = \boldsymbol{u}^{cB} - \boldsymbol{u}^{cA}\,, \tag{A.1}$$

where $\boldsymbol{u}^{cA}$ represents the virtual displacement of c from the perspective of particle A.

Since the particles are assumed rigid, the relative motion of the particle contact can be written in terms of a translation and a rotation. For example, particle A's contact motion can be written as

$$\boldsymbol{u}^{cA} = \boldsymbol{u}^A + \boldsymbol{w}^{Ac} \cdot (\boldsymbol{x}^c - \boldsymbol{x}^A) \tag{A.2}$$

where $\boldsymbol{w}^{Ac} = -\boldsymbol{w}^{cA}$ represents the rotation of contact c relative to A, and $\boldsymbol{u}^A$ denotes the displacement of the centroid of A.

Substituting equation (A.2) and a similar equation for particle B into equation (A.1) gives

$$\boldsymbol{\Delta}^c = \boldsymbol{u}^B - \boldsymbol{u}^A + \boldsymbol{w}^{cA} \cdot (\boldsymbol{x}^c - \boldsymbol{x}^A) - \boldsymbol{w}^{cB} \cdot (\boldsymbol{x}^c - \boldsymbol{x}^B)\,. \tag{A.3}$$

The displacement of the particle centroids can be defined from the series expansion about the common contact point c. Assuming that the displacements $\boldsymbol{u}^B$ and $\boldsymbol{u}^A$ and the rotations $\boldsymbol{w}^{cA}$ and $\boldsymbol{w}^{cB}$ conform to some smooth field $\boldsymbol{u}$ and $\boldsymbol{w}$ and that $\boldsymbol{u}^c = \boldsymbol{u}(\boldsymbol{x}^c)$ represents the value of $\boldsymbol{u}$ at the contact c, the contact rotations become $\boldsymbol{w}^{cA} = \boldsymbol{w}^{cB} = \boldsymbol{w}(\boldsymbol{x}^c)$. The centroid displacements can be written as

$$u_i^A = u^c + \frac{\partial u_i(\boldsymbol{x}^c)}{\partial x_k}(x_k^A - x_k^c) + \ldots \tag{A.4}$$

and

$$u_i^B = u^c + \frac{\partial u_i(\boldsymbol{x}^c)}{\partial x_k}(x_k^B - x_k^c) + \ldots\,. \tag{A.5}$$

Subtracting (A.4) from (A.5) and substituting into (A.3) gives

$$\Delta_i^c = \left[\frac{\partial u_i(\boldsymbol{x}^c)}{\partial x_k} - w_{ik}(\boldsymbol{x}^c)\right] l_k^{AB} + \ldots\,. \tag{A.6}$$

If the tensor $\boldsymbol{\phi}$ is identified as

$$\phi_{ik} = \frac{\partial u_i(\boldsymbol{x}^c)}{\partial x_k} - w_{ik}(\boldsymbol{x}^c)\,, \tag{A.7}$$

then to a first order approximation the virtual separation reads

$$\boldsymbol{\Delta}^c = \boldsymbol{\phi} \cdot \boldsymbol{l}^{AB} \tag{A.8}$$

which is identical to the field equation (3.10) specified for the contact c.

Appendix B. Localization function

For a path-dependent material response, the constitutive equations are integrated incrementally. When the deformation reaches the point where the localization function

$$f(\boldsymbol{n}) = \det[\boldsymbol{A}(\boldsymbol{n})] \tag{B.1}$$

becomes negative or zero, localization is said to have begun. To predict this onset of localization the minima of the function f must be computed at the end of every deformation increment.

In the two-dimensional case, the acoustic tensor $\boldsymbol{A}(\boldsymbol{n})$ takes the following form

$$\boldsymbol{A}(\boldsymbol{n}) = \begin{bmatrix} \begin{array}{c} n_1^2 K_{1111} + n_1 n_2 K_{1112} \\ +n_2 n_1 K_{1211} + n_2^2 K_{1212} \end{array} & \begin{array}{c} n_1^2 K_{1112} + n_1 n_2 K_{1122} \\ +n_2 n_1 K_{1212} + n_2^2 K_{1222} \end{array} \\ & \\ \begin{array}{c} n_1^2 K_{1211} + n_1 n_2 K_{1212} \\ +n_2 n_1 K_{2211} + n_2^2 K_{2212} \end{array} & \begin{array}{c} n_1^2 K_{1212} + n_1 n_2 K_{1222} \\ +n_2 n_1 K_{2212} + n_2^2 K_{2222} \end{array} \end{bmatrix} \tag{B.2}$$

where $n_1 = \cos\theta$ and $n_2 = \sin\theta$, and the angle θ defines the orientation of the discontinuity planes. The localization function yields

$$f(\boldsymbol{n}) = a_0 n_1^4 + a_1 n_1^3 n_2 + a_2 n_1^2 n_2^2 + a_3 n_1 n_2^3 + a_4 n_2^4 \tag{B.3}$$

where

$$\begin{aligned} a_0 &= K_{1111}K_{1212} - K_{1112}K_{1211} \\ a_1 &= K_{1111}K_{1222} + K_{1111}K_{2212} - K_{1112}K_{2211} - K_{1122}K_{1211} \\ a_2 &= K_{1111}K_{2222} + K_{1112}K_{1222} + K_{1211}K_{2212} \\ &\quad - K_{1122}K_{1212} - K_{1122}K_{2211} - K_{1212}K_{2211} \\ a_3 &= K_{1112}K_{2222} + K_{1211}K_{2222} - K_{1122}K_{2212} - K_{1222}K_{2211} \\ a_4 &= K_{1212}K_{2222} - K_{1222}K_{2212} \end{aligned} \tag{B.4}$$

With the change of variables $x = \tan\theta$, equation (B.3) can be written as

$$f(x) = a_4 x^4 + a_3 x^3 + a_2 x^2 + a_1 x + a_0. \tag{B.5}$$

The minima of the function $f(x)$ occur at the roots of the cubic polynomial $f'(x)$ which can be analytically found using Carden's formulae. Positive minima indicate that localization has not yet developed while a negative or zero minimum signals the onset of localization.

Appendix C. Strain-driven problem: tangent operator derivatives

Unless otherwise specified, all quantities in this section have implied subscripts of "$n+1$" for time step and superscripts of 'i' for iteration step.

Taking particle A's point of view, we have the following preliminary results:

$$\boldsymbol{A} := \boldsymbol{n}'(\boldsymbol{d}^A) = -\boldsymbol{n}'(\boldsymbol{d}^B) = -(\boldsymbol{I} - \boldsymbol{n}\boldsymbol{n}^t)/\|\,\boldsymbol{l}\,\|\,; \qquad (C.1)$$

$$\boldsymbol{n}'(\theta^A) = \boldsymbol{n}'(\theta^B) = \boldsymbol{0}\,, \qquad (C.2)$$

where $\boldsymbol{n} = \boldsymbol{n}^A$. Note that $\boldsymbol{A} = \boldsymbol{A}^t$, or $A_{ij} = A_{ji}$. Other necessary derivatives are as follows. For the normal indentation, one has

$$\delta'(\boldsymbol{d}^A) = -\,\delta'(\boldsymbol{d}^B) = \boldsymbol{n}\,; \qquad (C.3)$$

$$\delta'(\theta^A) = \delta'(\theta^B) = 0\,. \qquad (C.4)$$

One can verify that for the incremental slip,

$$\Delta\gamma'(\boldsymbol{d}^A) = -\Delta\gamma'(\boldsymbol{d}^B) = (r^A + r^B)\Delta\theta^{C'}(\boldsymbol{d}^A)\,; \qquad (C.5)$$

$$\Delta\gamma'(\theta^A) = -\,r^A\,; \qquad (C.6)$$

$$\Delta\gamma'(\theta^B) = -\,r^B\,, \qquad (C.7)$$

where

$$\Delta\theta^{C'}(\boldsymbol{d}^A) = (\sec\Delta\theta^C\,\boldsymbol{n}_n \times \boldsymbol{e}_3 + \tan\Delta\theta^C\,\boldsymbol{n})/\|\,\boldsymbol{l}\,\|\,; \qquad (C.8)$$

$$\Delta\theta^C = \sin^{-1}(\boldsymbol{e}_3 \cdot \boldsymbol{n}_n \times \boldsymbol{n})\,. \qquad (C.9)$$

Also, the derivative of the ramp function becomes

$$H'_\varepsilon(\delta) = \begin{cases} 0, & \text{if } \delta_{n+1} > \varepsilon; \\ 1/\varepsilon, & \text{if } 0 < \delta_{n+1} \le \varepsilon; \\ 0, & \text{if } \delta_{n+1} \le 0. \end{cases} \qquad (C.10)$$

Now, assuming that particles A and B are in contact, one finds that

$$f'_N(\boldsymbol{d}^A) = -f'_N(\boldsymbol{d}^B) = -[H'_\varepsilon k_N \delta + H_\varepsilon k_N]\,\delta'(\boldsymbol{d}^A)\,; \qquad (C.11)$$

$$f'_N(\theta^A) = f'_N(\theta^B) = 0\,. \qquad (C.12)$$

If the contact mode is 'stick,' the corresponding derivatives of the tangential force become

$$f'_T(\boldsymbol{d}^A) = -f'_T(\boldsymbol{d}^B) = H'_\varepsilon \, k_T \, \Delta\gamma \, \delta'(\boldsymbol{d}^A) + H_\varepsilon \, k_T \, \Delta\gamma'(\boldsymbol{d}^A) \, , \tag{C.13}$$

$$f'_T(\theta^A) = \left(\frac{r^A}{r^B}\right) f'_T(\theta^B) = -H_\varepsilon k_T r^A \tag{C.14}$$

and if the contact mode is 'slip,' the derivatives of the tangential force are

$$f'_T(\boldsymbol{d}^A) = -f'_T(\boldsymbol{d}^B) \, , \tag{C.15}$$

$$\begin{aligned} f'_T(\boldsymbol{d}^A) = \frac{k_T}{H_\epsilon k_T + H'} \Bigg[H' H_\epsilon \Delta\gamma'(\boldsymbol{d}^A) + \Big[& H'_\epsilon H' (\Delta\gamma - \Delta\gamma^p) \\ & - (\cdot) H_\epsilon k_N \tan\phi (H'_\epsilon \delta_{n+1} + H_\epsilon) \Big] \, \delta'(\boldsymbol{d}^A) \Bigg] \, , \end{aligned} \tag{C.16}$$

$$f'_T(\theta^A) = -\frac{H'_\varepsilon \, H' k_T}{H_\varepsilon k_T + H'} \, r^A \, , \tag{C.17}$$

where $(\cdot) = (f_T)_n + H_\varepsilon k_T \Delta\gamma$.

Constructing the local force gradients, one obtains

$$\mathcal{F}'(\boldsymbol{d}^A) = \begin{bmatrix} f'_N(\boldsymbol{d}^A) \\ f'_T(\boldsymbol{d}^A) \end{bmatrix}_{(2\times 2)} \, ; \tag{C.18}$$

$$\mathcal{F}'(\theta^A) = \begin{Bmatrix} 0 \\ f'_T(\theta^A) \end{Bmatrix}_{(2\times 1)} \, . \tag{C.19}$$

Since $\boldsymbol{f} = \boldsymbol{R} \cdot \mathcal{F}$, the chain rule yields

$$\boldsymbol{f}'(\boldsymbol{d}^A) = -\boldsymbol{f}'(\boldsymbol{d}^B) = \boldsymbol{R} \cdot \mathcal{F}'(\boldsymbol{d}^A) + \boldsymbol{R}'(\boldsymbol{d}^A) \cdot \mathcal{F} \, . \tag{C.20}$$

The last term on the right-hand side of $(C.20)$ has the explicit form

$$\boldsymbol{R}'(\boldsymbol{d}^A) \cdot \mathcal{F} = \begin{bmatrix} (\Lambda_{11} f_N - \Lambda_{12} f_T) & (\Lambda_{12} f_N - \Lambda_{22} f_T) \\ (\Lambda_{12} f_N + \Lambda_{11} f_T) & (\Lambda_{22} f_N + \Lambda_{12} f_T) \end{bmatrix} \tag{C.21}$$

in which the Λ_{ij}'s are given in $(C.1)$. Finally,

$$\boldsymbol{f}'(\theta^A) = \left(\frac{r^A}{r^B}\right) \boldsymbol{f}'(\theta^B) = \boldsymbol{R} \cdot \mathcal{F}'(\theta^A) + \boldsymbol{R}'(\theta^A) \mathcal{F} = f'_T(\theta^A) \, \boldsymbol{n} \times \boldsymbol{e}_3 \, . \tag{C.22}$$

This completes the derivatives necessary to construct the gradient $\boldsymbol{f}^{e\prime}(\boldsymbol{d}^e)$.

Appendix D. Stress-driven problem: tangent operator derivatives

Consider contact element 'e' to represent the contact between particle A and B. Unless otherwise specified, all quantities in this section have implied superscripts of 'k' for iteration step. Taking particle A's point of view to write the force derivatives in (5.46) and (5.47) can be written as

$$\frac{\partial \boldsymbol{f}^{AB}}{\partial \tilde{\boldsymbol{d}}^A} = \begin{bmatrix} \dfrac{\partial \boldsymbol{f}^{AB}(\boldsymbol{d}^A)}{\partial \tilde{\boldsymbol{d}}^A} & \boldsymbol{0} \end{bmatrix}_{(3\times 3)} \tag{D.1}$$

$$\frac{\partial \boldsymbol{f}^{AB}}{\partial \hat{\boldsymbol{d}}^A} = \begin{bmatrix} \dfrac{\partial \boldsymbol{f}^{AB}(\boldsymbol{d}^A)}{\partial \hat{\boldsymbol{d}}^A} & \dfrac{\partial \boldsymbol{f}^{AB}(\theta^A)}{\partial \theta^A} \end{bmatrix}_{(3\times 3)} \tag{D.2}$$

where

$$\boldsymbol{f}^{AB} = \begin{Bmatrix} \boldsymbol{f}^A \\ r^A f_T \end{Bmatrix}_{(3\times 1)} \quad \boldsymbol{d}^A = \begin{Bmatrix} \boldsymbol{d}^A \\ \theta^A \end{Bmatrix}_{(3\times 1)} \tag{D.3}$$

and

$$\tilde{\boldsymbol{d}}^A = \begin{Bmatrix} \tilde{\boldsymbol{d}}^A \\ 0 \end{Bmatrix}_{(3\times 1)} \qquad \hat{\boldsymbol{d}}^A = \begin{Bmatrix} \hat{\boldsymbol{d}}^A \\ \theta^A \end{Bmatrix}_{(3\times 1)} . \tag{D.4}$$

The following preliminary results extend from Appendix C:

$$\boldsymbol{A}_{\tilde{n}} := \frac{\partial \boldsymbol{n}_{\tilde{n}}}{\partial \tilde{\boldsymbol{d}}^A} = -\left(\boldsymbol{I} - \boldsymbol{n}_{\tilde{n}} \boldsymbol{n}_{\tilde{n}}^t\right) / \|\boldsymbol{l}_{\tilde{n}}\| \,, \quad \frac{\partial \boldsymbol{n}_{\tilde{n}}}{\partial \hat{\boldsymbol{d}}^A} = \boldsymbol{0} \,, \quad \frac{\partial \boldsymbol{n}_{\tilde{n}}}{\partial \theta^A} = \boldsymbol{0} \,; \tag{D.5}$$

$$\boldsymbol{A}_{n+1} := \frac{\partial \boldsymbol{n}_{n+1}}{\partial \tilde{\boldsymbol{d}}^A} = \frac{\partial \boldsymbol{n}_{n+1}}{\partial \hat{\boldsymbol{d}}^A} = -\left(\boldsymbol{I} - \boldsymbol{n}_{n+1} \boldsymbol{n}_{n+1}^t\right) / \|\boldsymbol{l}_{n+1}\| \,, \quad \frac{\partial \boldsymbol{n}_{n+1}}{\partial \theta^A} = \boldsymbol{0} \,. \tag{D.6}$$

where $\boldsymbol{n}_{\tilde{n}} = \boldsymbol{n}_{\tilde{n}}^A$ and $\boldsymbol{n}_{n+1} = \boldsymbol{n}_{n+1}^A$. Note that $\boldsymbol{A}_{\tilde{n}} = \boldsymbol{A}_{\tilde{n}}^t$ and $\boldsymbol{A}_{n+1} = \boldsymbol{A}_{n+1}^t$.

Other necessary derivatives are as follows. For the normal indentation, one has

$$\frac{\partial \delta_{n+1}}{\partial \tilde{\boldsymbol{d}}^A} = \frac{\partial \delta_{n+1}}{\partial \hat{\boldsymbol{d}}^A} = \boldsymbol{n}_{n+1} \,, \frac{\partial \delta_{n+1}}{\partial \theta^A} = 0. \tag{D.7}$$

For the incremental slip, one can write

$$\frac{\partial \Delta\gamma}{\partial \tilde{\boldsymbol{d}}^A} = \frac{\partial \Delta\gamma_{\tilde{\boldsymbol{n}}}}{\partial \tilde{\boldsymbol{d}}^A} + \frac{\partial \Delta\gamma_{\hat{\boldsymbol{n}}}}{\partial \tilde{\boldsymbol{d}}^A} \,, \tag{D.8}$$

and

$$\frac{\partial \Delta\gamma}{\partial \hat{\boldsymbol{d}}^A} = \frac{\partial \Delta\gamma_{\tilde{\boldsymbol{n}}}}{\partial \hat{\boldsymbol{d}}^A} + \frac{\partial \Delta\gamma_{\hat{\boldsymbol{n}}}}{\partial \hat{\boldsymbol{d}}^A} \,, \tag{D.9}$$

where

$$\frac{\partial \Delta\gamma_{\tilde{n}}}{\partial \tilde{\boldsymbol{d}}^A} = \left(r^A + r^B\right) \frac{\partial \Delta\theta^C_{\tilde{n}}}{\partial \tilde{\boldsymbol{d}}^A}\,, \tag{D.10}$$

$$= \left(r^A + r^B\right) \left[\sec \Delta\theta^C_{\tilde{n}}\ \boldsymbol{n}_n \times \mathbf{e}_3 + \tan \Delta\theta^C_{\tilde{n}}\ \boldsymbol{n}_{\tilde{n}}\right] / \|\boldsymbol{l}_{\tilde{n}}\|\,, \tag{D.11}$$

$$\frac{\partial \Delta\gamma_{\tilde{n}}}{\partial \hat{\boldsymbol{d}}^A} = \mathbf{0}\,, \tag{D.12}$$

and

$$\frac{\partial \Delta\gamma_{\hat{n}}}{\partial \tilde{\boldsymbol{d}}^A} = \left(r^A + r^B\right) \frac{\partial \Delta\theta^C_{\hat{n}}}{\partial \tilde{\boldsymbol{d}}^A}\,, \tag{D.13}$$

$$\begin{aligned} &= \left(r^A + r^B\right) \left[\sec \Delta\theta^C_{\hat{n}}\ \mathbf{e}_3 \times \boldsymbol{n}_{n+1} + \tan \Delta\theta^C_{\hat{n}}\ \boldsymbol{n}_{\tilde{n}}\right] / \|\boldsymbol{l}_{\tilde{n}}\| \\ &\quad + \left(r^A + r^B\right) \left[\sec \Delta\theta^C_{\hat{n}}\ \boldsymbol{n}_{\tilde{n}} \times \mathbf{e}_3 + \tan \Delta\theta^C_{\hat{n}}\ \boldsymbol{n}_{n+1}\right] / \|\boldsymbol{l}_{n+1}\|\,, \end{aligned} \tag{D.14}$$

$$\frac{\partial \Delta\gamma_{\hat{n}}}{\partial \hat{\boldsymbol{d}}^A} = \left(r^A + r^B\right) \frac{\partial \Delta\theta^C_{\hat{n}}}{\partial \hat{\boldsymbol{d}}^A}\,, \tag{D.15}$$

$$= \left(r^A + r^B\right) \left[\sec \Delta\theta^C_{\hat{n}}\ \boldsymbol{n}_{\tilde{n}} \times \mathbf{e}_3 + \tan \Delta\theta^C_{\hat{n}}\ \boldsymbol{n}_{n+1}\right] / \|\boldsymbol{l}_{n+1}\|\,. \tag{D.16}$$

Similarly, considering the rotation effects gives

$$\frac{\partial \Delta\gamma}{\partial \theta^A} = \frac{\partial \Delta\gamma_{\tilde{n}}}{\partial \theta^A} + \frac{\partial \Delta\gamma_{\hat{n}}}{\partial \theta^A}\,, \tag{D.17}$$

where

$$\frac{\partial \Delta\gamma_{\tilde{n}}}{\partial \theta^A} = 0\,, \tag{D.18}$$

$$\frac{\partial \Delta\gamma_{\hat{n}}}{\partial \theta^A} = -r^A\,. \tag{D.19}$$

The derivative of the ramp function becomes

$$H'_\epsilon(\delta) = \begin{cases} 0, & \text{if } \delta_{n+1} > \epsilon\,; \\ 1/\epsilon, & \text{if } 0 < \delta_{n+1} \le \epsilon\,; \\ 0, & \text{if } \delta_{n+1} \le 0\,. \end{cases} \tag{D.20}$$

Now, the derivatives of the normal force can be written as

$$\frac{\partial f_N}{\partial \tilde{\boldsymbol{d}}^A} = \frac{\partial f_N}{\partial \hat{\boldsymbol{d}}^A} = -\left[H'_\epsilon k_N \delta_{n+1} + H_\epsilon k_N\right] \boldsymbol{n}_{n+1}\,, \tag{D.21}$$

$$\frac{\partial f_N}{\partial \theta^A} = 0. \tag{D.22}$$

If the contact mode is 'stick,' the corresponding derivatives of the tangential force become

$$\frac{\partial f_T}{\partial \tilde{\boldsymbol{d}}^A} = H'_\epsilon k_T \Delta\gamma \frac{\partial \delta_{n+1}}{\partial \tilde{\boldsymbol{d}}^A} + H_\epsilon k_T \frac{\partial \Delta\gamma}{\partial \tilde{\boldsymbol{d}}^A}\,, \tag{D.23}$$

$$\frac{\partial f_T}{\partial \hat{\boldsymbol{d}}^A} = H'_\epsilon k_T \Delta\gamma \frac{\partial \delta_{n+1}}{\partial \hat{\boldsymbol{d}}^A} + H_\epsilon k_T \frac{\partial \Delta\gamma}{\partial \hat{\boldsymbol{d}}^A}\,, \tag{D.24}$$

$$\frac{\partial f_T}{\partial \theta^A} = -r^A H_\epsilon k_T. \tag{D.25}$$

If the contact mode is 'slip,' the derivatives of the tangential force are

$$\begin{aligned}\frac{\partial f_T}{\partial \tilde{\boldsymbol{d}}^A} = \frac{1}{H_\epsilon k_T + H'}\Bigg[&\Big[H'_\epsilon k_T H'(\Delta\gamma - \Delta\gamma^p) \\ &- (\cdot) H_\epsilon k_T k_N \tan\phi (H'_\epsilon \delta_{n+1} + H_\epsilon)\Big] \frac{\partial \delta_{n+1}}{\partial \tilde{\boldsymbol{d}}^A} \\ &+ H' H_\epsilon k_T \frac{\partial \Delta\gamma}{\partial \tilde{\boldsymbol{d}}^A}\Bigg]\,,\end{aligned} \tag{D.26}$$

$$\begin{aligned}\frac{\partial f_T}{\partial \hat{\boldsymbol{d}}^A} = \frac{1}{H_\epsilon k_T + H'}\Bigg[&\Big[H'_\epsilon k_T H'(\Delta\gamma - \Delta\gamma^p) \\ &- (\cdot) H_\epsilon k_T k_N \tan\phi (H'_\epsilon \delta_{n+1} + H_\epsilon)\Big] \frac{\partial \delta_{n+1}}{\partial \hat{\boldsymbol{d}}^A} \\ &+ H' H_\epsilon k_T \frac{\partial \Delta\gamma}{\partial \hat{\boldsymbol{d}}^A}\Bigg]\,,\end{aligned} \tag{D.27}$$

where $(\cdot) = (f_T)_n + H_\epsilon k_T \Delta\gamma$.

Since $\boldsymbol{f} = \boldsymbol{R} \cdot \mathcal{F}$, the chain rule yields

$$\frac{\partial \boldsymbol{f}}{\partial \tilde{\boldsymbol{d}}^A} = \boldsymbol{R} \cdot \frac{\partial \mathcal{F}}{\partial \tilde{\boldsymbol{d}}^A} + \frac{\partial \boldsymbol{R}(\boldsymbol{d}^A)}{\partial \tilde{\boldsymbol{d}}^A} \cdot \mathcal{F}\,, \tag{D.28}$$

$$\frac{\partial \boldsymbol{f}}{\partial \hat{\boldsymbol{d}}^A} = \boldsymbol{R} \cdot \frac{\partial \mathcal{F}}{\partial \hat{\boldsymbol{d}}^A} + \frac{\partial \boldsymbol{R}(\boldsymbol{d}^A)}{\partial \hat{\boldsymbol{d}}^A} \cdot \mathcal{F}\,, \tag{D.29}$$

where

$$\frac{\partial \mathcal{F}}{\partial \tilde{\boldsymbol{d}}^A} = \left[\frac{\partial f_N}{\partial \tilde{\boldsymbol{d}}^A}\,;\quad \frac{\partial f_T}{\partial \tilde{\boldsymbol{d}}^A}\right]^t_{(2\times 2)}\,, \tag{D.30}$$

$$\frac{\partial \mathcal{F}}{\partial \hat{\boldsymbol{d}}^A} = \left[\frac{\partial f_N}{\partial \hat{\boldsymbol{d}}^A}\,;\quad \frac{\partial f_T}{\partial \hat{\boldsymbol{d}}^A}\right]^t_{(2\times 2)}\,. \tag{D.31}$$

The last term on the right-hand side of $(D.28)$ and $(D.29)$ has the explicit form

$$\frac{\partial \boldsymbol{R}(\boldsymbol{d}^A)}{\partial \tilde{\boldsymbol{d}}^A} = \frac{\partial \boldsymbol{R}(\boldsymbol{d}^A)}{\partial \hat{\boldsymbol{d}}^A} = \begin{bmatrix} (\Lambda_{11} f_N - \Lambda_{12} f_T) & (\Lambda_{12} f_N - \Lambda_{22} f_T) \\ (\Lambda_{12} f_N + \Lambda_{11} f_T) & (\Lambda_{22} f_N + \Lambda_{12} f_T) \end{bmatrix} \tag{D.32}$$

in which the Λ_{ij}'s are given in $(D.6)$. Finally,

$$\frac{\partial \boldsymbol{f}}{\partial \theta^A} = \boldsymbol{R} \cdot \frac{\partial \mathcal{F}}{\partial \theta^A} + \frac{\partial \boldsymbol{R}(\boldsymbol{d}^A)}{\partial \theta^A} \cdot \mathcal{F} = \frac{\partial \mathcal{F}}{\partial \theta^A} \boldsymbol{n}_{n+1} \times \boldsymbol{e}_3 \, . \tag{D.33}$$

This completes the derivatives necessary to construct the algorithmic tangent operator.

References

[1] M. Oda, Initial fabrics and their relations to mechanical properties of granular material, Japanese Society of Soil Mechanics and Foundation Engineering: Soils and Foundations 12 (1972) 17–36.

[2] M. Oda, The mechanism of fabric changes during compressional deformation of sand, Japanese Society of Soil Mechanics and Foundation Engineering: Soils and Foundations 12 (1972) 1–18.

[3] M. Oda, Deformation mechanism of sand in triaxial compression tests, Japanese Society of Soil Mechanics and Foundation Engineering: Soils and Foundations 12 (1972) 45–63.

[4] A. Drescher and De Josselin De Jong, Photoelastic verification of a material model for the flow of a granular material, J. Mech. and Physics of Solids 20 (1972) 337–351.

[5] M. Oda and J. Konishi, Microscopic deformation mechanism of granular material in simple shear, Japanese Society of Soil Mechanics and Foundation Engineering: Soils and Foundations 14 (1974) 25–38.

[6] M. Oda, J. Konishi, and S. Nemat–Nasser, Experimental micromechanical evaluation of strength of granular materials, Mech. of Materials 1 (1982) 269–283.

[7] H. Deresiewicz, Mechanics of granular material, Advd. Appl. Mech. 5 (1958) 233–306.

[8] C. Thorton, The conditions of failure of a face–centered cubic array of uniform rigid spheres, Géotechnique 29 (1979) 441–459.

[9] A.A. Serano and J.M. Rodriguez–Ortiz, A contribution to the mechanics of heterogeneous granular media, in: A.C. Palmer, ed., Proceedings of the Symposium on the Role of Plasticity in Soil Mechanics (Cambridge, 1973) 215–228.

[10] J.M. Rodriguez–Ortiz, Estudio del comportamiento de medios granulares heterogéos medianto modelos discontinuos analógicos y matemáticos, PhD thesis, Universidad Politećnica de Madrid, 1974.

[11] R.D. Mindlin, Compliance of elastic bodies in contact, J. Appl. Mech. 71 (1949) 259–268.

[12] R.D. Mindlin and H. Deresiewicz, Elastic spheres in contact under varying oblique forces, J. Appl. Mech. 20 (1953) 327–344.

[13] P.A. Cundall and O.D.L. Strack, A discrete numerical model for granular assemblies, Géotechnique 29 (1979) 47–65.

[14] O.R. Walton and R.L. Braun, Viscosity, granular–temperature, and stress calculations for shearing assemblies of inelastic, frictional disks, J. Rheology 30 (1986) 949–980.

[15] O.R. Walton and R.L. Braun, Stress calculations for assemblies of inelastic spheres in uniform shear, Acta Mechanica 63 (1986) 73–86.

[16] C. Thorton and C.W. Randall, Applications of theoretical contact mechanics to solid particle system simulation, in: M. Satake and J.T. Jenkins, eds., Micromechanics of Granular Materials (Elsevier Science Publishers, Amsterdam, 1988) 133–142.

[17] L. Rothenburg and R.J. Bathurst, Micromechanical features of granular assemblies with planar elliptical particles, Géotechnique 42 (1992) 79–95.

[18] T.T. Ng, A non–linear numerical model for soil mechanics, Int. J. Num. Meth. and Anal. Meth. in Geomech. 16 (1992) 247–263.

[19] Y. Kishino, Disc model analysis of granular media, in: M. Satake and J.T. Jenkins, eds., Micromechanics of Granular Materials (Elsevier Science Publishers, Amsterdam, 1988) 133–142.

[20] J.P. Bardet and J. Proubet, Adaptive dynamic relaxation for statics of granular materials, Comput. and Structs 39 (1991) 221–229.

[21] J.P. Bardet and J. Proubet, A numerical investigation of the structure of persistent shear bands in granular media, Géotechnique 41 (1991) 599–613.

[22] J.P. Bardet and J. Proubet, Shear–band analysis in idealized granular material, ASCE J. Engrg. Mech. 118 (1992) 397–415.

[23] S. Nemat-Nasser and M.M. Mehrabadi, Micromechanically based rate constitutive descriptions for granular materials, in: C.S. Desai and R.H. Gallagher, eds. Mechanics of Engineering Materials (John Wiley and Sons, New York, 1984) 451–463.

[24] R. Hill, Continuum micro–mechanics of elastoplastic polycrystals, J. Mech. Physics Solids 13 (1965) 89–101.

[25] R. Hill, The essential structure of constitutive laws for metal composites and polycrystals, J. Mech. Physics Solids 15 (1967) 79–95.

[26] C.S. Chang, A. Misra, and K. Acheampong, Elastoplastic deformation for particulates with frictional contacts, ASCE J. Engrg. Mech. 118 (1992) 1692–1707.

[27] C.S. Chang, Y. Chang, and M.G. Kabir, Micromechanical modeling for stress–strain behavior of granular soils. I: Theory, ASCE J. Geotech. Engrg. 118 (1992) 1959–1974.

[28] C.S. Chang, M.G. Kabir, and Y. Chang, Micromechanical modeling for stress–strain behavior of granular soils. I: Evaluation, ASCE J. Geotech. Engrg. 118 (1992) 1975–1992.

[29] J. Christoffersen, M.M. Mehrabadi, and S. Nemat–Nasser, A micromechanical description of granular material behavior, J. Appl. Mech. 48 (1981) 339–344.

[30] J.R. Rice, The localization of plastic deformation, in: W.T. Koiter, eds. Theoretical and Applied Mechanics, Proc. of the 14th IUTAM Congress (North Holland, New York, 1976) 207–220.

[31] J.W. Rudnicki and J.R. Rice, Conditions for the localization of deformation in pressure–sensitive dilatant materials, J. Mech. Phys. Solids 23 (1975) 371–394.

[32] R.I. Borja and J.R. Wren, Discrete micromechanics of elastoplastic crystals, Internat. J. Numer. Meths. Engrg. 36 (1993) 3815–3840.

[33] J.E. Dennis, JR and J.J. Moré, Quasi-Newton methods, motivation and theory, SIAM Review 19 (1977) 46–89.

[34] J.M. Ortega and W.C. Rheinboldt, Iterative Solution of Nonlinear Equations in Several Variables (Academic Press, San Diego, 1970).

[35] R.I. Borja, Composite Newton-PCG and quasi-Newton iterations for nonlinear consolidation, Comput. Methods Appl. Mech. Engrg. 86 (1991) 27–60.

[36] M.R. Kuhn, Micromechanical aspects of soil creep, Ph.D. thesis, University of California, Berkeley, CA (1987).

[37] J. C. Simo and R. L. Taylor, Consistent tangent operators for rate-independent elastoplasticity, Comput. Methods Appl. Mech. Engrg. 48 (1985) 101–118.

[38] S. Nemat-Nasser, Overall stresses and strains in solids with microstructure, in: J. Gittus and J. Zarka, eds. Modelling Small Deformations of Polycrystals (Elsevier, New York, 1986) 41–64.

[39] R. D. Mindlin, Compliance of elastic bodies in contact, J. Applied Mechanics, Trans. ASME 71 (1949) 259–268.

[40] H. Poritsky, Stresses and deflections of cylindrical bodies in contact with application to contact of gears and locomotive wheels, J. Applied Mechanics, Trans. ASME 17 (1950) 191–201.

[41] K. L. Johnson, Contact Mechanics (Cambridge University Press, New York, 1985).

[42] L. Barden, H. Ismail, and P. Tong, Plane strain deformation of granular material at low and high pressures, Géotechnique 19 (1969) 441–452.

[43] J. Desrues, J. Lanier, and P. Stutz, Localization of the deformation in tests on sand sample, Engineering Fracture Mechanics 21 (1985) 909–921.

[44] C. Han and A. Drescher, Shear bands in biaxial tests on dry coarse sand, Soils and Foundations 33 (1993) 118–132.

[45] L. V. Medeiros and E. Evgin, Influence of stress paths on strength and deformation characteristics of sand, in: O. A. Ayorinde, N. K. Sinha, D. S. Sodhi, and W. A. Nixon, eds. Proceedings of the 11th International Conference on Offshore Mechanics and Artic Engineering (American Society of Mechanical Engineers, New York, 1992) 401–408.

[46] F. Tatsuoka, S. Nakamura, C. Huang, and K. Tani, Strength anisotropy and shear band direction in plane strain tests on sand, Soils and Foundations 30 (1990) 35–54.

[47] F. Tatsuoka, M. Sakamoto, T. Kawamura, and S. Fukushima, Strength and deformation characteristics of sand in plane strain compression at extremely low pressures, Soils and Foundations 26 (1986) 65–84.

[48] I. Vardoulakis, Theoretical and experimental bounds for shear-band bifurcation strain in biaxial tests on dry sand, Res Mechanica 23 (1988) 239–259.

[49] I. Vardoulakis and B. Graf, Calibration of constitutive models for granular materials using data from biaxial experiments, Géotechnique 35 299–317.

[50] I. Vardoulakis and M. Goldsheider, Biaxial apparatus for testing shear bands in soils, in: Soil Mechanics and Foundation Engineering Tenth International Conference, Volume 1 (A. A. Balkema, Rotterdam, 1981) 819–824.

[51] Y. S. Touloukian and C. Y. Ho, Physical Properties of Rocks and Minerals, Volume II-2 (McGraw-Hill, San Francisco, 1981).

[52] J. Dvorkin and A. Nur, Dynamic poro-elasticity: a unified theory with the squirt and the Biot mechanisms, Geophysics, in press.

[53] R.I. Borja and E. Alarcón, E., A mathematical framework for finite strain

elasto-plastic consolidation, Part 1: Balance laws, variational formulation, and linearization, Comput. Methods Appl. Mech. Engrg. 122 (1995) 145–171.

[54] R.I. Borja, One-step and linear multistep methods for nonlinear consolidation, Comput. Methods Appl. Mech. Engrg., 85 (1991) 239–272.

Computer Code for Micromechanical and Macromechanical Model

```
C==============================================================
C     PROGRAM MACRO
C==============================================================
C
C.... MAIN PROGRAM
C
      IMPLICIT REAL*8(A-H,O-Z)
C
C.... REMOVE ABOVE CARD FOR SINGLE PRECISION OPERATION
C
      DIMENSION IDIAG(5000)
      DIMENSION AUPPER(200000),ALOWER(200000),B(3000)
      DIMENSION XA(2),XB(2),XL0(2)
      COMMON /MACRO / FSIG(3),SIG(3),EP(3)
      COMMON /PARTCL/ X(3,1000),NPART,RMIN
      COMMON /INFO  / IEN(2,20000),ID(3,1000),LM(6,20000),
     X                NUMEL,NEQ,NSTIFF
      COMMON /DSDATA/ D(3,1000),DD(3,1000),DINC(3,1000),
     X                DDINC(3,1000)
      COMMON /FDATA / FTN(20000),ALPHA(20000),ICON(20000)
      COMMON /ELDATA/ SKN,SKT,A,TANPHI,HP
      DATA ZERO,ONE/0.0D0,1.0D0/
C
      OPEN(UNIT=12,FILE='out1',STATUS='UNKNOWN')
      OPEN(UNIT=24,FILE='out2',STATUS='UNKNOWN')
      OPEN(UNIT=36,FILE='out3',STATUS='UNKNOWN')
      OPEN(UNIT=48,FILE='out4',STATUS='UNKNOWN')
      OPEN(UNIT=60,FILE='out5',STATUS='UNKNOWN')
      OPEN(UNIT=51,FILE='input',STATUS='UNKNOWN')
C
C.... INPUT CONTROL DATA.
C     THE INPUT FILE 'input' TAKES THE FOLLOWING FORM:
C
C     NPART,XCELL,YCELL,SKN,SKT,A,PHI,HP
C     X(1),Y(1),RADIUS(1)
C     :
C     :
C     :
C     :
C     X(NPART),Y(NPART),RADIUS(NPART)
C
C     WHERE:
C     NPART=NUMBER OF PARTICLES IN THE CONTROL VOLUME
C     XCELL=X DIMENSION OF THE CONTROL VOLUME.
C     YCELL=Y DIMENSION OF THE CONTROL VOLUME.
C     SKN=NORMAL SPRING STIFFNESS.
C     SKT=TANGENTIAL SPRING STIFFNESS.
C     A=PARTICLE COHESION.
```

```
C     PHI=PARTICLE FRICTION ANGLE.
C     HP=HARDENING PARAMETER.
C     TANPHI=TAN(PHI).
C     RADIUS(N)=RADIUS OF PARTICLE N.
C     X(N)=X COORDINATE OF THE PARTICLE N'S CENTROID.
C     Y(N)=Y COORDINATE OF THE PARTICLE N'S CENTROID.
C
C     THIS DATA IS READ INTO THE ARRAY X WHERE EACH ELEMENT HAS
C     THE FOLLOWING MEANING:
C
C     X(1,N) = X(N)
C     X(2,N) = Y(N)
C     X(3,N) = RADIUS(N).
C
C     RMIN = MINIMUM PARTICLE RADIUS IN THE CONTROL VOLUME.
C
      READ(51,*) NPART,XCELL,YCELL,SKN,SKT,A,PHI,HP
      WRITE(12,999)NPART,XCELL,YCELL,SKN,SKT,A,PHI,HP
      WRITE(6,999)NPART,XCELL,YCELL,SKN,SKT,A,PHI,HP
      WRITE(36,999)NPART,XCELL,YCELL,SKN,SKT,A,PHI,HP
c     WRITE(12,996)
      RMIN = 1.0D5
      RMAX = 0.0D0
      DO 15 I=1, NPART
         READ(51,*) X(1,I),X(2,I),X(3,I)
         RD = X(3,I)
         RMIN = DMIN1(RMIN,RD)
         RMAX = DMAX1(RMAX,RD)
c      WRITE(6,998)X(1,I),X(2,I),X(3,I)
 15   CONTINUE
      PI=4.0D0*DATAN(1.0D0)
      TANPHI=DTAN(PHI*PI/180.0D0)
C
C.... BOUNDARY CONDITION DATA: FIX ORIGIN PARTICLE
C
      CALL ICLEAR(ID,3*NPART)
      DO 1 I=1, 3
         ID(I,1) = 1
 1    CONTINUE
c     do 2 i=1, npart
c     id(3,i)=1
c     2    continue
C
C.... ESTABLISH EQUATION NUMBERS
C
      NEQ = 0
      DO 10 N=1, NPART
         DO 10 I=1, 3
            IF(ID(I,N).EQ.0) GOTO 5
            ID(I,N) = 0
            GO TO 10
 5          NEQ = NEQ + 1
```

```
            ID(I,N) = NEQ
 10   CONTINUE
c      WRITE(12,994)
c      DO 11 I=1, NPART
c      WRITE(12,993) I, (ID(J,I), J=1,3)
c 11   CONTINUE
C
C.... INPUT CONTACT ELEMENT DATA
C     ASSUME THAT A PARTICLE MAY INTERACT ONLY WITH
C     PARTICLES WITHIN A RADIUS EQUAL TO 4*(LARGEST
C     PARTICLE RADIUS).
C
      XA(1) = XCELL
      XA(2) = ZERO
      XB(1) = ZERO
      XB(2) = YCELL
      DET    = XA(1)*XB(2)-XB(1)*XA(2)
      NUMEL = 0
      DO 20 NA=1,NPART-1
         DO 60 NB=NA+1,NPART
C
      RA     = X(3,NA)
      RB     = X(3,NB)
      RPLUSR = RA + RB
C
      XL0(1) = X(1,NB) - X(1,NA)
      XL0(2) = X(2,NB) - X(2,NA)
      AA = (XB(1)*XL0(2)-XB(2)*XL0(1))/DET
      BB = (XA(2)*XL0(1)-XA(1)*XL0(2))/DET
      SIGNA = ZERO
      IF(AA.NE.ZERO) SIGNA=AA/DABS(AA)
      SIGNB = ZERO
      IF(BB.NE.ZERO) SIGNB=BB/DABS(BB)
C
      DO 65 I=0,1
      DO 70 J=0,1
      DI = DREAL(I)
      DJ = DREAL(J)
      XL0(1) = X(1,NB) + DI*SIGNA*XA(1) + DJ*SIGNB*XB(1)
      XL0(2) = X(2,NB) + DI*SIGNA*XA(2) + DJ*SIGNB*XB(2)
      XL0(1) = XL0(1) - X(1,NA)
      XL0(2) = XL0(2) - X(2,NA)
      DELTA = DSQRT(DOT(XL0,XL0,2))
      IF(DELTA.LT.4.0D0*RMAX) GOTO 55
 70   CONTINUE
 65   CONTINUE
      GOTO 60
 55   CONTINUE
      NUMEL = NUMEL + 1
      IEN(1,NUMEL) = NA
      IEN(2,NUMEL) = NB
 60   CONTINUE
 20   CONTINUE
C
C.... INITIALIZE THE HARDENING ARRAY TO PARTICLE COHESION AND
C     THE CONTACT ARRAY TO ALL PARTICLES IN CONTACT WITH EACH
C     OTHER (ie ICON(NUMEL)=1).
C
      DO 25 I=1, NUMEL
         ALPHA(I)=A
         ICON(I)=1
 25   CONTINUE
C
C.... LOCALIZE ID ARRAY
C
      DO 40 K=1, NUMEL
         DO 30 J=1, 2
            NN = IEN(J,K)
            DO 30 I=1,3
               LM(3*(J-1)+I,K) = ID(I,NN)
 30      CONTINUE
 40   CONTINUE
C
C.... COMPUTE DIAGONAL ADDRESSES
C
      NSTIFF = 1
      IDIAG(1) = 1
      IF(NEQ.EQ.1) GOTO 100
      DO 50 I=2, NEQ
         IDIAG(I) = IDIAG(I-1) + I
 50   CONTINUE
      NSTIFF = IDIAG(NEQ)
C
C.... CALL DRIVER PROGRAM
C
 100  CALL MACROI(XCELL,YCELL,AUPPER,ALOWER,B,IDIAG)
C
C.... PRINT RESULTS
C
 993  FORMAT(2X,I3,9X,3I4)
 994  FORMAT(/,'ID ARRAY:',/,'PARTICLE',3X,'GLOBAL EQ. NUMBER')
 996  FORMAT(//,10X,'X',15X,'Y',14X,'RADIUS')
 998  FORMAT(F16.8,F16.8,F16.8)
 999  FORMAT('NUMBER OF PARTICLES = ',I3,/,
     X     'WIDTH OF THE CONTROL VOLUME: XCELL = ',F16.8,/,
     X     'HIEGHT OF THE CONTROL VOLUME: YCELL = ',F16.8,/,
     X     'NORMAL SPRING STIFFNESS = ',E20.8,/,
     X     'TANGENTIAL SPRING STIFFNESS = ',E20.8,/,
     X     'PARTICLE COHESION = ',E20.8,/,
     X     'PACTICLE FRICTION ANGLE = ',F16.8,/,
     X     'HARDENING PARAMETER = ',E20.8,/)
C
      CLOSE(UNIT=12)
      CLOSE(UNIT=24)
      CLOSE(UNIT=36)
      CLOSE(UNIT=48)
      CLOSE(UNIT=60)
      CLOSE(UNIT=51)
C
      STOP
      END
```

```
C===============================================================
      SUBROUTINE MACROI(XCELL,YCELL,AUPPER,ALOWER,B,IDIAG)
C
C.... INVERSE PROBLEM DRIVER PROGRAM
C
      IMPLICIT REAL*8(A-H,O-Z)
C
C.... REMOVE ABOVE CARD FOR SINGLE PRECISION OPERATION
C
      DIMENSION XAOLD(2),XBOLD(2),EPSI(3),EPS(3,1000),DELSIG(3,1000)
      DIMENSION EK(6,6),P(6),XA(2),XB(2),DSIG(3),SK(3,3)
      DIMENSION AUPPER(1),ALOWER(1),B(1),IDIAG(1)
      DIMENSION UNITY(3,3),SIG1(3),SIG2(3),SIGT(3)
      COMMON /MACRO / FSIG(3),SIG(3),EP(3)
      COMMON /PARTCL/ X(3,1000),NPART,RMIN
      COMMON /INFO  / IEN(2,20000),ID(3,1000),LM(6,20000),
     X                NUMEL,NEQ,NSTIFF
      COMMON /DSDATA/ D(3,1000),DD(3,1000),DINC(3,1000),
     X                DDINC(3,1000)
      COMMON /FDATA / FTN(20000),ALPHA(20000),ICON(20000)
      COMMON /ELDATA/ SKN,SKT,A,TANPHI,HP
      DATA ZERO,ONE/0.0D0,1.0D0/
C
      CALL CLEAR(UNITY,9)
      DO 1 I=1, 3
         UNITY(I,I)=ONE
 1    CONTINUE
C
C.... CLEAR MACRO QUANTITIES: STRESS AND STRAIN
C
      CALL CLEAR(FSIG,3)
      CALL CLEAR(SIG,3)
      CALL CLEAR(EP,3)
      CALL CLEAR(SIG1,3)
      CALL CLEAR(SIG2,3)
C
C.... CLEAR MICRO QUANTITIES: TANGENTIAL FORCE, DISPLACEMENT,
C     AND DISPLACEMENT INCREMENT.
C
      CALL CLEAR(FTN,NUMEL)
      CALL CLEAR(D,3*NPART)
      CALL CLEAR(DINC,3*NPART)
      CALL ICLEAR(ICON,NUMEL)
C
C.... INITIAL CONTROL VOLUME CONFIGURATION
C
      XA(1) = XCELL
      XA(2) = ZERO
      XB(1) = ZERO
      XB(2) = YCELL
C
C.... ANALYSIS OPTIONS
```

```
C          ICODE=0 => STRAIN CONTROL
C          ICODE=1 => STRESS CONTROL
C          ICODE=2 => 2 TIMESTEPS STRAIN CONTROL; STRESS CONTROL
C
      ICODE = 2
      IF(ICODE.EQ.1) GOTO 7000
C
C
C     ====================
C        STRAIN CONTROL
C     ====================
C
C
C.... INPUT MACROSCOPIC STRAIN INCREMENTS (EPS)
C
c     A(k-1)=eps(I,1)     A(k)=eps(I,2)
      WRITE(6,980)
      WRITE(36,980)
      NSTEP = 2
      fnmax=0.0d0
      CALL CLEAR(EPS,3*NSTEP)
      DO 10 I=1, NSTEP
         EPS(1,I) = -8.500d-3
         EPS(2,I) = -8.500d-3
         EPS(3,I) =  1.00d-5
c
         IF(I.GE.2) THEN
            EPS(1,I) = -8.600d-3
            EPS(2,I) = -8.600d-3
            EPS(3,I) =  2.00d-5
         ENDIF
 10   CONTINUE
C
C.... TIME STEP LOOP
C
      DO 1000 NS=1,NSTEP
      WRITE(6,982) NS
c      WRITE(12,982) NS
      WRITE(24,982) NS
      WRITE(36,982) NS
C
C.... UPDATE CONTROL VOLUME CONFIGURATION
C
      DO 15 I=1,3
         EP(I) = EP(I) + EPS(I,NS)
         EPSI(I) = EPS(I,NS)
 15   CONTINUE
      DO 150 I=1,2
         XAOLD(I)=XA(I)
         XBOLD(I)=XB(I)
 150  CONTINUE
C
```

```
C.... CALL STRAIN DRIVER PROGRAM
C
      CALL MICRO(EPSI,XA,XB,XAOLD,XBOLD,NS,NSTEP,DET,
     X     AUPPER,ALOWER,B,IDIAG,fnmax)
C
C.... UPDATE TANGENTIAL CONTACT FORCES/CALCULATE MACRO STRESS
C
      CALL CLEAR(SIG,3)
      DO 2000 N=1,NUMEL
      NA = IEN(1,N)
      NB = IEN(2,N)
      ITASK = 1
      IF(ICODE.EQ.2) ITASK=2
      CALL CNTACT(N,NA,NB,P,EK,XA,XB,DET,ITOUCH,ITASK,XAOLD,
     x     XBOLD,fnmax,nplas)
 2000 CONTINUE
C
      XAxXB  = DABS(XA(1)*XB(2) - XA(2)*XB(1))
      AREA   = XAxXB
      SIG(1) = SIG(1)/AREA
      SIG(2) = SIG(2)/AREA
      SIG(3) = SIG(3)/AREA
C
      IF(ICODE.NE.2) GOTO 4999
      XA(1)=XCELL
      XA(2)=ZERO
      XB(1)=ZERO
      XB(2)=YCELL
      IF(NS.EQ.1) THEN
         CALL MOVE(SIG1,SIG,3)
         GOTO 5001
      ELSE
         CALL MOVE(SIG2,SIG,3)
         GOTO 5001
      ENDIF
C
C.... UPDATE COORDINATES OF PARTICLE CENTROIDS
C
 4999 CONTINUE
      DO 5000 I=1,NPART
      X(1,I) = X(1,I) + DINC(1,I)
      X(2,I) = X(2,I) + DINC(2,I)
C
C.... CHECK FOR IMAGE PARTICLE
C
      AA  = (XB(2)*X(1,I)-XB(1)*X(2,I))/DET
      BB  = (XA(1)*X(2,I)-XA(2)*X(1,I))/DET
      IF(AA.GE.ZERO.AND.AA.LE.ONE.AND.BB.GE.ZERO.AND.BB.LE.ONE)
     X   GOTO 5000
C
C.... CONVERT IMAGE PARTICLE TO REAL
C
```

```
      IF(AA.LT.ZERO) AA=AA+ONE
      IF(AA.GT.ONE)  AA=AA-ONE
      IF(BB.LT.ZERO) BB=BB+ONE
      IF(BB.GT.ONE)  BB=BB-ONE
      X(1,I) = AA*XA(1) + BB*XB(1)
      X(2,I) = AA*XA(2) + BB*XB(2)
 5000 CONTINUE
C
C.... OUTPUT
C
 5001 CONTINUE
C     PRINCIPAL STRESSES
      TEMP=DSQRT((SIG(1)-SIG(2))*(SIG(1)-SIG(2))+4.0D0*SIG(3)*SIG(3))
      PSIG1=-0.50D0*(SIG(1)+SIG(2) + TEMP)
      PSIG2=-0.50D0*(SIG(1)+SIG(2) - TEMP)
C
      IF(ICODE.EQ.0) GOTO 5002
      WRITE(6,978) -EPS(1,NS),-SIG(1),-EPS(2,NS),-SIG(2),
     X      -EPS(3,NS),-SIG(3)
      WRITE(36,977)
      WRITE(36,978) -EPS(1,NS),-SIG(1),-EPS(2,NS),-SIG(2),
     X     -EPS(3,NS),-SIG(3)
      WRITE(24,990) NS, NPART, XCELL, YCELL
      GOTO 825
 5002 CONTINUE
      WRITE(6,978) -EP(1),-SIG(1),-EP(2),-SIG(2),-EP(3),-SIG(3)
      WRITE(36,977)
      WRITE(36,978) -EP(1),-SIG(1),-EP(2),-SIG(2),-EP(3),-SIG(3)
      WRITE(24,990) NS, NPART, XCELL, YCELL
      DO 850 I=1, NPART
         WRITE(24,994) X(1,I),X(2,I),X(3,I)
 850  CONTINUE
      WRITE(24,991) 0.0D0, 0.0D0, X(3,I)
      WRITE(24,991) XA(1), XA(2), X(3,I)
      WRITE(24,991) XA(1)+XB(1), XA(2)+XB(2), X(3,I)
      WRITE(24,991) XB(1), XB(2), X(3,I)
      WRITE(24,991) 0.0D0, 0.0D0, X(3,I)
 825  CONTINUE
      IF(NS.EQ.1) WRITE(48,977)
      IF(ICODE.EQ.0) WRITE(48,976) -EP(1),-SIG(1),-EP(2),-SIG(2),
     X     -EP(3),-SIG(3)
     X     ,PSIG1,PSIG2
      IF(ICODE.EQ.2) WRITE(48,976) -EPS(1,NS),-SIG(1),-EPS(2,NS),
     X     -SIG(2),-EPS(3,NS),-SIG(3)
     X     ,PSIG1,PSIG2
C
 1000 CONTINUE
C
      IF(ICODE.EQ.0) RETURN
C
C     ====================
C        STRESS CONTROL
```

```
C     ===================
C
c     sig1=sig(K-1)  sig2=sig(K)
c     eps(i,1)=eps(K-1)  eps(i,2)=eps(K)
 7000 CONTINUE
      WRITE(6,983)
      WRITE(36,983)
C
C.... INPUT MACROSCOPIC STRESS INCREMENTS (DELSIG)
C
      NSTEP = 900
      CALL CLEAR(DELSIG,3*NSTEP)
      CALL CLEAR(EP,3)
      DO 5 I=1, NSTEP
         if(i.eq.1 .or. i.eq.2) then
            DELSIG(1,I) = -0.9810d+01
            DELSIG(2,I) = -0.9810d+01
            DELSIG(3,I) = -0.00d+00
         else
            DELSIG(1,I) = -0.50d+00
            DELSIG(2,I) =  0.00d+00
            DELSIG(3,I) =  0.00d+00
         endif
 5    CONTINUE
C
C.... TIME STEP LOOP
C
      DO 500 NS=1,NSTEP
      WRITE(6, 982) NS
      WRITE(12,982) NS
      WRITE(24,982) NS
      WRITE(36,982) NS
C
C.... CONVERGENCE CRITERIA
C
      ETOL = ZERO
      DO 7 I=1, 3
         ETOL = ETOL + DELSIG(I,NS)*DELSIG(I,NS)
 7    CONTINUE
      ETOL = 1.0d-7*DSQRT(ETOL)
C
C.... UPDATE CONTROL VOLUME CONFIGURATION
C
      DO 25 I=1, 2
         XAOLD(I)=XA(I)
         XBOLD(I)=XB(I)
 25   CONTINUE
C
C.... COMPUTE SIGbar
C
      DO 20 I=1, 3
         FSIG(I) = FSIG(I) + DELSIG(I,NS)
 20   CONTINUE
C
C.... ITERATION LOOP
C
      IT = 0
      CALL CLEAR(EPSI,3)
 450  CONTINUE
      DO 90 I=1, 2
         XA(I)=XAOLD(I)
         XB(I)=XBOLD(I)
 90   CONTINUE
      IF(IT.EQ.0) CALL MOVE(SIG,SIG2,3)
      IF(IT.EQ.0) GOTO 499
C
C.... CALL STRAIN DRIVER PROGRAM
C
      WRITE(6,980)
      WRITE(36,980)
      WRITE(6,992) EPSI(1),EPSI(2),EPSI(3)
      WRITE(36,992) EPSI(1),EPSI(2),EPSI(3)
      CALL MICRO(EPSI,XA,XB,XAOLD,XBOLD,NS,NSTEP,DET,
     X     AUPPER,ALOWER,B,IDIAG,fnmax)
      WRITE(6,984)
      WRITE(36,984)
C
C.... UPDATE TANGENTIAL CONTACT FORCES/CALCULATE MACRO STRESS
C
      CALL CLEAR(SIG,3)
      DO 35 N=1,NUMEL
      NA = IEN(1,N)
      NB = IEN(2,N)
      CALL CNTACT(N,NA,NB,P,EK,XA,XB,DET,ITOUCH,2,XAOLD,
     x     XBOLD,fnmax,nplas)
 35   CONTINUE
C
      XAxXB  = DABS(XA(1)*XB(2) - XA(2)*XB(1))
      AREA   = XAxXB
      SIG(1) = SIG(1)/AREA
      SIG(2) = SIG(2)/AREA
      SIG(3) = SIG(3)/AREA
C
      CALL MOVE(SIG1,SIG2,3)
      CALL MOVE(SIG2,SIG ,3)
C
 499  CONTINUE
      WRITE(6,996) SIG(1),SIG(2),SIG(3)
      WRITE(36,996) SIG(1),SIG(2),SIG(3)
      DO 40 I=1, 3
         DSIG(I) = FSIG(I) - SIG(I)
 40   CONTINUE
C
C.... COMPUTE RESIDUAL
```

```
C
      RESID = ZERO
      DO 45 I=1, 3
         RESID = RESID + DSIG(I)*DSIG(I)
 45   CONTINUE
      RESID = DSQRT(RESID)
      IF(IT.EQ.0) WRITE(6,981) ETOL
      IF(IT.EQ.0) WRITE(12,981) ETOL
      IF(IT.EQ.0) WRITE(36,981) ETOL
      WRITE(6,995) IT+1, RESID
      WRITE(12,995) IT+1, RESID
      WRITE(36,995) IT+1, RESID
      IF(RESID.LE.ETOL) GOTO 700
C
C.... TANGENT OPERATOR
C
C     TANGENT OPTIONS FOR THE START OF EACH TIMESTEP:
C        1.) USE THE CONVERGED TANGENT FROM THE
C            PREVIOUS TIMESTEP FOR THE FIRST ITERATION.
c      IF(NS.GE.2 .AND. IT.EQ.0) GOTO 76
C
C        2.) USE THE CONVERGED TANGENT FROM THE
C            PREVIOUS TIMESTEP FOR THE FIRST TWO ITERATIONS.
      IF(NS.GE.2 .AND. IT.LE.1) GOTO 76
C
C        3.) UPDATE THE TANGENT EVERY OTHER ITERATION.
c      MDIV = (IT+1)/2
c      IF(MDIV*2.EQ.(IT+1)) GOTO 76
C
      CALL CLEAR(SK,9)
      CALL MOVE(SIGT,SIG2,3)
C
C.... DISCRETE TANGENT OPTIONS
C          ITAN=0 => TANGENT APPROXIMATED BY THE DIFFERENCE EXPRESSION
C                    IN ORTEGA AND RHEINBOLT (7.1.15) PG. 185.
C          ITAN=1 => TANGENT APPROXIMATED BY THE DIFFERENCE EXPRESSION
C                    IN ORTEGA AND RHEINBOLT (7.1.16) PG. 186.
C          ITAN=2 => EXACT TANGENT OPERATOR
C
      ITAN = 0
C
      WRITE(6,985)
      WRITE(36,985)
      DO 50 J=1, 3
C
         IF(ITAN.EQ.1) GOTO 8000
C
         IF(J.GE.2) CALL MOVE(SIGT,SIG,3)
         IF(J.EQ.3) CALL MOVE(SIG,SIG1,3)
         DO 61 I=1, 3
            EPSI(I) = EPS(I,2)
 61      CONTINUE
```

```
         DO 62 K=1, J
            DO 63 I=1, 3
               EPSI(I) = EPSI(I) + UNITY(I,K)*(EPS(K,1)-EPS(K,2))
 63         CONTINUE
 62      CONTINUE
         GOTO 9000
C
 8000    CONTINUE
         DO 60 I=1, 3
            EPSI(I) = EPS(I,2) + UNITY(I,J)*(EPS(J,1)-EPS(J,2))
 60      CONTINUE
C
 9000    CONTINUE
         write(6,*)'J = ',j
         write(36,*)'J = ',j
         WRITE(6,992) EPSI(1),EPSI(2),EPSI(3)
         WRITE(36,992) EPSI(1),EPSI(2),EPSI(3)
      IF(J.EQ.3 .AND. ITAN.EQ.0) GOTO 73
         DO 65 I=1, 2
            XA(I) = XAOLD(I)
            XB(I) = XBOLD(I)
 65      CONTINUE
         CALL MICRO(EPSI,XA,XB,XAOLD,XBOLD,NS,NSTEP,DET,
     X        AUPPER,ALOWER,B,IDIAG,fnmax)
         CALL CLEAR(SIG,3)
         DO 71 N=1, NUMEL
            NA = IEN(1,N)
            NB = IEN(2,N)
            CALL CNTACT(N,NA,NB,P,EK,XA,XB,DET,ITOUCH,2,XAOLD,
     x           XBOLD,fnmax,nplas)
 71      CONTINUE
C
         XAxXB  = DABS(XA(1)*XB(2) - XA(2)*XB(1))
         AREA   = XAxXB
         SIG(1) = SIG(1)/AREA
         SIG(2) = SIG(2)/AREA
         SIG(3) = SIG(3)/AREA
 73      CONTINUE
      WRITE(6 ,996) SIG(1),SIG(2),SIG(3)
      WRITE(36,996) SIG(1),SIG(2),SIG(3)
         TEMP = ONE/(EPS(J,1)-EPS(J,2))
         DO 74 I=1, 3
            SK(I,J) = (SIG(I) - SIGT(I))*TEMP
 74      CONTINUE
 50   CONTINUE
 76   continue
      WRITE(6 ,*)'SK: '
      WRITE(36,*)'SK: '
      do 77 I=1, 3
         WRITE(6 ,988)(SK(I,J), J=1,3)
         WRITE(36,988)(SK(I,J), J=1,3)
 77   continue
```

```
c        write(36,997) dsig(1),dsig(2),dsig(3)
      WRITE(6,986)
      WRITE(36,986)
      K = 0
      DO 105 J=1, 3
         DO 110 I=1, J
            K = K + 1
            AUPPER(K) = SK(I,J)
            ALOWER(K) = SK(J,I)
 110     CONTINUE
 105  CONTINUE
C
C.... FACTORIZE TANGENT OPERATOR
C
c        WRITE(36,*)'DIAGONAL AND RHS BEFORE FACTORIZATION:'
c        DO 235 I=1, 3
c           WRITE(36,987) I, AUPPER(IDIAG(I)), I, DSIG(I)
c 235    CONTINUE
      CALL NSOLVE(AUPPER,ALOWER,DSIG,IDIAG,3,.TRUE.,.FALSE.)
      DO 238 I=1, 3
         IF(DABS(AUPPER(IDIAG(I))).LT.1.0D-9)
     X        WRITE(6,979) I, AUPPER(IDIAG(I))
         IF(DABS(AUPPER(IDIAG(I))).LT.1.0D-9)
     X        WRITE(12,979) I, AUPPER(IDIAG(I))
         IF(DABS(AUPPER(IDIAG(I))).LT.1.0D-9)
     X        WRITE(36,979) I, AUPPER(IDIAG(I))
 238  CONTINUE
C
C.... FORWARD REDUCE AND BACK SUBSTITUTE
C
      CALL NSOLVE(AUPPER,ALOWER,DSIG,IDIAG,3,.FALSE.,.TRUE.)
c        WRITE(36,*)
c        WRITE(36,*)'DIAGONAL AND RHS AFTER FACTORIZATION:'
c        DO 236 I=1, 3
c           WRITE(36,987) I, AUPPER(IDIAG(I)), I, DSIG(I)
c 236    CONTINUE
      DO 70 I=1, 3
         EPS(I,1) = EPS(I,2)
         EPS(I,2) = EPS(I,2) + DSIG(I)
         EPSI(I)  = EPS(I,2)
 70   CONTINUE
      WRITE(6,992) EPSI(1),EPSI(2),EPSI(3)
c        WRITE(36,992) EPSI(1),EPSI(2),EPSI(3)
      WRITE(6,993) DSIG(1),DSIG(2),DSIG(3)
c        WRITE(36,993) DSIG(1),DSIG(2),DSIG(3)
      IT = IT + 1
      IF(IT.LE.20) GOTO 450
C
C.... NO CONVERGENCE
C
      WRITE(*,100)
      WRITE(36,100)
 100  FORMAT(' NO CONVERGENCE AFTER 20 ITERATIONS')
      STOP
 700  CONTINUE
C
C.... CONVERGENCE
C
      CALL CLEAR(EPS,6)
      DO 75 I=1,3
         EP(I) = EP(I) + EPSI(I)
 75   CONTINUE
C
C.... UPDATE TANGENTIAL CONTACT FORCES/CALCULATE MACRO STRESS
C
      fnmax=0.0d0
      icntact = 0
      iplstic = 0
      CALL CLEAR(SIG,3)
      DO 200 N=1,NUMEL
      NA = IEN(1,N)
      NB = IEN(2,N)
      nplas = 0
      CALL CNTACT(N,NA,NB,P,EK,XA,XB,DET,ITOUCH,1,XAOLD
     x     ,XBOLD,fnmax,nplas)
      icntact = icntact + itouch
      iplstic = iplstic + nplas
 200  CONTINUE
C
      XAxXB  = DABS(XA(1)*XB(2) - XA(2)*XB(1))
      AREA   = XAxXB
      SIG(1) = SIG(1)/AREA
      SIG(2) = SIG(2)/AREA
      SIG(3) = SIG(3)/AREA
c
      write(6,*)'fnmax = ',fnmax
      write(24,*)'fnmax = ',fnmax
      write(24,*)'number of contacts = ',icntact
      write(24,*)'number of plastic contacts = ',iplstic
C
C.... UPDATE COORDINATES OF PARTICLE CENTROIDS
C
      DO 80 I=1,NPART
      X(1,I) = X(1,I) + DINC(1,I)
      X(2,I) = X(2,I) + DINC(2,I)
C
C.... CHECK FOR IMAGE PARTICLE
C
      AA  = (XB(2)*X(1,I)-XB(1)*X(2,I))/DET
      BB  = (XA(1)*X(2,I)-XA(2)*X(1,I))/DET
      IF(AA.GE.ZERO.AND.AA.LE.ONE.AND.BB.GE.ZERO.AND.BB.LE.ONE)
     X   GOTO 80
C
C.... CONVERT IMAGE PARTICLE TO REAL
```

```
C
      IF(AA.LT.ZERO) AA=AA+ONE
      IF(AA.GT.ONE)  AA=AA-ONE
      IF(BB.LT.ZERO) BB=BB+ONE
      IF(BB.GT.ONE)  BB=BB-ONE
      X(1,I) = AA*XA(1) + BB*XB(1)
      X(2,I) = AA*XA(2) + BB*XB(2)
   80 CONTINUE
C
C.... CHECK FOR LOCALIZATION
C
      CALL LOCALI(SK,NS)
C
C.... OUTPUT
C
C     PRINCIPAL STRESSES
      TEMP=DSQRT((SIG(1)-SIG(2))*(SIG(1)-SIG(2))+4.0D0*SIG(3)*SIG(3))
      PSIG1=-0.50D0*(SIG(1)+SIG(2) + TEMP)
      PSIG2=-0.50D0*(SIG(1)+SIG(2) - TEMP)
C
      WRITE(6,978) -EP(1),-SIG(1),-EP(2),-SIG(2),-EP(3),-SIG(3)
      WRITE(36,977)
      WRITE(36,978) -EP(1),-SIG(1),-EP(2),-SIG(2),-EP(3),-SIG(3)
      IF(NS.EQ.1) WRITE(48,977)
      WRITE(48,976) -EP(1),-SIG(1),-EP(2),-SIG(2),-EP(3),-SIG(3)
     X     ,PSIG1,PSIG2
      WRITE(24,990) NS, NPART, XCELL, YCELL
      DO 85 I=1, NPART
      WRITE(24,994) X(1,I),X(2,I),X(3,I)
 85   CONTINUE
      WRITE(24,991) 0.0D0, 0.0D0, X(3,I)
      WRITE(24,991) XA(1), XA(2), X(3,I)
      WRITE(24,991) XA(1)+XB(1), XA(2)+XB(2), X(3,I)
      WRITE(24,991) XB(1), XB(2), X(3,I)
      WRITE(24,991) 0.0D0, 0.0D0, X(3,I)
C
  500 CONTINUE
C
 976  FORMAT(8E16.8)
  977 FORMAT('MACROSCOPIC STRESS',/,5X,
     X     'EPSI(1)',7X,'SIG(1)',6X,'EPSI(2)',7X,'SIG(2)',
     X     6X,'EPSI(3)',7X,'SIG(3)')
  978 FORMAT(6E16.8)
  979 FORMAT('ZERO ON DIAGONAL-- EQ. #',I3,'  DIAG = ',E20.10)
  980 FORMAT(//,'====================','  STRAIN CONTROL',
     X       2X,'===================')
  981 FORMAT('CONVERGENCE CRITERION = ',E16.8)
  982 FORMAT(//,'TIMESTEP ',I3)
  983 FORMAT(///,'===================','  STRESS CONTROL',
     X       2X,'===================')
  984 FORMAT('========================================================')
  985 FORMAT(//,'================','  TANGENT OPERATOR',
     X       2X,'=================')
  986 FORMAT('=====================================================')
  987 FORMAT('DIAG(',I3,') = ',E20.10,7X,'B(',I3,') = ',E20.10)
  988 FORMAT(3F20.10)
  990 FORMAT(/,'CONTROL VOLUME CONFIGURATION AT THE END OF TIMESTEP
',I3,
     X     /,I3,2F20.14)
  991 FORMAT(3F20.10)
  992 FORMAT('STRAIN INCREMENT:',/,6X,'EPSI(1)',14X,'EPSI(2)',
     X     14X,'EPSI(3)',/,E16.8,5X,E16.8,5X,E16.8)
  993 FORMAT('DELTA(STRAIN INCREMENT):',/,6X,'DEPS(1)',14X,'DEPS(2)',
     X     14X,'DEPS(3)',/,E16.8,5X,E16.8,5X,E16.8)
  994 FORMAT(3F20.10)
  995 FORMAT(I2,' STRESS RESIDUAL = ',E16.8)
  996 FORMAT('STRESS:',/,6X,'SIG(1)',14X,'SIG(2)',
     X     14X,'SIG(3)',/,E16.8,5X,E16.8,5X,E16.8)
  997 FORMAT('STRESS RESIDUAL VECTOR:',/,6X,'DSIG(1)',14X,'DSIG(2)',
     X     14X,'DSIG(3)',/,E16.8,5X,E16.8,5X,E16.8)
C
      STOP
      END
```

```
C=========================================================
      SUBROUTINE MICRO(EPSI,XA,XB,XAOLD,XBOLD,NS,NSTEP,DET,
     X     AUPPER,ALOWER,B,IDIAG,fnmax)
C
C.... STRAIN DRIVEN PROBLEM DRIVER PROGRAM
C
      IMPLICIT REAL*8(A-H,O-Z)
C
C.... REMOVE ABOVE CARD FOR SINGLE PRECISION OPERATION
C
      DIMENSION EPSI(3),XAOLD(2),XBOLD(2)
      DIMENSION EK(6,6),P(6),XA(2),XB(2)
      DIMENSION AUPPER(1),ALOWER(1),B(1),IDIAG(1),BDPL(1000)
      COMMON /MACRO / FSIG(3),SIG(3),EP(3)
      COMMON /PARTCL/ X(3,1000),NPART,RMIN
      COMMON /INFO  / IEN(2,20000),ID(3,1000),LM(6,20000),
     X                NUMEL,NEQ,NSTIFF
      COMMON /DSDATA/ D(3,1000),DD(3,1000),DINC(3,1000),
     X                DDINC(3,1000)
      COMMON /FDATA / FTN(20000),ALPHA(20000),ICON(20000)
      COMMON /ELDATA/ SKN,SKT,A,TANPHI,HP
C
      DATA ZERO,ONE,ETOL/0.0D0,1.0D0,1.0D-8/
C
C.... INITIALIZE Dbar
C
      DO 5 I=1,NPART
      DINC(1,I) = EPSI(1)*X(1,I) + EPSI(3)*X(2,I)
      DINC(2,I) = EPSI(3)*X(1,I) + EPSI(2)*X(2,I)
      DINC(3,I) = 0.0D0
    5 CONTINUE
C
      TEMP  = (ONE+EPSI(1))*XA(1) + EPSI(3)*XA(2)
      XA(2) = EPSI(3)*XA(1) + (ONE+EPSI(2))*XA(2)
      XA(1) = TEMP
      TEMP  = (ONE+EPSI(1))*XB(1) + EPSI(3)*XB(2)
      XB(2) = EPSI(3)*XB(1) + (ONE+EPSI(2))*XB(2)
      XB(1) = TEMP
      DET   = XA(1)*XB(2)-XB(1)*XA(2)
C
C.... PSEUDO TIME STEP LOOP
C
      DT = 1.0D0
      DO 400 NT=1, 1
c      WRITE(6,980) NT
c      WRITE(12,980) NT
c      WRITE(24,980) NT
      CALL CLEAR(DDINC,3*NPART)
C
C.... NEWTON ITERATION LOOP
C
      ITER = 0
```

```
   10 CONTINUE
      ITER = ITER + 1
c      WRITE(6,996) ITER
c      WRITE(12,996) ITER
C
  701 CONTINUE
      ALPHK = ONE
C
  702 CONTINUE
      CALL CLEAR(AUPPER,NSTIFF)
      CALL CLEAR(ALOWER,NSTIFF)
      CALL CLEAR(B,NEQ)
C
C.... FORM RHS VECTOR AND TANGENT OPERATOR
C
      iflag = 0
      DO 15 N=1,NUMEL
      CALL CLEAR(P,6)
      CALL CLEAR(EK,36)
      NA = IEN(1,N)
      NB = IEN(2,N)
      CALL CNTACT(N,NA,NB,P,EK,XA,XB,DET,ITOUCH,ITASK,XAOLD,
     x     XBOLD,fnmax,nplas)
c      if(itouch.eq.1) then
c      if(iflag.eq.1) goto 104
c      iflag = 1
c      write(12,*) 'n = ',n
c      do 303 ii=1,6
c      write(12,223) (ek(ii,jj),jj=1,6), p(ii)
c 223  format(7f10.3)
c  222 format(6f10.3)
c  303 continue
c      endif
c  104 continue
      IF(ITOUCH.EQ.0) GOTO 15
      CALL ADDSTF(AUPPER,B,ALOWER,EK,P,IDIAG,LM(1,N))
   15 CONTINUE
C
C.... PARABOLIC REGULARIZATION
C
      IF(ITER.EQ.1) WRITE(6,*)'*** NO PSEUDO TIMESTEPPING ***'
      GOTO 35
      IF(ITER.EQ.1) GOTO 35
      DO 30 N=1, NPART
      CALL PAREG(N,AUPPER,B,ALOWER,IDIAG,DT)
 30   CONTINUE
 35   CONTINUE
C
C.... COMPUTE NORM OF RESIDUAL AND CHECK CONVERGENCE
C
      RESID1 = DSQRT(DOT(B,B,NEQ))
      IF(ITER.EQ.1) TOLER=RESID1*ETOL
```

```
C
C.... STEPLENGTH DETERMINATION/LINE SEARCH
C
C     FOR NO LINE SEARCH GOTO 705
c      go to 705
  706 continue
      IF(RESID1.LT.RESID0.OR.ITER.EQ.1) THEN
      IF(ITER.EQ.1) GOTO 705
c      WRITE(12,989)
c      DO 22 J=1, NPART
c      WRITE(12,985) J, (DDINC(I,J), I=1,3), (DINC(I,J),I=1,3)
c 22   CONTINUE
      GOTO 705
      ENDIF
      ALPHK = 0.50D0*ALPHK*ALPHK*RESID5/(RESID1+RESID5*ALPHK-RESID0)
      WRITE(*,777) ALPHK
      WRITE(36,777) ALPHK
  777 FORMAT(' ALPHK = ',F20.10)
      DO 17 I=1,3
      DO 16 J=1,NPART
      K = ID(I,J)
      IF(K.GT.0) DINC(I,J)=D(I,J)-ALPHK*BDPL(K)
      IF(K.GT.0) DDINC(I,J)=DD(I,J)-ALPHK*BDPL(K)
   16 CONTINUE
   17 CONTINUE
      GO TO 702
  705 CONTINUE
      IF(ITER.EQ.1) WRITE(6,981) TOLER
      IF(ITER.EQ.1) WRITE(36,981) TOLER
      WRITE(6,995) ITER, RESID1
      WRITE(36,995) ITER, RESID1
      IF(RESID1.LT.TOLER.OR.RESID1.LT.1.0D-7) GOTO 400
      RESID0 = RESID1
      RESID5 = RESID0
C
C.... FACTORIZE TANGENT OPERATOR
C
c      WRITE(12,*)'DIAGONAL AND RHS BEFORE FACTORIZATION:'
c      DO 235 I=1, NEQ
c         WRITE(12,987) I, AUPPER(IDIAG(I)), I, B(I)
c 235  CONTINUE
      CALL NSOLVE(AUPPER,ALOWER,B,IDIAG,NEQ,.TRUE.,.FALSE.)
      DO 238 I=1, NEQ
c         IF(DABS(AUPPER(IDIAG(I))).LT.1.0D-9)
c     X        WRITE(6,979) I, AUPPER(IDIAG(I))
c         IF(DABS(AUPPER(IDIAG(I))).LT.1.0D-9)
c     X        WRITE(12,979) I, AUPPER(IDIAG(I))
         IF(DABS(AUPPER(IDIAG(I))).LT.1.0D-9)
     X        WRITE(36,979) I, AUPPER(IDIAG(I))
 238  CONTINUE
C
C.... FORWARD REDUCE AND BACK SUBSTITUTE
```

```
C
      CALL NSOLVE(AUPPER,ALOWER,B,IDIAG,NEQ,.FALSE.,.TRUE.)
c      WRITE(12,*)
c      WRITE(12,*)'DIAGONAL AND RHS AFTER FACTORIZATION:'
c      DO 236 I=1, NEQ
c         WRITE(12,987) I, AUPPER(IDIAG(I)), I, B(I)
c 236  CONTINUE
C
C.... INTERMEDIATE UPDATE FOR DISPLACEMENT INCREMENT
C
      CALL MOVE(D,DINC,3*NPART)
      CALL MOVE(DD,DDINC,3*NPART)
      CALL MOVE(BDPL,B,NEQ)
      DO 25 I=1,3
      DO 20 J=1,NPART
      K = ID(I,J)
      IF(K.GT.0) DINC(I,J)=DINC(I,J)-B(K)
      IF(K.GT.0) DDINC(I,J)=DDINC(I,J)-B(K)
   20 CONTINUE
 25   CONTINUE
C
      IF (ITER.LT.45) GOTO 10
C
C.... NO CONVERGENCE
C
      WRITE(*,100)
      WRITE(36,100)
 100  FORMAT(' NO CONVERGENCE AFTER 45 ITERATIONS.')
      STOP
 400  CONTINUE
C
  979 FORMAT('ZERO ON DIAGONAL-- EQ. #',I3,'  DIAG = ',E20.10)
  980 FORMAT('PSEUDO TIMESTEP ',I3)
  981 FORMAT('CONVERGENCE CRITERION = ',E16.8)
  985 FORMAT(I3,2X,3E12.4,' |',3E12.4)
  987 FORMAT('DIAG(',I3,') = ',E20.10,7X,'B(',I3,') = ',E20.10)
  989 FORMAT(/,'PRT.#',2X,'D(DINC(1))',2X,'D(DINC(2))',2X,'D(DINC(3))',
     X     1X,'|',4X,'DINC(1)',5X,'DINC(2)',5X,'DINC(3)')
  995 FORMAT(I2,' RESIDUAL = ',E16.8)
  996 FORMAT(//,'ITERATION = ',I2)
C
      RETURN
      END
```

```
C==============================================================
      SUBROUTINE CNTACT(N,NA,NB,P,EK,XA,XB,DET,ITOUCH,ITASK,
     X     XAOLD,XBOLD,fnmax,nplas)
C
C     PROGRAM TO FORM ELEMENT FORCE VECTOR AND STIFFNESS MATRIX
C
      IMPLICIT REAL*8(A-H,O-Z)
C
C.... REMOVE ABOVE CARD FOR SINGLE PRECISION OPERATION
C
      DIMENSION P(1),EK(6,1),XA(1),XB(1),XAOLD(1),XBOLD(1)
      DIMENSION XN1(2,2),XL0(2),XL1(2),XNB(2)
      DIMENSION C(2,2),B(2,4),CB(2,4)
      COMMON /MACRO / FSIG(3),SIG(3),EP(3)
      COMMON /PARTCL/ X(3,1000),NPART,RMIN
      COMMON /DSDATA/ D(3,1000),DD(3,1000),DINC(3,1000),
     X                DDINC(3,1000)
      COMMON /FDATA / FTN(20000),ALPHA(20000),ICON(20000)
      COMMON /ELDATA/ SKN,SKT,A,TANPHI,HP
      DATA ZERO,HALF,ONE/0.0D0,0.50D0,1.0D0/
C
C.... ITASK OPTIONS:
C     ITASK=0 => CALCULATE ELEMENT CONTRIBUTION TO MICRO STIFFNESS
C     ITASK=1 => UPDATE MACRO STRESS AND CONTACT FORCES
C     ITASK=2 => CALCULATE MACRO STRESS WITHOUT ANY UPDATES
C
C.... IOPT OPTIONS:
C     IOPT=0 => ALL PARTICLE IN CONTACT WITH EACH OTHER AT Tn
C     IOPT=1 => NEW CONTACTS FORM AT Tn+1.
C
      IOPT = 0
C
      RA     = X(3,NA)/100.0D0
      RB     = X(3,NB)/100.0D0
      RPLUSR = (RA + RB)/100.0D0
      RA     = X(3,NA)
      RB     = X(3,NB)
      RPLUSR = (RA + RB)
C
      XN1(1,1) = X(1,NA) + DINC(1,NA)
      XN1(2,1) = X(2,NA) + DINC(2,NA)
      XN1(1,2) = X(1,NB) + DINC(1,NB)
      XN1(2,2) = X(2,NB) + DINC(2,NB)
C
      THETAA = DINC(3,NA)
      THETAB = DINC(3,NB)
C
C.... CHECK REAL AND IMAGE PARTICLES
C
      XL1(1) = XN1(1,2) - XN1(1,1)
      XL1(2) = XN1(2,2) - XN1(2,1)
      AA = (XB(1)*XL1(2)-XB(2)*XL1(1))/DET
      BB = (XA(2)*XL1(1)-XA(1)*XL1(2))/DET
      SIGNA = ZERO
      IF(AA.NE.ZERO) SIGNA=AA/DABS(AA)
      SIGNB = ZERO
      IF(BB.NE.ZERO) SIGNB=BB/DABS(BB)
C
      ITOUCH = 0
      DO 40 I=0,1
      DO 35 J=0,1
      DI = DREAL(I)
      DJ = DREAL(J)
      XNB(1) = XN1(1,2) + DI*SIGNA*XA(1) + DJ*SIGNB*XB(1)
      XNB(2) = XN1(2,2) + DI*SIGNA*XA(2) + DJ*SIGNB*XB(2)
C
      XL0(1) = X(1,NB) + DI*SIGNA*XAOLD(1) + DJ*SIGNB*XBOLD(1)
      XL0(2) = X(2,NB) + DI*SIGNA*XAOLD(2) + DJ*SIGNB*XBOLD(2)
C
C.... BRANCH VECTORS
C
      XL1(1) = XNB(1) - XN1(1,1)
      XL1(2) = XNB(2) - XN1(2,1)
      XL0(1) = XL0(1) - X(1,NA)
      XL0(2) = XL0(2) - X(2,NA)
      DELTA0 = DSQRT(DOT(XL0,XL0,2))
      DELTA1 = DSQRT(DOT(XL1,XL1,2))
C
C.... CHECK CONTACT
C
      DELTA = RPLUSR - DELTA1
      IF(DELTA.GT.ZERO) GOTO 50
   35 CONTINUE
   40 CONTINUE
C
C.... NO CONTACT
C
      IF(ITASK.GE.0) RETURN
      ICON(N)  = 0
      FTN(N)   = ZERO
      ALPHA(N) = A
      RETURN
C
C.... CONTACT
C
 50   CONTINUE
C      IF(NA.EQ.7 .OR. NB.EQ.7) WRITE(60,*)' NA = ',NA,' NB = ',NB,DELTA
C      write(36,*)'CONTACT BETWEEN PARTICLES ',NA,' AND ',NB, DELTA
      ITOUCH = 1
      EPS1    = 0.1D0*RMIN
      HEPS   = ONE
      DHEPS  = ZERO
      IF(DELTA.LT.EPS1) HEPS=DELTA/EPS1
      IF(DELTA.LT.EPS1) DHEPS=ONE/EPS1
```

```
C
C.... CONTACT STIFFNESS
C
      PI=DATAN(1.0D0)*4.0D0
C     E (N/cm^2)
      E    = 5.00d4
      NU   = 0.20D0
      R    = 1.0D0/(1.0D0/RA + 1.0D0/RB)
      Po   = 3.0d0
      TEMP = RA*RB*PI*E/(4.0D0*R*(1.0D0-NU*NU)*Po)
      SKN  = PI*E/(4.0D0*(1.0D0-NU*NU)*(DLOG(TEMP)+1.0D0))
      SKT  = SKN
C
C.... NORMALIZE BRANCH VECTORS
C
      DO 55 I=1,2
      XL0(I) = XL0(I)/DELTA0
      XL1(I) = XL1(I)/DELTA1
   55 CONTINUE
C
C.... ROTATION ANGLE
C
      THETAC = DASIN(XL0(1)*XL1(2) - XL0(2)*XL1(1))
c      WRITE(12,*)'THETA C = ', THETAC
C
C.... NORMAL CONTACT FORCE
C
      FN = -HEPS*SKN*DELTA
C
C.... TANGENTIAL CONTACT FORCE
C
      GAMMA  = RA*(THETAC-THETAA) + RB*(THETAC-THETAB)
      FTRIAL = FTN(N) + HEPS*SKT*GAMMA
      YIELD  = ALPHA(N) - FN*TANPHI
c      WRITE(12,*)'FTRIAL = ',FTRIAL
c      WRITE(12,*)'YIELD = ',YIELD
      IF(IOPT.EQ.1 .AND.ICON(N).EQ.0) THEN
         GPLAS  = ZERO
         FT     = FTRIAL
         C(1,1) = -SKN*(HEPS+DELTA*DHEPS)
         C(1,2) = ZERO
         C(2,1) = ZERO
         C(2,2) = ZERO
         GO TO 90
      ENDIF
      IF(DABS(FTRIAL).GT.YIELD) GOTO 70
C
C.... ELASTIC PROCESS; C = LOCAL STRESS-STRAIN MATRIX
C
c      WRITE(12,*)'ELASTIC PROCESS'
c     write(*,*) 'elastic process'
      nplas  = 0
      GPLAS  = ZERO
      FT     = FTRIAL
      C(1,1) = -SKN*(HEPS+DELTA*DHEPS)
      C(1,2) = ZERO
      C(2,1) = SKT*GAMMA*DHEPS
      C(2,2) = HEPS*SKT
c      WRITE(12,*)'GAMMA = ',GAMMA
c      WRITE(12,999)N,NA,NB,FT,FN
      GO TO 90
C
C.... PLASTIC PROCESS; C = LOCAL STRESS-STRAIN MATRIX
C
 70   CONTINUE
       nplas = 1
c      if(itask.eq.1) WRITE(24,*)'PLASTIC PROCESS'
c      write(*,*) 'plastic process'
      SIGN   = FTRIAL/DABS(FTRIAL)
      GPLAS  = SIGN*(DABS(FTRIAL)-YIELD)/(HEPS*SKT+HP)
      FT     = FTRIAL - HEPS*SKT*GPLAS
      TEMP   = ONE + HP/(SKT*HEPS)
      C(1,1) = -SKN*(HEPS+DELTA*DHEPS)
      C(1,2) = ZERO
      C(2,1) = HP*DHEPS*(GAMMA-GPLAS)/HEPS
     X         +SIGN*SKN*TANPHI*(HEPS+DELTA*DHEPS)
      C(2,1) = C(2,1)/TEMP
      C(2,2) = HEPS*SKT*(ONE - ONE/TEMP)
c      WRITE(12,*)'SIGN = ',SIGN
c      WRITE(12,*)'GAMMA = ',GAMMA
c      WRITE(12,*)'PLASTIC GAMMA = ',gplas
c      WRITE(12,*)'ELASTIC GAMMA = ',gamma-gplas
c      WRITE(12,999)N,NA,NB,FT,FN
C
C.... UPDATE VARIABLES
C
   90 CONTINUE
      IF(ITASK.EQ.0) GOTO 100
c      write(*,102)
  102 format(' i am here at update...')
      IF(IOPT.EQ.1 .AND. ICON(N).EQ.0) FT = ZERO
      FX = XL1(1)*FN - XL1(2)*FT
      FY = XL1(2)*FN + XL1(1)*FT
C
      SIG(1) = SIG(1) + FX*XL1(1)*DELTA1
      SIG(2) = SIG(2) + FY*XL1(2)*DELTA1
      SIG(3) = SIG(3) + 0.50D0*DELTA1*(FX*XL1(2)+FY*XL1(1))
      IF(ITASK.EQ.1) THEN
         ICON(N) = 1
         FTN(N) = FT
         ALPHA(N) = ALPHA(N)+HP*SIGN*GPLAS
c
c         WRITE(24,505) NA,NB,FX,FY,FT,FN
c         R=1.0D0/(1.0D0/RA + 1.0D0/RB)
```

```
c         e=2.0d0*E/(1.0d0-nu*nu)
c         a=8.0*fn*r/3.14160d0/e
c         a=a*a/r
c         write(24,*)'a/R = ', a
         if(dabs(fn).gt.fnmax)fnmax=dabs(fn)
         RETURN
      ENDIF
      IF(ITASK.EQ.2) RETURN
  505 FORMAT(' ELEM.',I3,'-',I3,' FX =',F10.5,
     X       ' FY =',F10.5,' FT =',E12.4,' FN =',E12.4)
      RETURN
C
C.... ASSEMBLE INTERNAL FORCE VECTOR
C
  100 CONTINUE
      P(1) = XL1(1)*FN - XL1(2)*FT
      P(2) = XL1(2)*FN + XL1(1)*FT
      P(3) = RA*FT
      P(4) = -P(1)
      P(5) = -P(2)
      P(6) = RB*FT
C
C.... B = STRAIN/DISPLACEMENT MATRIX
C
      B(1,1) = XL1(1)
      B(1,2) = XL1(2)
      B(1,3) = ZERO
      B(1,4) = ZERO
      TANC = DTAN(THETAC)/DELTA1
      SECC = ONE/(DCOS(THETAC)*DELTA1)
      B(2,1) = (XL1(1)*TANC + XL0(2)*SECC)*RPLUSR
      B(2,2) = (XL1(2)*TANC - XL0(1)*SECC)*RPLUSR
      B(2,3) = -RA
      B(2,4) = -RB
c       WRITE(12,*)'B'
c       DO 112 I=1, 2
c          WRITE(12,994) (B(I,J), J=1, 4)
c 112   CONTINUE
C
C.... CB = DISPLACEMENT GRADIENT OF LOCAL FORCE VECTOR
C
      DO 110 I=1,2
      DO 110 J=1,4
      CB(I,J) = C(I,1)*B(1,J) + C(I,2)*B(2,J)
  110 CONTINUE
c       WRITE(12,*)'CB'
c       DO 111 I=1, 2
c          WRITE(12,994) (CB(I,J), J=1, 4)
c 111   CONTINUE
C
C.... DISPLACEMENT GRADIENT OF UNIT NORMAL
C
```

```
      SL11 = (XL1(1)*XL1(1)-ONE)/DELTA1
      SL12 = XL1(2)*XL1(1)/DELTA1
      SL22 = (XL1(2)*XL1(2)-ONE)/DELTA1
C
C.... C = DISPLACEMENT GRADIENT OF GLOBAL FORCE VECTOR
C
      C(1,1) = XL1(1)*CB(1,1) - XL1(2)*CB(2,1) + SL11*FN - SL12*FT
      C(1,2) = XL1(1)*CB(1,2) - XL1(2)*CB(2,2) + SL12*FN - SL22*FT
      C(2,1) = XL1(2)*CB(1,1) + XL1(1)*CB(2,1) + SL12*FN + SL11*FT
      C(2,2) = XL1(2)*CB(1,2) + XL1(1)*CB(2,2) + SL22*FN + SL12*FT
C
C.... ELEMENT STIFFNESS MATRIX
C
      DO 120 I=1,2
      DO 120 J=1,2
      EK(I  ,J  ) = EK(I  ,J  ) + C(I,J)
      EK(I+3,J  ) = EK(I+3,J  ) - C(I,J)
      EK(I  ,J+3) = EK(I  ,J+3) - C(I,J)
      EK(I+3,J+3) = EK(I+3,J+3) + C(I,J)
  120 CONTINUE
C
C.... C = ROTATION GRADIENT OF GLOBAL FORCE VECTOR
C
      C(1,1) = XL1(1)*CB(1,3) - XL1(2)*CB(2,3)
      C(1,2) = XL1(1)*CB(1,4) - XL1(2)*CB(2,4)
      C(2,1) = XL1(2)*CB(1,3) + XL1(1)*CB(2,3)
      C(2,2) = XL1(2)*CB(1,4) + XL1(1)*CB(2,4)
C
      DO 130 I=1,2
      EK(I  ,3) = EK(I  ,3) + C(I,1)
      EK(I+3,3) = EK(I+3,3) - C(I,1)
      EK(I  ,6) = EK(I  ,6) + C(I,2)
      EK(I+3,6) = EK(I+3,6) - C(I,2)
      EK(3,I  ) = EK(3,I  ) + RA*CB(2,I)
      EK(3,I+3) = EK(3,I+3) - RA*CB(2,I)
      EK(6,I  ) = EK(6,I  ) + RB*CB(2,I)
      EK(6,I+3) = EK(6,I+3) - RB*CB(2,I)
  130 CONTINUE
C
      EK(3,3) = EK(3,3) + RA*CB(2,3)
      EK(3,6) = EK(3,6) + RA*CB(2,4)
      EK(6,3) = EK(6,3) + RB*CB(2,3)
      EK(6,6) = EK(6,6) + RB*CB(2,4)
C
c       WRITE(12,*)'STIFFNESS MATRIX'
c       DO 73 I=1, 6
c          WRITE(12,996)(EK(I,J), J=1, 6)
c 73    CONTINUE
c       WRITE(12,*)'ELEMENT INTERNAL FORCE VECTOR'
c       DO 74 I=1, 6
c          WRITE(12,995) P(I)
c 74    CONTINUE
```

```
C
 994  FORMAT(4F14.6)
 995  FORMAT(F12.4)
 996  FORMAT(6F12.4)
 999  FORMAT('ELEMENT NUMBER ',I5,' CONNECTING PARTICLES ',I3,
     X     ' AND ',I3,/,'TANGENTIAL FORCE = ',E16.8,/,
     X     'NORMAL FORCE = ',E16.8,/)
C
      RETURN
      END
```

```
C=================================================================
      SUBROUTINE LOCALI(C,NS)
C
C.... INVERSE PROBLEM DRIVER PROGRAM
C
      IMPLICIT REAL*8(A-H,O-Z)
C
C.... REMOVE ABOVE CARD FOR SINGLE PRECISION OPERATION
C
      DIMENSION C(3,3),X(3)
      DATA ZERO,ONE/0.0D0,1.0D0/
C
      HALF  = 1.0D0/2.0D0
      THIRD = 1.0D0/3.0D0
      RAD   = 4.0D0*DATAN(1.0D0)/180.0D0
C
C.... CALCULATE THE DETERMINATE OF THE ACOUSTIC TENSOR.
C
C     A0, A1, A2, A3, AND A4 ARE THE COEFFICIENTS OF THE
C     QUARTIC EXPRESSION DEFINING THE LOCALIZATION CONDITION.
C            F(X) = A4 X**4 + A3 X**3 + A2 X**2 + A1 X + A0 = 0
C     WHERE X=TAN(THETA), THETA DEFINES THE ORIENTATION OF
C     THE SHEAR BAND.
C
      A0 = C(1,1)*C(3,3) - C(1,3)*C(3,1)
      A1 = C(1,1)*C(3,2) + C(1,1)*C(2,3)
     X   - C(1,3)*C(2,1) - C(1,2)*C(3,1)
      A2 = C(1,1)*C(2,2) + C(1,3)*C(3,2) + C(3,1)*C(2,3)
     X   - C(1,2)*C(3,3) - C(1,2)*C(2,1) - C(3,3)*C(2,1)
      A3 = C(1,3)*C(2,2) + C(3,1)*C(2,2)
     X   - C(1,2)*C(2,3) - C(3,2)*C(2,1)
      A4 = C(3,3)*C(2,2) - C(2,3)*C(3,2)
c       a0 = 1.0d0
c       a1 = -240.0334830d0
c       a2 = 1.0d0
c       a3 = -10.0d0
c       a4 = 1.0d0
C
C.... FIND THE MINIMA OF THE LOCALIZATION CONDITION.  THE
C     MINIMA OCCURS AT THE ROOTS OF THE DERIVATIVE OF THE
C     LOCALIZATION CONDITION -- A CUBIC EQUATION.
C             F'(X) = X**3 + P X**2 + Q X + R = 0
C
      P = A3/A4*3.0D0/4.0D0
      Q = A2/A4/2.0D0
      R = A1/A4/4.0D0
C
C.... FIND THE ROOTS OF F'(X).
C
      A = (3.0D0*Q - P*P)*THIRD
      B = (2.0D0*P*P*P - 9.0D0*P*Q + 27.0D0*R)/27.0D0
C
```

```
      QQ = B*B/4.0D0 + A*A*A/27.0D0
      IF(DABS(QQ).LT.1.0D-8) QQ = ZERO
c      write(6,*) 'QQ = ',qq
C
C.... ANALYSIS OPTIONS
C          QQ>0 => ONE REAL ROOT AND TWO CONJUGATE COMPLEX ROOTS;
C          QQ=0 => THREE REAL ROOTS OF WHICH TWO AT LEAST TWO ARE EQUAL;
C          QQ<0 => THREE REAL AND UNEQUAL ROOTS.
C
C.... NOTE THE CHANGE IN VARIABLES Y = X - P/3.
C
      TEMP = P*THIRD
C
C.... COMPUTE ONLY THE REAL PARTS OF ALL THE ROOTS.  NOTE THAT
C     THE COMPLEX ROOTS WILL NOT BE USED IN THE LOCALIZATION
C     ANALYSIS BUT THEIR REAL PARTS WILL BE CALCULATED ANYWAYS.
C
C.... FOR QQ>0 OR QQ=0
      IF(QQ.LT.ZERO) GOTO 500
C
C.... FOR QQ<0
      TEMP2 = ONE
      TEMP3 = -HALF*B + DSQRT(QQ)
      IF(TEMP3.LT.ZERO) TEMP2 = -ONE
      AA = TEMP2*(DABS(TEMP3))**THIRD
      TEMP2 = ONE
      TEMP3 = -HALF*B - DSQRT(QQ)
      IF(TEMP3.LT.ZERO) TEMP2 = -ONE
      BB = TEMP2*(DABS(TEMP3))**THIRD
      X(1) = AA + BB - TEMP
      X(2) = -(AA + BB)/2.0D0 - TEMP
      X(3) = X(2)
      GOTO 1000
 500  CONTINUE
      THETA = DACOS(-HALF*B/DSQRT(DABS(-A*THIRD*A*THIRD*A*THIRD)))
      TEMP2  = 2.0D0*DSQRT(DABS(-THIRD*A))
      X(1) = TEMP2*DCOS(THETA*THIRD) - TEMP
      X(2) =-TEMP2*DCOS(THETA*THIRD + 60.0D0*RAD) - TEMP
      X(3) =-TEMP2*DCOS(THETA*THIRD - 60.0D0*RAD) - TEMP
C
 1000 CONTINUE
C
C.... FIND THE MINIMIA OF THE LOCALIZATION FUNCTION USING
C     ONLY THE REAL ROOTS OF THE CUBIC EQUATION.
C
      FMIN = 1.0D50
      N = 3
      IF(DABS(QQ).LT.1.0D-8) N = 2
      IF(QQ.GT.ZERO) N = 1
      DO 5 I=1, N
         F = A4*X(I)*X(I)*X(I)*X(I) + A3*X(I)*X(I)*X(I)
     X      + A2*X(I)*X(I) + A1*X(I) + A0
```

```
         IF(F.GT.FMIN) GOTO 5
         FMIN = F
         XMIN = X(I)
 5    CONTINUE
C
C.... OUTPUT
C
      IF(FMIN.LT.1.0D-8) WRITE(36,*)'LOCALIZATION'
      IF(FMIN.LT.1.0D-8) WRITE( 6,*)'LOCALIZATION'
      WRITE(36,990)N, FMIN, XMIN
c      WRITE( 6,990)N, FMIN, XMIN
      WRITE( 6,993) N
      WRITE(36,*)A4, A3, A2, A1, A0
      IF(NS.EQ.1) WRITE(60,991)
      WRITE(60,992) NS, FMIN, N
      WRITE(36,*) 'ROOTS: '
      WRITE(36,*) X(1), X(2), X(3)
 990  FORMAT('NUM. OF REAL ROOTS = ',I1,/,
     X     'LOCALIZATION FUNCTION MINIMA = ',E16.8,/,
     X     'TAN(THETA) AT MINIMA = ',E16.8)
 991  FORMAT('LOCALIZATION FUNC. FOR EACH TIMESTEP ',
     X     'AND NUM. OF REAL ROOTS:',/,'TIMESTEP',3X,'LOCAL. FUNCT.',3X,
     X     'NUM. REAL ROOTS')
 992  FORMAT(I3,5X,E20.10,5X,I2)
 993  FORMAT('NUM. OF REAL ROOTS = ',I1)
C
      RETURN
      END
```

```
C=============================================================
      SUBROUTINE PAREG(N,AUPPER,B,ALOWER,IDIAG,DT)
C
C     PROGRAM TO FORM PARTICLE FORCE VECTOR AND STIFFNESS MATRIX
C     RESULTING FROM THE DRAG/VISCOUS FORCE.
C
      IMPLICIT REAL*8(A-H,O-Z)
C
C.... REMOVE ABOVE CARD FOR SINGLE PRECISION OPERATION
C
      DIMENSION AUPPER(1),B(1),ALOWER(1),IDIAG(1)
      COMMON /PARTCL/ X(3,1000),NPART,RMIN
      COMMON /INFO  / IEN(2,20000),ID(3,1000),LM(6,20000),
     X                NUMEL,NEQ,NSTIFF
      COMMON /DSDATA/ D(3,1000),DD(3,1000),DINC(3,1000),
     X                DDINC(3,1000)
      DATA ZERO,TWO/0.0D0,2.0D0/
C
c      DAMP  =-1.0D2
      DAMP  = 0.0D0
      R     = X(3,N)
C
      DMAG  = DDINC(1,N)*DDINC(1,N) + DDINC(2,N)*DDINC(2,N)
      DRT   = DSQRT(DMAG)
c      write(12,*) n
c      write(12,997) drt
      IF(DRT.LT.1.0D-8) GOTO 300
C
      RDAMP = R*DAMP*DRT/(DT*DT)
C
      DO 200 I=1, 2
         K = ID(I,N)
         IF(K.EQ.0) GOTO 200
         VISC = RDAMP*DDINC(I,N)
         B(K) = B(K) + VISC
c         write(12,998) i, visc
 200  CONTINUE
C
      RDAMP = RDAMP/(DRT*DRT)
      K = ID(1,N)
      IF(K.EQ.0) GOTO 210
      J = IDIAG(K)
      STF = RDAMP*(DDINC(1,N)*DDINC(1,N) + DMAG)
c      write(12,996) 1, 1, stf
      AUPPER(J) = AUPPER(J) + STF
      ALOWER(J) = ALOWER(J) + STF
C
 210  CONTINUE
      K = ID(2,N)
      IF(K.EQ.0) GOTO 220
      J = IDIAG(K)
      STF = RDAMP*(DDINC(2,N)*DDINC(2,N) + DMAG)
```

```
c        write(12,996) 2, 2, stf
      AUPPER(J) = AUPPER(J) + STF
      ALOWER(J) = ALOWER(J) + STF
C
      STF = RDAMP*(DDINC(1,N)*DDINC(2,N))
c        write(12,996) 1, 2, stf
      AUPPER(J-1) = AUPPER(J-1) + STF
      ALOWER(J-1) = ALOWER(J-1) + STF
 220  CONTINUE
 300  CONTINUE
C
 996  FORMAT('STF(',I1,',',I1,') = ',E16.8)
 997  FORMAT('||delta(delta D)|| = ',E16.8)
 998  FORMAT('DOF ',I1,' RHS = ',E16.8)
 999  FORMAT('PARTICLE NUMBER ',I3)
C
      RETURN
      END
      SUBROUTINE ADDSTF(A,B,C,S,P,IDIAG,LM)
C
C ==========================================================
C     ADDS ELEMENT STIFFNESS AND FORCE TO THE GLOBAL ARRAYS.
C ==========================================================
C
      IMPLICIT REAL*8(A-H,O-Z)
C
C.... REMOVE ABOVE CARD FOR SINGLE PRECISION OPERATION
      DIMENSION A(1),B(1),C(1),IDIAG(1)
      DIMENSION S(6,1),P(1),LM(1)
C
      DO 10 J=1, 6
         K=LM(J)
         IF(K.EQ.0) GOTO 10
         B(K)=B(K)+P(J)
         L=IDIAG(K)-K
         DO 20 I=1, 6
            M=LM(I)
            IF(M.GT.K .OR. M.EQ.0) GOTO 20
            M=L+M
            A(M)=A(M)+S(I,J)
            C(M)=C(M)+S(J,I)
 20      CONTINUE
 10   CONTINUE
C
      RETURN
      END
```

```
C ==================================================
      SUBROUTINE NSOLVE(A,C,B,IDIAG,NEQ,FACT,BACK)
C
C.... PROGRAM TO PERFORM (A/C)=L*D*U FACTORIZATION AND/OR
C     BACKSUBSTITUTION OF AN UNSYMMETRIC SYSTEM OF EQUATIONS
C        A(NA)       = UPPER TRIANGULAR COEFFICIENT MATRIX
C                      STORED IN COLUMN FORM
C        C(NA)       = LOWER TRIANGULAR COEFFICIENT MATRIX
C                      STORED IN COLUMN FORM
C        B(NEQ)      = RIGHT SIDE VECTOR(AFTER BACKSUBSTITION,
C                      IT CONTAINS THE SOLUTION VECTOR.)
C        IDIAG(NEQ)  = ADDRESSES OF DIAGONAL TERM IN A(NA)
C        NEQ         = NUMBER OF EQUATIONS
C        FACT        = .TRUE. , FACTOR A / C
C                      .FALSE. , DO NOT FACTOR A / C
C        BACK       = .TRUE. , FORWARD REDUCE B(NEQ) AND BACKSUBSTITUTE
C                      .FALSE. , DO NOT FORWARD REDUCE B(NEQ) OR
C                         BACKSUBTITUTE
C
      IMPLICIT REAL*8(A-H,O-Z)
      REAL*8 DOT
C
C.... REMOVE ABOVE CARD FOR SINGLE-PRECISION OPERATION
C
      LOGICAL FACT,BACK
      DIMENSION A(1),B(1),C(1),IDIAG(1)
C
C.... FACTOR A TO UT*D*U,REDUCE B TO Y
C
      JR=0
      DO 10 J=1,NEQ
      JD=IDIAG(J)
      JH=JD-JR
      IF(JH.LE.1) GOTO 10
      NS=J+1-JH
      NE=J-1
      IF(.NOT.FACT) GOTO 20
      K=JR+1
      ID=0
C
C.... REDUCE ALL EQUATIONS EXCEPT DIAGONAL
C
      DO 30 I=NS,NE
      IR=ID
      ID=IDIAG(I)
      NT=MIN0(ID-IR-1,I-NS)
      IF(NT.EQ.0) GOTO 40
      A(K)=A(K)- DOT(A(K-NT),C(ID-NT),NT)
      C(K)=C(K)- DOT(C(K-NT),A(ID-NT),NT)
 40   IF(A(ID).NE.0.) C(K)=C(K)/A(ID)
   30 K=K+1
C
```

```
C.... REDUCE DIAGONAL TERM
C
      A(JD)=A(JD)- DOT(A(JR+1),C(JR+1),JH-1)
C
C.... FORWARD REDUCE THE R.H.S.
C
   20 IF(BACK) B(J)=B(J)-DOT(C(JR+1),B(NS),JH-1)
   10 JR=JD
      IF(.NOT.BACK) RETURN
C
C.... BACKSUBSTITUTION
C
      J=NEQ
      JD=IDIAG(J)
      IF(A(JD).NE.0.) B(J)=B(J)/A(JD)
      IF(NEQ.EQ.1) RETURN
   50 D=B(J)
      J=J-1
      JR=IDIAG(J)
      IF(JD-JR.LE.1) GOTO 60
      M=J-JD+JR+2
      K=JR-M+1
      DO 70 I=M,J
   70 B(I)=B(I)-A(I+K)*D
   60 JD=JR
      IF(A(JD).NE.0.) B(J)=B(J)/A(JD)
      IF(J.GT.1) GOTO 50
C
      RETURN
      END
```

```
C===============================================================
      SUBROUTINE MULT(A,B,C,IA,JA,JB)
C
C.... CALCULATE THE PRODUCT C=A*B
C
      IMPLICIT REAL*8(A-H,O-Z)
C
C.... REMOVE ABOVE CARD FOR SINGLE PRECISION OPERATION
C
      DIMENSION A(IA,JA), B(JA,JB), C(IA,JB)
C
      DO 5 I=1, IA
         DO 10 J=1, JB
            C(I,J)=0.0D0
            DO 15 K=1, JA
               C(I,J)=C(I,J)+A(I,K)*B(K,J)
 15         CONTINUE
 10      CONTINUE
 5    CONTINUE
      RETURN
      END
```

```
C =====================================================
      SUBROUTINE MOVE(A,B,N)
C
C.... PROGRAM TO MOVE N ELEMENTS OF ARRAY B INTO ARRAY A
C
      IMPLICIT REAL*8(A-H,O-Z)
C
C.... REMOVE ABOVE CARD FOR SINGLE-PRECISION OPERATION
C
      DIMENSION A(1),B(1)
      DO 10 I=1,N
   10 A(I)=B(I)
C
      RETURN
      END
```

```
C =====================================================
      DOUBLE PRECISION FUNCTION DOT(A,B,N)
C
C.... PROGRAM TO PERFORM THE DOT PRODUCT OF TWO VECTORS
C
      IMPLICIT REAL*8(A-H,O-Z)
C
C.... REMOVE ABOVE CARD FOR SINGLE-PRECISION OPERATION
C
      DIMENSION A(1),B(1)
C
      DOT=0.D0
      DO 10 I=1,N
   10 DOT=DOT+A(I)*B(I)
C
      RETURN
      END
```

```
C ==================================================
      SUBROUTINE CLEAR(A,M)
C
C.... PROGRAM TO CLEAR A FLOATING POINT ARRAY
C
      IMPLICIT REAL*8(A-H,O-Z)
C
C.... REMOVE ABOVE CARD FOR SINGLE-PRECISION OPERATION
C
      DIMENSION A(1)
      DO 10 I=1,M
   10 A(I)=0.D0
C
      RETURN
      END
```

```
C =====================================
      SUBROUTINE ICLEAR(IA,M)
C
C.... PROGRAM TO CLEAR AN INTERGER ARRAY
C
      DIMENSION IA(1)
      DO 10 I=1,M
   10 IA(I)=0
C
      RETURN
      END
```